



universität
wien

DISSERTATION

Titel der Dissertation

Application of the Random Phase Approximation to
Complex Problems in Materials Science

Verfasser

Dipl.-Ing. Laurids Schimka

angestrebter akademischer Grad

Doktor der Naturwissenschaften (Dr. rer. nat.)

Wien, 2012

Studienkennzahl lt. Studienblatt:	A 091 411
Dissertationsgebiet lt. Studienblatt:	Physik
Betreuerin / Betreuer:	Univ.Prof. Dipl.-Ing. Dr. Georg Kresse

Acknowledgements

First and foremost, I would like to thank Georg Kresse for his motivating supervision of my thesis and his invaluable support throughout the last three years. I thank the people of the Computational Materials Science group, Martijn, Doris, Kerstin and Michael for their support, the great working atmosphere and their never-ending patience to answer my questions. I am grateful to Judith and Nicola, who made my start as a PhD student as easy as possible. I enjoyed the - not always work-related - discussions and lively debates with my PhD colleagues Roman, Andreas, Thomas, Florian, Ronald and Merzuk. I also wish to express my most heart-felt thanks to my parents who have always supported me during the years of my education. Last but not least I'd like to thank my fiancée Miriam for her understanding, moral support and her efforts to care about the random phase approximation in the adiabatic-connection fluctuation-dissipation framework.

Abstract

This thesis is devoted to the assessment and application of the random phase approximation (RPA) in the adiabatic-connection fluctuation-dissipation (ACFD) framework in solid state physics.

The first part presents a review of density functional theory (DFT) and the ACFD theorem in the RPA. This includes an introduction to the many-body problem as well as a description of the implementation of the RPA in the Vienna Ab-initio Simulation Package (VASP).

In the results part, the quality of the RPA is assessed and its performance compared to three (beyond) DFT functionals. The experimental values are corrected for the effect of phonon zero-point vibrational energies which were calculated at the DFT level from ab-initio.

We find that the RPA describes all bonding situations very accurately, making it a promising candidate for more complex problems in solid state physics.

In light of these findings, we investigate the carbon-water interaction in two specific cases: the adsorption of water on benzene and the adsorption of water on a graphene layer. We compare our results to a different correlated method: diffusion Monte Carlo (DMC). We find very good agreement and thus believe that our values can serve as a benchmark for the development of other DFT functionals to treat water-carbon interfaces.

The highlight of this thesis is the successful application of the RPA to the long-standing and (at DFT level) unsolved *CO adsorption puzzle*. We show results for CO adsorption on Cu, late 4d metals and Pt. RPA is at present the only ab-initio method that describes adsorption and surface energies accurately at the same time and predicts the correct adsorption site in every single case.

Zusammenfassung

Die vorliegende Dissertation widmet sich der Bewertung und Anwendung der Random Phase Approximation (RPA) im Rahmen des Adiabatic-Connection Fluctuation-Dissipation Theorems (ACFDT) auf Problemstellungen der Festkörperphysik.

Im Theorie- und Methodenteil wird ein Überblick über Dichte Funktional Theorie (DFT) und das ACFD Theorem gegeben. Weiters beinhaltet dieser Teil eine einführende Diskussion des Vielteilchen Problems wie auch eine Beschreibung der Implementierung der Random Phase Approximation in dem Softwarepaket Vienna Ab-initio Simulation Package (VASP).

Im zweiten Teil der Disseration wird die Genauigkeit der RPA überprüft und mit Resultaten anderer Funktionale verglichen. Experimentelle Ergebnisse werden in Bezug auf Phononen Nullpunkt-Vibrationsenergien, welche ab-initio auf DFT Ebene berechnet wurden, korrigiert. RPA liefert eine sehr genaue Beschreibung aller Bindungsarten und ist daher ein vielversprechender Kandidat für komplexere Problemstellungen der Festkörperphysik.

Als erstes Beispiel untersuchen wir die Wechselwirkung von Wassermolekülen mit Kohlenstoffverbindungen an Hand zweier Fälle: Wasser auf Benzen und Wasser auf einer Graphenoberfläche. Unsere Ergebnisse zeigen gute Übereinstimmung mit einer weiteren korrelierten Methode: Diffusion Monte Carlo (DMC). Wir glauben daher, dass unsere gefundenen Werte als Richtwerte für die Entwicklung weiterer DFT Funktionale zur Beschreibung von Wasser-Kohlenstoff Wechselwirkungen dienen können. Ein Kernstück dieser Dissertation ist sicherlich die erfolgreiche Anwendung der RPA auf das bis dahin ungelöste *CO Adsorptions Rätsel*. Wir diskutieren die Adsorption eines Kohlenmonoxidmoleküls auf Cu, Ru, Rh, Pd und Pt. RPA ist gegenwärtig die einzige ab-initio Methode, welche sowohl die Adsorptionsenergie, als auch die Oberflächenenergie genau beschreibt und weiters die richtige Position des Moleküls auf der Metalloberfläche für jeden einzelnen Fall korrekt wiedergibt.

Contents

1	Introduction	1
I	Theoretical Background and Methods	5
2	The Many-Body Problem	7
3	Density Functional Theory	11
3.1	Hohenberg-Kohn Theorem	12
3.2	Kohn-Sham Equations	13
3.3	Approximations to the Exchange Correlation Functional	14
4	Adiabatic-Connection Fluctuation-Dissipation Theorem	17
4.1	Adiabatic-Connection Theorem	17
4.2	Fluctuation-Dissipation Theorem	19
5	The Random Phase Approximation	23
6	Random Phase Approximation in VASP	27
6.1	VASP - a Plane Wave Code in Reciprocal Space	27
6.2	Projector Augmented Wave Method	30
6.3	Implementation of RPA in VASP	34
6.3.1	Evaluation of the RPA Correlation Energy	34
6.3.2	Basis Set Convergence	36
6.3.3	Total RPA Energies	37
II	Results	39
7	Phonon Zero-Point Vibration Energies	41

8	Assessing the RPA	49
8.1	Method of Calculation	49
8.1.1	The HSEsol Functional	50
8.1.2	Settings for the RPA Calculations	52
8.2	Results	54
8.2.1	Lattice Constants	54
8.2.2	Bulk Moduli	57
8.2.3	Atomization Energies of Solids	59
8.2.4	Heats of Formation	62
8.3	Discussion	63
8.4	Conclusions	64
9	Carbon Water Interaction	67
9.1	Carbon Water Interaction: A Complex Problem Worthwhile a Closer Investigation	67
9.2	Computational Setup	68
9.3	Results	72
9.4	Discussion	75
9.5	Conclusions	78
10	CO Adsorption on Transition Metal Surfaces	79
10.1	Computational Setup and Methods	81
10.1.1	Settings for the Calculation of Surface Energies	82
10.1.2	Auxiliary Basis Set and k-point Extrapolation for Ad- sorption Energies	82
10.1.3	Applied Groundstate Geometries	86
10.2	Results	87
10.2.1	Surface Energies	87
10.2.2	Adsorption Energies	87
10.2.3	Summary	90
10.3	Discussion	90
10.4	Conclusion	94
11	Conclusions and Summary	95
A	Adiabatic Connection Fluctuation-Dissipation Theorem	99
A.1	Proof of Equation (4.5)	99
A.2	Proof of Equation (4.7)	100
A.3	Proof of Equation (4.11)	101
A.4	Proof of Equation (4.12)	101

A.5	Retarded Density-Density Response Function	102
A.6	Proof of Equation (4.16)	104
A.7	Retarded Kohn-Sham Density-Density Response Function . . .	104
B	Random Phase Approximation in VASP	107
B.1	Proof of Equation (6.5)	107
B.2	Proof of Equation (6.25)	108
C	Zero-Point Vibration Energies and Corrected Experimental Lattice Constants	109
C.1	The change in Equilibrium Energy due to Phonon Zero-Point Vibration Energies	109
C.2	The Change in Equilibrium Volume due to Phonon Zero-Point Vibration Energies	110
D	Assessing the RPA for Solids and Molecules	113
E	Carbon Water Interaction	117
E.1	Analytical Behaviour of the RPA Correlation Energy	117
	Bibliography	121
	Curriculum Vitae	129
	List of Publications	131

Chapter 1

Introduction

The subject of this thesis is the application of the random phase approximation (RPA) in the adiabatic-connection fluctuation-dissipation (ACFD) framework in solid state physics.

In the following, we will briefly discuss the history of this method, which dates back to the 1950s. For now, it shall suffice to state that the RPA within the ACFD theorem provides a formalism to calculate the (approximated) quantum mechanical total energy of atoms, molecules and solids. This is important, since nearly all, but in particular the macroscopic physical properties are related to total energies or differences of total energies. The equilibrium lattice constant of a crystal minimizes the total energy as a function of volume. The corresponding energy volume curve yields the bulk modulus of the crystal. The binding energy is the difference between the energy of a compound and that of its constituents. There are further examples, such as heats of formation, atomization energies, surface and adsorption energies; examples of each of these will be defined, calculated and compared to experiment in the results part of this thesis.

Why are such quantum mechanical simulations of materials properties important?

Quantum mechanical simulations can yield parameters that help to improve more empirical models which predict macroscopic materials properties. They can simulate situations, which are barely or not at all accessible in experiments. Furthermore, it may be preferable and cheaper to employ quantum mechanical simulations, even if experiments are possible. Finally, theory can narrow the range of possible constituents to design new materials with a desired property.

The 'ideal' quantum mechanical method reproduces available experimental data accurately, predicts hitherto unavailable experiments correctly and requires a minimum of computational resources. Unfortunately, due to the complexity of the many-body problem, this is not possible. On the one side, there are very accurate methods, such as the coupled-cluster approximation. However, since the scaling is very unfavourable (N^6 , where N is a measure of the system size), it is only possible to simulate small systems containing very few atoms. On the other side, density functional theory (DFT) is a very efficient method, within which even thousands of atoms can be simulated, but its results are of questionable quality in some cases. There exists a multitude of different functionals in DFT that are specialized either for the simulation of solids or molecules or even for the simulation of certain bonding situations. Nevertheless, in order to calculate e.g. the adsorption of a molecule at a surface accurately, a good description of the surface *and* the molecule is required at the same time. In such cases, present density functionals often fail to reproduce experimental results.

The RPA in the ACFD framework (scaling N^4) is more accurate than DFT and faster than coupled-cluster methods (but slower than DFT and less accurate than coupled-cluster methods). It is applicable to a system size of more than hundred atoms and is often able to grasp the right physics in situations, where density functional approximations (DFA) fail and more involved methods are too demanding in terms of computer power. Hence, RPA can successfully simulate materials and processes which were previously firmly within

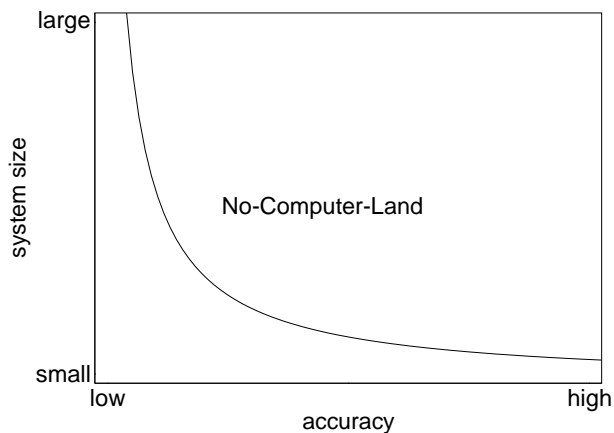


Figure 1.1: Schematic plot of the perpetual compromise between simulated system size and desired accuracy in quantum mechanical simulations.

'no-computer-land' before, see figure 1.1.

The ACFD theory is more than thirty years old and provides an exact expression for the correlation energy via the density-density response function of the respective system. This response function is in general unknown and has to be approximated, e.g. by the RPA which was first introduced by Nozières and Pines [1] in the late 1950s. Due to its high computational demand, the RPA has been disregarded for total energy calculations since its introduction. Instead, Kohn-Sham methods were usually applied in chemistry and solid state physics. With the tremendous advances in computer power, the RPA has moved back into focus and was recently applied to molecules [2, 3, 4] and extended systems [5, 6].

In the theory part we present the theoretical background, starting with a definition of the many-body problem, and ending with details of the implementation of RPA in the applied software package.

In chapter 8 of the results part we assess the quality of RPA for lattice constants, bulk moduli, atomization energies and heats of formation. We compare its performance to that of HSEsol, a hybrid functional specifically designed to describe solids we recently published, as well as to that of other methods. As some of the compared functionals yield very accurate results, phonon zero point vibrational energies are taken into account and the experimental data are corrected accordingly (see chapter 7).

In chapter 9 we investigate water-carbon interactions and compare the results to those of another correlated method: diffusion Monte Carlo (DMC). In chapter 10, we successfully apply the RPA to the long-standing and (within DFT) hitherto unsolved CO adsorption puzzle.

Part I

**Theoretical Background and
Methods**

Chapter 2

The Many-Body Problem

In solid state physics, we are mostly confronted with the many-body problem: matter consists of atoms interacting with each other, where each of these atoms consists of a certain number of electrons, which interact with the nuclei and with each other.

The time evolution of these electrons and nuclei is given by the time-dependent Schrödinger Equation (SE):

$$\begin{cases} i\frac{\partial}{\partial t}\Psi(t) = \hat{H}(t)\Psi(t) \\ \Psi(0) = \Psi_0. \end{cases} \quad (2.1)$$

This is the most general form and no representation is chosen yet. The SE as casted here is given in atomic units (a.u.), where e^2 , m_e , \hbar and $4\pi\epsilon_0$ equal 1 (As long as not otherwise stated atomic units are applied throughout this work). If the Hamiltonian \hat{H} is explicitly time-independent and under the assumption that ψ is an eigenstate of \hat{H} , one can make the ansatz

$$\Psi(t) = f(t)\psi \quad (2.2)$$

and divide the SE by $\Psi(t)$, which yields

$$\frac{\hat{H}\psi}{\psi} = i\frac{\frac{\partial}{\partial t}f(t)}{f(t)} \quad (2.3)$$

where the right hand side is dependent and the left hand side is independent of time. Thus, both sides have to equal a constant, here E .

$$\hat{H}\psi = E\psi \quad (2.4)$$

$$i\frac{\partial}{\partial t}f(t) = Ef(t) \quad (2.5)$$

It follows with $f(0)=1$

$$f(t) = e^{-iEt} \quad , \quad \Psi(t) = \psi e^{-iEt} \quad (2.6)$$

The solution of equation (2.5) is trivial, hence by applying this separation ansatz, we see that instead of an initial value problem (IVP, 2.1) we deal with an eigenvalue problem in the static case (2.4), where the eigenvalues correspond to the energy of the system. In the manifold of solutions $\psi = \{\psi_n\}$ and eigenvalues $E = \{E_n\}$, the index n refers to the number of excitation, where ψ_0 is to the ground state, whereas E_0 refers to the ground state energy of the system. The subject of this thesis is the description of (mainly) ground state properties of matter from theoretical methods firmly rooted in these fundamental equations. For the time being, let us restrict our considerations to the static, non-relativistic SE (2.4).

The static Hamiltonian for the system of nuclei and electrons is defined in the N -particle Hilbert space $\mathcal{H} \cong L^2(\mathbb{R}^{3N})$ and reads in spatial representation

$$\hat{H} = -\frac{1}{2} \sum_i \Delta_i - \sum_{i,I} \frac{Z_I}{|\mathbf{r}_i - \mathbf{R}_I|} + \frac{1}{2} \sum_{i \neq j} \frac{1}{|\mathbf{r}_i - \mathbf{r}_j|} - \sum_I \frac{1}{2M_I} \Delta_I + \frac{1}{2} \sum_{I \neq J} \frac{Z_I Z_J}{|\mathbf{R}_I - \mathbf{R}_J|} \quad (2.7)$$

where nuclei, with charge Z and mass M are denoted by upper case subscripts and electrons are denoted by lower case subscripts. The first and the fourth term describe the kinetic energy contribution of electrons and nuclei, respectively. The second term represents the Coulomb attraction between electrons and nuclei, the third and the fifth term represent the repulsion between electrons and between nuclei, respectively.

The fourth term on the right hand side in (2.7) can be regarded as small due to the large mass difference between electrons and nuclei. Assuming this, one can define a perturbation series in terms of $1/M_I$ in order to attain a decoupling of electronic and nuclei degrees of freedom, the Born-Oppenheimer Approximation [7]. Further, from now on, we omit the electrostatic interaction between the positive ions, which equals a constant for a fixed ionic configuration. The electronic Hamiltonian now reads

$$\hat{H} = \hat{T} + \hat{W} + \hat{V}_{\text{ext}} = -\frac{1}{2} \sum_i \Delta_i + \frac{1}{2} \sum_{i \neq j} \frac{1}{|\mathbf{r}_i - \mathbf{r}_j|} + \sum_i \hat{v}_{\text{ext}}(\mathbf{r}_i) \quad (2.8)$$

where \hat{v}_{ext} denotes the external potential. The corresponding SE becomes rapidly intractable with increasing system size. Every theory which is based on the information of the full wave function has to deal with an exponential growth of computational demand for many particle systems. For example even the simple storage of an N -electron wave function where each coordinate of each electron is discretized by only 10 points in each direction (x, y, z), results in a demand of 10^{3N} entries. Considering a single precision array one would have to provide disk space of 10^{3N} bytes. Even for small atoms this is not tractable. In short, the need for alternatives to the “direct“ solution of the SE is evident. A very successful example of such methods is the Density Functional Theory (DFT).

Chapter 3

Density Functional Theory

In DFT, the key quantity is the one particle density $n(\mathbf{r})$

$$n(\mathbf{r}) = N \int d^3r_2 d^3r_3 \dots d^3r_N \Psi^*(\mathbf{r}, \mathbf{r}_2, \dots, \mathbf{r}_N) \Psi(\mathbf{r}, \mathbf{r}_2, \dots, \mathbf{r}_N). \quad (3.1)$$

Here, contrary to the notation in chapter two, Ψ denotes the solution of the time-independent SE (2.4). The one particle density only depends on three arguments and consequently contains less information than the full many-body wavefunction. Still, the two following statements apply[9]:

- Every observable quantity of a quantum system can be calculated from the density of the system alone.
- The density of particles interacting with each other can be calculated as the density of an auxiliary system of non-interacting particles.

These two theorems demonstrate the beauty of DFT: It is possible to calculate any observable of interest of a complex many-body system by solving “simple” one particle equations. Furthermore, this theory is in principle exact. It is exact in the sense that for each system of interacting particles, there exists an auxiliary system of non-interacting particles which yields the exact density of particles of the fully interacting system. The theoretical foundation of DFT is provided by the Hohenberg-Kohn theorem[8], formulated by P. Hohenberg and W. Kohn in 1964.

3.1 Hohenberg-Kohn Theorem

In the presentation of the Hohenberg-Kohn theorem (HK-theorem) we follow R. M. Martin[10], Chapter 6.2. The starting point is the standard Hamiltonian of an interacting, fermionic, non relativistic, time-independent system (compare (2.8)).

$$\hat{H} = \hat{T} + \hat{W} + \hat{V}_{\text{ext}} = -\frac{1}{2} \sum_i \Delta_i + \frac{1}{2} \sum_{i \neq j} \frac{1}{|\mathbf{r}_i - \mathbf{r}_j|} + \sum_i \hat{v}_{\text{ext}}(\mathbf{r}_i) \quad (3.2)$$

For this Hamiltonian, two theorems are stated:

Theorem I For any system of interacting particles in an external potential $\hat{V}_{\text{ext}}(\mathbf{r})$, the potential $\hat{V}_{\text{ext}}(\mathbf{r})$ is determined uniquely, except for a constant, by the ground state particle density $n_0(\mathbf{r})$.

Since the Hamiltonian is thus fully determined (except for a constant shift in the energy), it follows that the many-body wavefunctions for ground and excited states are determined. Therefore all properties of the system are completely determined given only the ground state density $n_0(\mathbf{r})$ (see the first statement in the introduction of this chapter).

Theorem II A universal functional for the energy $E[n]$ in terms of the density $n(\mathbf{r})$ can be defined, valid for any external potential $\hat{V}_{\text{ext}}(\mathbf{r})$. For any particular $\hat{V}_{\text{ext}}(\mathbf{r})$, the exact ground state energy of the system is the global minimum value of this functional, and the density $n(\mathbf{r})$ that minimizes the functional is the exact ground state density $n_0(\mathbf{r})$.

The functional for the energy is usually expressed as

$$E_{\text{HK}}[n] = F_{\text{HK}}[n] + \int d^3r \hat{v}_{\text{ext}}(\mathbf{r})n(\mathbf{r}) \quad (3.3)$$

with

$$F_{\text{HK}}[n] = T[n] + W[n] = \langle \Psi[n] | \hat{T} + \hat{W} | \Psi[n] \rangle \quad (3.4)$$

being an universal (independent of the external potential) functional. If the functional $F_{\text{HK}}[n]$ was known, then by minimizing (3.3) with respect to variations in the density $n(\mathbf{r})$, one would find the exact ground state density and energy. However, $F_{\text{HK}}[n]$ is in general not known and has to be approximated.

3.2 Kohn-Sham Equations

The Kohn-Sham (KS) equations replace the intractable many-body problem by an auxiliary system which can be solved more easily (see second statement in the introduction of this chapter). The ansatz of Kohn-Sham [11] formulated in 1965 assumes that the one particle ground state density of a fully interacting system is equal to that of a chosen non-interacting system. This leads to independent-particle equations for the non-interacting system. These equations are solvable and contain all the difficult terms arising from many-body contributions in the so called exchange correlation functional $E_{\text{xc}}[n]$ of the density. The accuracy of this ansatz is only limited by the approximations in $E_{\text{xc}}[n]$. The KS approach is to rewrite (3.3) as

$$E_{\text{KS}}[n] = T_{\text{s}}[n] + \int d^3r \hat{v}_{\text{ext}}(\mathbf{r})n(\mathbf{r}) + E_{\text{Hartree}}[n] + E_{\text{xc}}[n]. \quad (3.5)$$

In this equation, $T_{\text{s}}[n]$ denotes the independent particle kinetic energy

$$T_{\text{s}}[n] = -\frac{1}{2} \sum_{i=1}^N \langle \psi_i | \Delta | \psi_i \rangle, \quad (3.6)$$

E_{Hartree} is the classical Coulomb interaction energy of the electron density $n(\mathbf{r})$

$$E_{\text{Hartree}}[n] = \frac{1}{2} \int d^3r d^3r' \frac{n(\mathbf{r})n(\mathbf{r}')}{|\mathbf{r} - \mathbf{r}'|} \quad (3.7)$$

and ψ_i is the i^{th} solution to the KS-equation

$$\hat{h}_{\text{KS}}\psi_i = \left(-\frac{1}{2}\Delta + \hat{v}_{\text{KS}}(\mathbf{r}) \right) \psi_i = \epsilon_i\psi_i. \quad (3.8)$$

The ψ_i are orthonormal

$$\langle \psi_i | \psi_j \rangle = \delta_{ij} \quad (3.9)$$

and the KS potential $\hat{v}_{\text{KS}}(\mathbf{r})$ is defined as

$$\hat{v}_{\text{KS}}(\mathbf{r}) = \hat{v}_{\text{ext}}(\mathbf{r}) + \frac{\delta E_{\text{Hartree}}}{\delta n(\mathbf{r})} + \frac{\delta E_{\text{xc}}}{\delta n(\mathbf{r})} = \hat{v}_{\text{ext}}(\mathbf{r}) + \hat{v}_{\text{H}}(\mathbf{r}) + \hat{v}_{\text{xc}}(\mathbf{r}). \quad (3.10)$$

For a system of N independent electrons that obeys (3.8), the ground state has one electron in each of the N orbitals $\psi_i(\mathbf{r})$ with the lowest eigenvalues ϵ_i of the Hamiltonian \hat{h}_{KS} . Thus, the ground state density of the auxiliary system is given by

$$n(\mathbf{r}) = \sum_i |\psi_i(\mathbf{r})|^2. \quad (3.11)$$

The KS potential (3.10) has to be found self-consistently via the repeated solution of the KS equations. We emphasize again that these equations would lead to the exact ground state density via (3.11) and energy via (3.5), if the exact functional $E_{\text{xc}}[n]$ was known.

3.3 Approximations to the Exchange Correlation Functional

An instructive expression for the exchange correlation functional $E_{\text{xc}}[n]$ can be found by comparing (3.3) to (3.5). It follows

$$E_{\text{xc}}[n] = \langle \Psi[n] | \hat{T} | \Psi[n] \rangle - T_{\text{s}}[n] + \langle \Psi[n] | \hat{W} | \Psi[n] \rangle - E_{\text{Hartree}}[n]. \quad (3.12)$$

This equation shows that $E_{\text{xc}}[n]$ must be a functional of n since the right-hand side consists of functionals of the density. Furthermore, it shows explicitly that $E_{\text{xc}}[n]$ is the difference of the kinetic and the electron-electron interaction energy from the many-body system compared to the auxiliary independent particle system. Therefore the exact expression for $E_{\text{xc}}[n]$ must be very complex, still, fairly accurate results have been obtained using remarkably simple

approximations.

The local density approximation (LDA) was first proposed by Kohn and Sham[11].

It reads

$$E_{xc}[n] = \int d^3r n(\mathbf{r})\epsilon_{xc}^{unif}(n(\mathbf{r})), \quad (3.13)$$

where $\epsilon_{xc}^{unif}(n(\mathbf{r}))$ is the exchange-correlation energy per particle of an electron gas with uniform density $n(\mathbf{r})$. The exchange energy of the homogeneous electron gas can be expressed analytically, whereas the correlation energy has to be calculated using Monte Carlo methods [12]. If the range of the effects of exchange and correlation is short in a particular system, the LDA should be a good approximation. The theory does not provide general evidence for such a behaviour. Consequently one must test the extent to which it works by actual applications. The LDA has been the standard for a long time in solid state physics but as it strongly overestimates atomization energies, it has not been very popular with the majority of quantum chemists. The atomization energies were greatly improved by the generalized gradient approximation (GGA)[13]

$$E_{xc}[n] = \int d^3r n(\mathbf{r})\epsilon_{xc}(n(\mathbf{r}), \nabla n(\mathbf{r})). \quad (3.14)$$

Here, the exchange correlation energy per particle depends on the density and on the gradient of the density. Accordingly this approximation is often denoted as semi-local. In equation (3.14) ϵ_{xc} is expressed as

$$\epsilon_{xc}(n(\mathbf{r}), \nabla n(\mathbf{r})) = \epsilon_x^{unif}(n(\mathbf{r}))F_{xc}(n(\mathbf{r}), \nabla n(\mathbf{r})), \quad (3.15)$$

where F_{xc} is the dimensionless enhancement factor over local exchange. GGA functionals can be tuned by increasing or decreasing the strength of this enhancement factor. As a result there exists a manifold of GGA functionals, each of which specialized for one class of problems. A very balanced and widely applied functional is the Perdew-Burke-Ernzerhof (PBE)[14] functional. The enhancement factor of the PBE x-functional is optimized with respect to physical constraints and reads

$$F_x(s) = 1 + \kappa - \frac{\kappa}{1 + \frac{\mu s^2}{\kappa}}, \quad (3.16)$$

with the parameters $\kappa = 0.804$ a.u. and $\mu = 0.21951$ a.u.. The dimensionless gradient s is defined as

$$s = \frac{|\nabla n|}{2k_{\text{F}}n} \Big|_{n=n(\mathbf{r})}, \quad (3.17)$$

where $k_{\text{F}} = (3\pi^2n)^{\frac{1}{3}}$ is the local fermi-vector. When s becomes zero then F_{x} becomes one and equation (3.15) equals the local density approximation. The enhancement factor for PBEsol has the same structure as the one for PBE but the parameter $\mu = 10/81$ is changed in order to improve equilibrium properties of densely packed solids and their surfaces [15]. We present a non exhaustive list of further functionals applied throughout this work: rPBE [16], Becke-Lee-Yang-Parr (BLYP)[17] and AM05[18]. rPBE has again the same formal structure as PBE and PBEsol but the parameters are chosen to yield increased enhancement factors and resultantly accurate adsorption energies. BLYP is an empirical functional which gradient's correction is stronger and which describes very accurately properties of molecules. AM05 is designed to enable an accurate treatment of systems with electronic surfaces with similar results as PBEsol, but with a different approach towards the gradient correction constructed using a subsystem approach.

Chapter 4

Adiabatic-Connection Fluctuation-Dissipation Theorem

4.1 Adiabatic-Connection Theorem

The Hamiltonian

$$\hat{H}_\lambda = \hat{T} + \hat{V}_{\text{ext}} + \hat{V}_\lambda + \lambda \hat{W}, \quad \lambda \in (0, 1) \quad (4.1)$$

describes a system with variable electron-electron interaction. The parameter λ determines the strength of the many body interaction. For $\lambda = 0$ the system is non interacting and $\Psi_{\lambda=0} = \Psi_0$ is the groundstate of \hat{H}_0 , whereas \hat{H}_1 describes the fully interacting system with groundstate Ψ_1 . \hat{V}_λ is a local potential that is chosen in such a way, that the ground state density is exact and therefore constant for every λ .

$$\begin{aligned} \hat{V}_0(\mathbf{r}_1 \dots \mathbf{r}_N) &= \sum_i \hat{v}_{\text{Hxc}}(\mathbf{r}_i) = \hat{V}_{\text{Hxc}}(\mathbf{r}_1 \dots \mathbf{r}_N) \\ \hat{V}_1 &= 0. \end{aligned} \quad (4.2)$$

\hat{T} is the kinetic energy operator, \hat{V}_{ext} is the external potential and \hat{v}_{Hxc} is the sum of Hartree and exchange-correlation potential as defined in equation (3.10). Ψ_λ is the ground state corresponding to \hat{H}_λ . Starting from the equality

$$\langle \Psi_1 | \hat{H}_1 | \Psi_1 \rangle - \langle \Psi_0 | \hat{H}_0 | \Psi_0 \rangle = \int_0^1 d\lambda \frac{d}{d\lambda} \langle \Psi_\lambda | \hat{H}_\lambda | \Psi_\lambda \rangle \quad (4.3)$$

we find for the left hand side

$$\langle \Psi_1 | \hat{T} + \hat{V}_{\text{ext}} + \hat{W} | \Psi_1 \rangle - \langle \Psi_0 | \hat{T} + \hat{V}_{\text{ext}} + \hat{V}_{\text{Hxc}} | \Psi_0 \rangle. \quad (4.4)$$

With¹

$$\langle \Psi_1 | \hat{V}_{\text{ext}} | \Psi_1 \rangle = \langle \Psi_0 | \hat{V}_{\text{ext}} | \Psi_0 \rangle \quad (4.5)$$

it follows that

$$\langle \Psi_1 | \hat{T} + \hat{W} | \Psi_1 \rangle - \langle \Psi_0 | \hat{T} + \hat{V}_{\text{Hxc}} | \Psi_0 \rangle. \quad (4.6)$$

Applying the Hellman-Feynman theorem to the right hand side of equation 4.3 and inserting²

$$\frac{d}{d\lambda} \langle \Psi_\lambda | \hat{V}_\lambda | \Psi_\lambda \rangle = \langle \Psi_\lambda | \frac{d}{d\lambda} \hat{V}_\lambda | \Psi_\lambda \rangle \quad (4.7)$$

yields

$$\begin{aligned} & \int_0^1 d\lambda \langle \Psi_\lambda | \frac{d\hat{H}_\lambda}{d\lambda} | \Psi_\lambda \rangle = \\ & = \int_0^1 d\lambda \langle \Psi_\lambda | \hat{W} | \Psi_\lambda \rangle + \int_0^1 d\lambda \frac{d}{d\lambda} \langle \Psi_\lambda | \hat{V}_\lambda | \Psi_\lambda \rangle \\ & = \int_0^1 d\lambda \langle \Psi_\lambda | \hat{W} | \Psi_\lambda \rangle + \langle \Psi_1 | \hat{V}_1 | \Psi_1 \rangle - \langle \Psi_0 | \hat{V}_0 | \Psi_0 \rangle \\ & = \int_0^1 d\lambda \langle \Psi_\lambda | \hat{W} | \Psi_\lambda \rangle + 0 - \langle \Psi_0 | \hat{V}_{\text{Hxc}} | \Psi_0 \rangle. \end{aligned} \quad (4.8)$$

Combining equation (4.6) and (4.8) gives

$$\langle \Psi_1 | \hat{T} + \hat{W} | \Psi_1 \rangle - \langle \Psi_0 | \hat{T} | \Psi_0 \rangle = \int_0^1 d\lambda \langle \Psi_\lambda | \hat{W} | \Psi_\lambda \rangle \quad (4.9)$$

¹see Appendix A.1

²see Appendix A.2

and finally with equations (3.4) and (3.5)

$$F_{\text{HK}}[n] - T_s = E_{\text{Hxc}} = \int_0^1 d\lambda \langle \Psi_\lambda | \hat{W} | \Psi_\lambda \rangle. \quad (4.10)$$

This is an exact expression for the Hartree exchange-correlation energy. The problem is that Ψ_λ is not known. Hence, expression (4.10) has to be cast in a form, which can be approximated in a sensible way.

4.2 Fluctuation-Dissipation Theorem

Equation (4.10) can be reformulated³ by virtue of the expression for the pair density $n^{2,\lambda}(\mathbf{r}_1, \mathbf{r}_2)$ as

$$E_{\text{Hxc}} = \int_0^1 d\lambda \langle \Psi_\lambda | \hat{W} | \Psi_\lambda \rangle = \frac{1}{2} \int d\lambda \int d^3r d^3r' \frac{n^{2,\lambda}(\mathbf{r}, \mathbf{r}')}{|\mathbf{r} - \mathbf{r}'|}. \quad (4.11)$$

Furthermore, the following equality holds⁴

$$\begin{aligned} \frac{1}{2} \int d^3r d^3r' \frac{n^{2,\lambda}(\mathbf{r}, \mathbf{r}')}{|\mathbf{r} - \mathbf{r}'|} &= \\ &= \frac{1}{2} \int d^3r d^3r' \frac{1}{|\mathbf{r} - \mathbf{r}'|} (\langle \Psi_\lambda | \hat{n}(\mathbf{r}) \hat{n}(\mathbf{r}') | \Psi_\lambda \rangle - \delta(\mathbf{r} - \mathbf{r}') \langle \Psi_\lambda | \hat{n}(\mathbf{r}) | \Psi_\lambda \rangle) \end{aligned} \quad (4.12)$$

where $\hat{n}(\mathbf{r})$ is the one particle density operator

$$\hat{n}(\mathbf{r}) = \sum_i \delta(\mathbf{r} - \mathbf{r}_i), \quad (4.13)$$

and $n^{2,\lambda}$ is defined as

$$n^{2,\lambda}(\mathbf{r}, \mathbf{r}') = N(N-1) \int d^3r_3 \dots d^3r_N |\Psi(\mathbf{r}, \mathbf{r}', \mathbf{r}_3 \dots \mathbf{r}_N)|^2. \quad (4.14)$$

The idea of the application of the fluctuation-dissipation theorem, first derived in Ref. [19], is to recast the expression for E_{Hxc} (4.10) with (4.12) in terms

³see Appendix A.3

⁴see Appendix A.4

of the retarded density-density response function χ_λ ⁵ at imaginary frequencies (and with limes $\eta \rightarrow 0$)(see also Ref.[20])

$$\begin{aligned} \chi_\lambda(\mathbf{r}, \mathbf{r}', i\omega) &= \\ &= \sum_{s \neq 0} \left(\frac{\langle \Psi_{0,\lambda} | \hat{n}(\mathbf{r}) | \Psi_{s,\lambda} \rangle \langle \Psi_{s,\lambda} | \hat{n}(\mathbf{r}') | \Psi_{0,\lambda} \rangle}{E_{0,\lambda} - E_{s,\lambda} + i\omega} + \frac{\langle \Psi_{0,\lambda} | \hat{n}(\mathbf{r}') | \Psi_{s,\lambda} \rangle \langle \Psi_{s,\lambda} | \hat{n}(\mathbf{r}) | \Psi_{0,\lambda} \rangle}{E_{0,\lambda} - E_{s,\lambda} - i\omega} \right). \end{aligned} \quad (4.15)$$

$\Psi_{0,\lambda}$ denotes the groundstate with energy $E_{0,\lambda}$ and $\Psi_{s,\lambda}$ the eigenstates with energies $E_{s,\lambda}$ of \hat{H}_λ . As a result, we get with the short hand notation $|\Psi_0, \lambda\rangle = |0, \lambda\rangle$ ⁶

$$\int_0^\infty d\omega (\chi_\lambda(\mathbf{r}, \mathbf{r}', i\omega) + \chi_\lambda(\mathbf{r}', \mathbf{r}, i\omega)) = -2\pi(\langle 0, \lambda | \hat{n}(\mathbf{r}) \hat{n}(\mathbf{r}') | 0, \lambda \rangle + n(\mathbf{r})n(\mathbf{r}')) \quad (4.16)$$

We can now insert equation (4.16) in (4.12, $|\Psi_\lambda\rangle$ is equal to $|0, \lambda\rangle$) and obtain with (4.11)

$$\begin{aligned} E_{\text{Hxc}} &= \\ &- \int_0^1 d\lambda \frac{1}{2} \int d^3r d^3r' \frac{1}{|\mathbf{r} - \mathbf{r}'|} \left(\frac{1}{\pi} \int_0^\infty d\omega \chi_\lambda(\mathbf{r}, \mathbf{r}', i\omega) + \delta(\mathbf{r} - \mathbf{r}')n(\mathbf{r}) + n(\mathbf{r})n(\mathbf{r}') \right) \end{aligned} \quad (4.17)$$

The last term in the right hand side of equation (4.17) is the Hartree energy. Accordingly we can write

$$E_{\text{xc}} = - \int_0^1 d\lambda \frac{1}{2} \int d^3r d^3r' \frac{1}{|\mathbf{r} - \mathbf{r}'|} \left(\frac{1}{\pi} \int_0^\infty d\omega \chi_\lambda(\mathbf{r}, \mathbf{r}', i\omega) + \delta(\mathbf{r} - \mathbf{r}')n(\mathbf{r}) \right). \quad (4.18)$$

Furthermore, when the retarded Kohn-Sham density-density response function⁷

$$\chi^{\text{KS}}(\mathbf{r}, \mathbf{r}', i\omega) = \sum_n^{\text{occ}} \sum_m^{\text{uocc}} \left(\frac{\psi_n^*(\mathbf{r})\psi_m(\mathbf{r})\psi_m^*(\mathbf{r}')\psi_n(\mathbf{r}')}{\epsilon_n - \epsilon_m + i\omega} + \frac{\psi_n^*(\mathbf{r}')\psi_m(\mathbf{r}')\psi_m^*(\mathbf{r})\psi_n(\mathbf{r})}{\epsilon_n - \epsilon_m - i\omega} \right). \quad (4.19)$$

⁵see Appendix A.5

⁶see Appendix A.6

⁷see Appendix A.7

is substituted for χ_λ , (4.18) yields the exact exchange energy, evaluated with Kohn-Sham orbitals.

$$E_{xc}[\chi^{\text{KS}}] = E_x\{\psi_i\} = -\frac{1}{2} \sum_n^{\text{occ}} \sum_m^{\text{occ}} \int d^3r d^3r' \frac{\psi_m^*(\mathbf{r}')\psi_n(\mathbf{r}')\psi_n^*(\mathbf{r})\psi_m(\mathbf{r})}{|\mathbf{r} - \mathbf{r}'|} \quad (4.20)$$

Here we used $n(\mathbf{r}) = \sum_i^{\text{occ}} \psi_i^*(\mathbf{r})\psi_i(\mathbf{r})$ and $\sum_m \psi_m^*(\mathbf{r}')\psi_m(\mathbf{r}) = \delta(\mathbf{r} - \mathbf{r}')$ and the definition of χ^{KS} (4.19). Consequently, we can separate exchange and correlation energy.

$$E_c = - \int_0^1 d\lambda \frac{1}{2} \int d^3r d^3r' \frac{1}{|\mathbf{r} - \mathbf{r}'|} \left(\frac{1}{\pi} \int_0^\infty d\omega (\chi_\lambda(\mathbf{r}, \mathbf{r}', i\omega) - \chi^{\text{KS}}(\mathbf{r}, \mathbf{r}', i\omega)) \right) \quad (4.21)$$

$$E_x = - \int_0^1 d\lambda \frac{1}{2} \int d^3r d^3r' \frac{1}{|\mathbf{r} - \mathbf{r}'|} \left(\frac{1}{\pi} \int_0^\infty d\omega \chi^{\text{KS}}(\mathbf{r}, \mathbf{r}', i\omega) + \delta(\mathbf{r} - \mathbf{r}')n(\mathbf{r}) \right) \quad (4.22)$$

In summary the Adiabatic-Connection Fluctuation-Dissipation theorem yields an expression for the correlation energy in terms of the density-density response function which is in principle exact and compatible to the exact exchange energy in the DFT sense. By DFT sense we mean that the exact exchange energy is evaluated non self-consistently with Kohn-Sham orbitals as input. However, it is important to note that the correlation energy here is not the difference of the exact ground state energy and the self-consistent Hartree-Fock energy, which is the usual quantum chemists definition. Still, equations (4.21) and (4.22) are exact, provided we would know χ_λ .

Chapter 5

The Random Phase Approximation

To derive an expression for χ_λ in (4.21) we follow the reasoning in [21], relying on time-dependent density functional theory. We consider an unperturbed inhomogeneous electronic system with ground state density $n_0(\mathbf{r})$ and external potential $v_{\text{ext}}(\mathbf{r})$. The linear density response to a small perturbation $\delta v_{\text{ext}}(\mathbf{r})$ is denoted by $\delta n_0(\mathbf{r})$ and reads in frequency space

$$\delta n_0(\mathbf{r}, \omega) = \int d^3r' \chi(\mathbf{r}, \mathbf{r}', \omega) \delta v_{\text{ext}}(\mathbf{r}', \omega), \quad (5.1)$$

where

$$\chi(\mathbf{r}, \mathbf{r}', \omega) = \frac{\delta n_0(\mathbf{r}, \omega)}{\delta v_{\text{ext}}(\mathbf{r}', \omega)} \quad (5.2)$$

is the exact density-density response function. Under the assumption that $n_0(\mathbf{r}) + \delta n_0(\mathbf{r}, t)$ is non-interacting v representable and thus can be reproduced by a system of non-interacting electrons in a corresponding single particle potential $v_{\text{KS}}(\mathbf{r}) + \delta v_{\text{KS}}(\mathbf{r}, t)$, we can write

$$\delta n_0(\mathbf{r}, \omega) = \int d^3r' \chi^{\text{KS}}(\mathbf{r}, \mathbf{r}', \omega) \delta v_{\text{KS}}(\mathbf{r}', \omega), \quad (5.3)$$

where

$$\chi^{\text{KS}}(\mathbf{r}, \mathbf{r}', \omega) = \frac{\delta n_0(\mathbf{r}, \omega)}{\delta v_{\text{KS}}(\mathbf{r}', \omega)} \quad (5.4)$$

is the Kohn-Sham density-density response function as defined in (4.19). Further, we define δv_{KS} as

$$\delta v_{\text{KS}}(\mathbf{r}, \omega) = \delta v_{\text{ext}}(\mathbf{r}, \omega) + \int d^3 r' \frac{\delta n_0(\mathbf{r}, \omega)}{|\mathbf{r} - \mathbf{r}'|} + \delta v_{\text{xc}}(\mathbf{r}, \omega) \quad (5.5)$$

and δv_{xc} as a linear functional of δn_0

$$\delta v_{\text{xc}}(\mathbf{r}, \omega) = \int d^3 r' f_{\text{xc}}(\mathbf{r}, \mathbf{r}', \omega) \delta n_0(\mathbf{r}', \omega), \quad (5.6)$$

where the exchange-correlation kernel f_{xc} depends on the unperturbed ground state density n_0 . From equation (5.5) follows with (5.2), (5.4) and (5.6)

$$\chi_{\text{KS}}^{-1}(\mathbf{r}, \mathbf{r}', \omega) = \chi^{-1}(\mathbf{r}, \mathbf{r}', \omega) + \frac{1}{|\mathbf{r} - \mathbf{r}'|} + f_{\text{xc}}(\mathbf{r}, \mathbf{r}', \omega) \quad (5.7)$$

or written differently

$$\begin{aligned} \chi(\mathbf{r}, \mathbf{r}', \omega) = & \chi^{\text{KS}}(\mathbf{r}, \mathbf{r}', \omega) + \\ & + \int d^3 r_1 \int d^3 r_2 \chi^{\text{KS}}(\mathbf{r}, \mathbf{r}_1, \omega) (v(\mathbf{r}_1, \mathbf{r}_2) + f_{\text{xc}}(\mathbf{r}_1, \mathbf{r}_2, \omega)) \chi(\mathbf{r}_2, \mathbf{r}', \omega) \end{aligned} \quad (5.8)$$

where v denotes the Coulomb kernel

$$v(\mathbf{r}, \mathbf{r}') = \frac{1}{|\mathbf{r} - \mathbf{r}'|}. \quad (5.9)$$

The Dyson like equation (5.8) links $\chi_{\lambda=0}^{\text{KS}}$ and $\chi_{\lambda=1}$ but also holds for arbitrary λ .

$$\begin{aligned} \chi_{\lambda}(\mathbf{r}, \mathbf{r}', \omega) = & \chi^{\text{KS}}(\mathbf{r}, \mathbf{r}', \omega) + \\ & + \int d^3 r_1 \int d^3 r_2 \chi^{\text{KS}}(\mathbf{r}, \mathbf{r}_1, \omega) (\lambda v(\mathbf{r}_1, \mathbf{r}_2) + f_{\text{xc}}^{\lambda}(\mathbf{r}_1, \mathbf{r}_2, \omega)) \chi_{\lambda}(\mathbf{r}_2, \mathbf{r}', \omega) \end{aligned} \quad (5.10)$$

The exchange-correlation kernel f_{xc} is, except for initially homogeneous systems ($n_0(\mathbf{r}) = \text{const.}$), not explicitly known and has to be approximated. In

the Random Phase Approximation (RPA) the exchange-correlation kernel is set to zero and equation (5.10) then reads

$$\begin{aligned} \chi_{\lambda}^{\text{RPA}}(\mathbf{r}, \mathbf{r}', \omega) = & \chi^{\text{KS}}(\mathbf{r}, \mathbf{r}', \omega) + \\ & + \int d^3r_1 \int d^3r_2 \chi^{\text{KS}}(\mathbf{r}, \mathbf{r}_1, \omega) \lambda v(\mathbf{r}_1, \mathbf{r}_2) \chi_{\lambda}^{\text{RPA}}(\mathbf{r}_2, \mathbf{r}', \omega) \end{aligned} \quad (5.11)$$

Inserting the above equation into (4.21) we finally obtain

$$\begin{aligned} E_c^{\text{RPA}} = & \\ = - \int_0^1 d\lambda \frac{1}{2} \int d^3r d^3r' \frac{1}{|\mathbf{r} - \mathbf{r}'|} & \left(\frac{1}{\pi} \int_0^{\infty} d\omega (\chi_{\lambda}^{\text{RPA}}(\mathbf{r}, \mathbf{r}', i\omega) - \chi^{\text{KS}}(\mathbf{r}, \mathbf{r}', i\omega)) \right). \end{aligned} \quad (5.12)$$

Taken the last two chapters together, we have seen that the ACFDT yields an expression for the correlation energy (4.21), which is compatible with exact exchange in the DFT sense (4.22) and in principle exact, but dependent on the exact density-density response function χ_{λ} .

A Dyson like equation (5.10) allows to determine χ_{λ} self-consistently, provided the exchange-correlation kernel f_{xc} is known. f_{xc} , however, is known only for initially homogenous electron densities. The RPA “approximates” f_{xc} by setting it to zero, so that we can calculate $\chi_{\lambda}^{\text{RPA}}$ self consistently and finally end up with an expression for the correlation energy, which requires only occupied and unoccupied Kohn-Sham orbitals for its evaluation.

Chapter 6

Random Phase Approximation in VASP

This chapter deals with the evaluation of total energies within the RPA as implemented in the Vienna ab-initio Simulation Package (VASP)[22, 23].

6.1 VASP - a Plane Wave Code in Reciprocal Space

The Vienna Ab-initio Simulation Package (VASP) enables the user to study and predict macroscopic properties of solid materials by simulating the interaction of electrons and nuclei at quantum mechanical level. For the properties to be macroscopic and in order to avoid effects in the boundary region, we have to mathematically describe crystals of (almost) infinite size. This implies the necessity to simulate an infinite number of - in the case of DFT - non-interacting electrons moving in a periodic potential of an infinite number of nuclei or ions. As a result, an infinite number of wave functions has to be calculated, where each of which extends over the entire bulk and thus requires an infinite basis. This seems like an impossible task but fortunately Bloch's

theorem in combination with Born-von Karman periodic boundary conditions and a well chosen k-point sampling grid of the First Brillouin Zone surmounts this problem.

We consider a crystal defined on a Bravais lattice spanned by a set of primitive vectors \mathbf{a}_1 , \mathbf{a}_2 and \mathbf{a}_3 . Bloch's theorem states that an eigenstate of the one electron Hamiltonian $\hat{H} = -\frac{1}{2}\Delta + \hat{v}(\mathbf{r})$ with a periodic potential $\hat{v}(\mathbf{r})$, where $\hat{v}(\mathbf{r} + \mathbf{R}) = \hat{v}(\mathbf{r})$ for all \mathbf{R} in the Bravais lattice, can be written as the product of a cell-periodic part $u(\mathbf{r})$ and a plane wave

$$\psi_{n\mathbf{k}}(\mathbf{r}) = u_{n\mathbf{k}}(\mathbf{r})e^{i\mathbf{k}\mathbf{r}}, \quad (6.1)$$

where

$$\mathbf{k} = x_1\mathbf{b}_1 + x_2\mathbf{b}_2 + x_3\mathbf{b}_3, \quad (6.2)$$

with \mathbf{b}_i being the reciprocal lattice vectors satisfying $\mathbf{a}_i \cdot \mathbf{b}_j = 2\pi\delta_{ij}$ and the x_i are in the most general case complex numbers¹. For each \mathbf{k} exists a discrete set of eigenstates which are labeled with the band index n and which can be calculated separately.

The Born-von Karman (BVK) periodic boundary conditions for the eigenstates ψ impose conditions on the x_i in equation (6.2) and thus limit the number of allowed \mathbf{k} in equation (6.1). The BVK periodic boundary conditions read

$$\psi(\mathbf{r} + \mathbf{T}(N_1, N_2, N_3)) = \psi(\mathbf{r}), \quad (6.3)$$

where the N_i define the crystal size and \mathbf{T} is any translation defined as

$$\mathbf{T}(n_1, n_2, n_3) = n_1\mathbf{a}_1 + n_2\mathbf{a}_2 + n_3\mathbf{a}_3, \quad n_i \in \mathbb{Z} \quad (6.4)$$

with \mathbf{a}_i being primitive vectors of the Bravais lattice. By inserting (6.3) in Bloch's theorem (6.1) it follows directly² that only \mathbf{k} vectors of the form

$$\mathbf{k} = \frac{m_1}{N_1}\mathbf{b}_1 + \frac{m_2}{N_2}\mathbf{b}_2 + \frac{m_3}{N_3}\mathbf{b}_3, \quad m_i \in \mathbb{Z}_{N_i} \quad (6.5)$$

¹We will see that for suitable boundary conditions the x_i must be real

²see Appendix B.1

are allowed. According to the above equation the reciprocal volume $\Delta\mathbf{k}$ per allowed value of \mathbf{k} is given by

$$\Delta\mathbf{k} = \frac{\mathbf{b}_1}{N_1} \cdot \left(\frac{\mathbf{b}_2}{N_2} \times \frac{\mathbf{b}_3}{N_3} \right) = \frac{1}{N} \mathbf{b}_1 \cdot (\mathbf{b}_2 \times \mathbf{b}_3) = \frac{\Omega}{N}, \quad (6.6)$$

where Ω denotes the volume of a reciprocal primitive cell and N is the total number of unit cells in the crystal. This has the consequence that the number of allowed \mathbf{k} vectors in a primitive cell of the reciprocal lattice, e.g. the First Brillouin Zone, is equal to the number of unit cells in the regarded crystal. We see now, that for an infinitely extended crystal, we would have to solve the SE for an infinite number of \mathbf{k} vectors. This is obviously not possible and not necessary, since $\Psi_{n\mathbf{k}}$ is expected to be smooth and thus very similar for \mathbf{k} vectors that are close together. Thus, the First Brillouin Zone is sampled by a finite number of special points in reciprocal space which fulfill equation (6.5). For RPA calculations we applied the scheme of Monkhorst and Pack [24].

The cell periodic part $u(\mathbf{r})$ of (6.1) can be expanded in terms of a discrete set of plane waves whose wave vectors \mathbf{G} are reciprocal lattice vectors

$$u_{n\mathbf{k}}(\mathbf{r}) = \sum_{\mathbf{G}} c_{n\mathbf{k}+\mathbf{G}} e^{i\mathbf{G}\mathbf{r}}, \quad (6.7)$$

where the expansion factors $c_{n\mathbf{k}+\mathbf{G}}$ are defined as

$$c_{n\mathbf{k}+\mathbf{G}} = \frac{1}{\Omega} \int_{\Omega} d^3r u_{n\mathbf{k}}(\mathbf{r}) e^{-i\mathbf{G}\mathbf{r}}. \quad (6.8)$$

As a result we can write the electronic wavefunction as

$$\psi_{n\mathbf{k}}(\mathbf{r}) = \sum_{\mathbf{G}} c_{n\mathbf{k}+\mathbf{G}} e^{i(\mathbf{k}+\mathbf{G})\mathbf{r}}. \quad (6.9)$$

In principle an infinite plane wave basis set is required for this expansion, fortunately, the coefficients $c_{n\mathbf{k},\mathbf{G}}$ for plane waves with small kinetic energy $\frac{|\mathbf{k}+\mathbf{G}|^2}{2}$ are typically more important than those with large kinetic energy. Thus the basis set can be truncated at some G_{\max} .

$$\psi_{n\mathbf{k}}(\mathbf{r}) = \sum_{|\mathbf{G}| < G_{\max}} c_{n\mathbf{k}+\mathbf{G}} e^{i(\mathbf{k}+\mathbf{G})\mathbf{r}} \quad (6.10)$$

Consequently, the one particle eigenstates can be represented by a finite and discrete set of plane waves and the First Brillouin Zone is sampled by k-points on a grid of special points.

6.2 Projector Augmented Wave Method

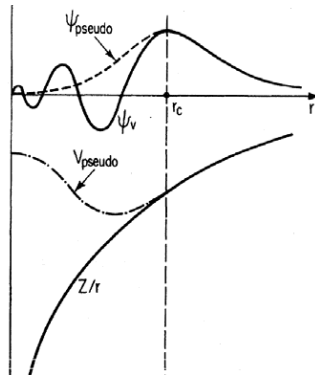


Figure 6.1: Schematic illustration of all-electron (solid lines) and pseudo electron (dashed lines) potentials and their corresponding wave functions. The radius at which all-electron and pseudo electron values match is the core radius r_c . The figure was originally published in [25].

The plane wave basis is only poorly suited to expand the electronic wavefunctions of core electrons or valence electrons in the core region. Core electrons are the electrons in the vicinity of the nucleus which do not participate in the formation of chemical bonds as opposed to valence electrons. Due to the Pauli principle, electronic wavefunctions must be orthogonal to each other which implicates oscillations of the wavefunctions. Hence, a very large value of G_{\max} in equation (6.10) would be needed for the expansion into plane waves which makes the calculations extremely slow. In VASP, the bare Coulomb potential of the nuclei and the potential of the core electrons is replaced by a 'softer' potential. Solving the KS-equations for this 'soft' pseudopotential yields a pseudo

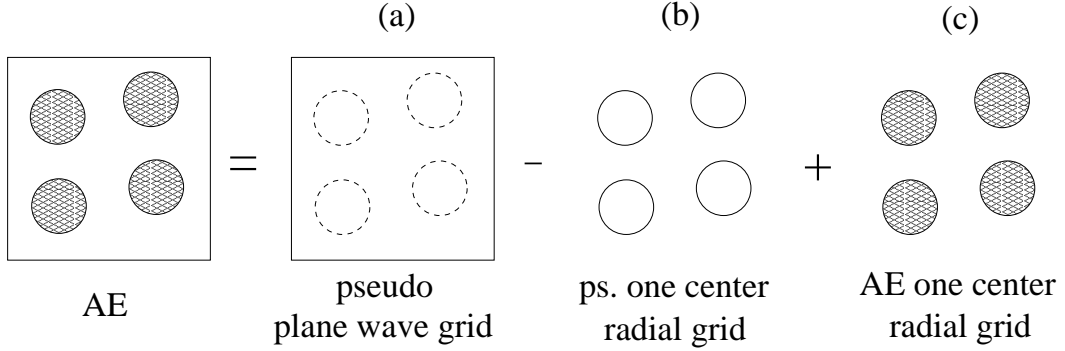


Figure 6.2: Illustration of the PAW method. (a) Pseudized quantities are defined in the entire space on a regular plane wave grid. (b) The pseudo wave functions are reconstructed inside atom centered augmentation regions and the corresponding one center energy terms are subtracted. (c) The AE wave functions are constructed as well and the AE one center energies are added.

wavefunction which has the same behaviour as the original wave function outside the core radius r_c (see figure 6.1), but its representation requires a much smaller plane wave basis. To restore the all-electron wavefunction VASP employs the PAW method. In the PAW method[27], space is divided into spherical, atom centered augmentation regions Ω_a and the interstitial region Ω_I between these spheres. The all electron (AE) wave functions $\psi_{n\mathbf{k}}$ are derived from the pseudo (PS) wavefunctions $\tilde{\psi}_{n\mathbf{k}}$ by means of a linear transformation:

$$|\psi_{n\mathbf{k}}\rangle = |\tilde{\psi}_{n\mathbf{k}}\rangle + \sum_i (|\phi_i\rangle - |\tilde{\phi}_i\rangle) \langle \tilde{p}_i | \tilde{\psi}_{n\mathbf{k}} \rangle. \quad (6.11)$$

The AE partial waves ϕ_i are solutions to the all electron KS equation for a spherical reference atom. The nodeless PS wave functions $\tilde{\psi}_{n\mathbf{k}}$ are the variational quantity and are represented by an expansion into plane waves:

$$\begin{aligned} \tilde{\psi}_{n\mathbf{k}} &= \sum_i \langle \tilde{p}_i | \tilde{\psi}_{n\mathbf{k}} \rangle |\tilde{\phi}_i\rangle && \text{in } \Omega_a \\ \tilde{\psi}_{n\mathbf{k}} &= \psi_{n\mathbf{k}} && \text{in } \Omega_I. \end{aligned} \quad (6.12)$$

The first line in equation 6.12 holds only for a complete set

$$\sum_i |\tilde{\phi}_i\rangle\langle\tilde{p}_i| = 1 \quad (6.13)$$

which is usually not the case and resultantly we write

$$\tilde{\psi}_{n\mathbf{k}} = \sum_{\mathbf{G}} c_{n,\mathbf{k}+\mathbf{G}} e^{i(\mathbf{k}+\mathbf{G})\mathbf{r}} \quad \text{in } \Omega_a. \quad (6.14)$$

The representation of the PS wave function $\tilde{\psi}_{n\mathbf{k}}$ requires only a modest number of plane waves because the AE partial waves ϕ_i with their rapid oscillations near the atomic core region Ω_a are replaced by the smooth PS partial waves $\tilde{\phi}_i$. The index i in the above equations is an abbreviation for the atomic site \mathbf{R} , the momentum number $L = l, m$ and an additional index k referring to the reference energy ϵ_{kl} corresponding to the AE partial waves. The projector functions \tilde{p}_i are dual to the partial waves:

$$\langle\tilde{p}_i|\tilde{\phi}_j\rangle = \delta_{ij}. \quad (6.15)$$

The AE and PS partial waves constitute a local basis set on radial logarithmic grids within the atom centered augmentation region Ω_a and are imported from an atomic pseudo potential generation code.

Taken all these informations together we can summarize: Pseudized quantities are defined in the entire space on a regular plane wave grid. The nodeless PS wave functions $\tilde{\psi}_{n\mathbf{k}}$ are the variational quantity and only a modest number of plane waves are necessary for an accurate expansion. To obtain AE energies, the pseudo wave functions are reconstructed on a radial grid inside atomic centered spheres and the corresponding one center terms are subtracted. Furthermore, the AE wave functions are reconstructed as well and the AE one center terms are added (see equation (6.11)).

Starting from equation (6.11), it can be shown that in the PAW formalism,

the AE charge density is given by three terms³(for details see [26]).

$$n(\mathbf{r}) = \tilde{n}(\mathbf{r}) + n^1(\mathbf{r}) - \tilde{n}^1(\mathbf{r}), \quad (6.16)$$

where the pseudo charge density \tilde{n} is directly calculated from the PS wave functions on a plane wave grid:

$$\tilde{n}(\mathbf{r}) = \sum_n f_n \tilde{\psi}_{n\mathbf{k}}^*(\mathbf{r}) \tilde{\psi}_{n\mathbf{k}}(\mathbf{r}). \quad (6.17)$$

The onsite or 'one-center' charge densities n^1 and \tilde{n}^1 are treated on a radial grid and are defined as

$$n^1(\mathbf{r}) = \sum_{ij} \rho_{ij} \phi_i^*(\mathbf{r}) \phi_j(\mathbf{r}) \quad (6.18)$$

and

$$\tilde{n}^1(\mathbf{r}) = \sum_{ij} \rho_{ij} \tilde{\phi}_i^*(\mathbf{r}) \tilde{\phi}_j(\mathbf{r}), \quad (6.19)$$

where the occupancies ρ_{ij} are calculated from the pseudo wave functions by means of the projector functions:

$$\rho_{ij} = \sum_n f_n \langle \tilde{\psi}_{n\mathbf{k}} | \tilde{p}_i \rangle \langle \tilde{p}_j | \tilde{\psi}_{n\mathbf{k}} \rangle, \quad (6.20)$$

where f_n is 1 for occupied and 0 for unoccupied states. Inside Ω_a , the onsite charge density \tilde{n}^1 is exactly the same as \tilde{n} for a complete set of projectors. For the total energy, an analogous separation $E = \tilde{E} + E^1 - \tilde{E}^1$ into terms arising from quantities represented on a regular plane wave grid and on a radial grid is possible, if one introduces the compensation charge density \hat{n} . The compensation charge density \hat{n} restores for $\tilde{n}^1 + \hat{n}$ the same moments as the exact AE charge density n^1 within each atom centered augmentation sphere at \mathbf{R} . For more details see section II.D and II.E in [27].

Furthermore, VASP applies the frozen core approximation, where the deeper lying core electrons are described by solutions according to a reference atom (for more details see section II.A in [27]).

³This equation is only exact for a complete set of projectors

6.3 Implementation of RPA in VASP

A more detailed description of the implementation of RPA total energies in VASP is provided in [28, 29]. Here, we will only discuss the most important steps which are necessary to understand the calculations which are presented in the results part of this thesis.

6.3.1 Evaluation of the RPA Correlation Energy

VASP performs the integration over the coupling parameter λ in equation (5.12) analytically. To explain how it works, we start from this very expression (5.12) for the RPA correlation energy but given per unit cell in reciprocal space:

$$\begin{aligned}
 E_c^{\text{RPA}} &= \\
 &= - \int_0^1 d\lambda \frac{1}{2\pi} \int_0^\infty d\omega \sum_{\mathbf{q} \in \text{BZ}} g_{\mathbf{q}} \sum_{\substack{|\mathbf{G}+\mathbf{q}| < G_{\text{max}} \\ |\mathbf{G}'+\mathbf{q}| < G_{\text{max}}}} \nu_{\mathbf{G},\mathbf{G}'} \left(\chi_{\mathbf{G},\mathbf{G}'}^{\lambda,\text{RPA}}(\mathbf{q}, i\omega) - \chi_{\mathbf{G},\mathbf{G}'}^{\text{KS}}(\mathbf{q}, i\omega) \right),
 \end{aligned} \tag{6.21}$$

where the Coulomb kernel $\nu_{\mathbf{G},\mathbf{G}'}$ is defined as (in a.u.)

$$\nu_{\mathbf{G},\mathbf{G}'} = \frac{4\pi}{|\mathbf{q} + \mathbf{G}|^2} \delta_{\mathbf{G},\mathbf{G}'} \tag{6.22}$$

and the k-point weights $g_{\mathbf{q}}$ are chosen such that the Brillouin zone is correctly sampled for a given set of k-points. With the short hand notation

$$\text{Tr}\{AB\} = \sum_{\mathbf{q} \in \text{BZ}} g_{\mathbf{q}} \sum_{\substack{|\mathbf{G}+\mathbf{q}| < G_{\text{max}} \\ |\mathbf{G}'+\mathbf{q}| < G_{\text{max}}}} A_{\mathbf{G},\mathbf{G}'}(\mathbf{q}) B_{\mathbf{G},\mathbf{G}'}(\mathbf{q}) \tag{6.23}$$

we can reformulate (6.21) as

$$E_c^{\text{RPA}} = - \int_0^1 d\lambda \frac{1}{2\pi} \int_0^\infty d\omega \text{Tr}\{\nu (\chi^{\lambda,\text{RPA}}(i\omega) - \chi^{\text{KS}}(i\omega))\}. \tag{6.24}$$

Inserting the equality

$$\text{Tr}\{\nu \chi^{\lambda,\text{RPA}}(i\omega)\} = - \frac{\partial}{\partial \lambda} \text{Tr}\{\ln[1 - \lambda \chi^{\text{KS}}(i\omega) \nu]\} \tag{6.25}$$

into (6.21) yields⁴

$$E_c^{\text{RPA}} = \frac{1}{2\pi} \int_0^\infty d\omega \text{Tr}\{\ln[1 - \chi^{\text{KS}}(i\omega)\nu] + \chi^{\text{KS}}(i\omega)\nu\}. \quad (6.26)$$

With this analytical trick, the costly numerical integration over the coupling parameter can be avoided. However, the frequency integration and the evaluation of the integrand $\text{Tr}\{\ln[1 - \chi^{\text{KS}}\nu] + \chi^{\text{KS}}\nu\}$ in this equation is left for discussion. With

$$\text{Tr}\{\ln[1 - AB]\} = -\text{Tr}\{AB\} - \frac{1}{2}\text{Tr}\{ABAB\} - \frac{1}{3}\text{Tr}\{ABABAB\} - \dots \quad (6.27)$$

and

$$\text{Tr}\{\chi^{\text{KS}}\nu\} = \text{Tr}\{\chi^{\text{KS}}\nu^{\frac{1}{2}}\nu^{\frac{1}{2}}\} = \text{Tr}\{\nu^{\frac{1}{2}}\chi^{\text{KS}}\nu^{\frac{1}{2}}\} \quad (6.28)$$

and noting that $S = \nu^{\frac{1}{2}}\chi^{\text{KS}}\nu^{\frac{1}{2}}$ is hermitian and can be diagonalized yielding real eigenvalues d_i

$$\sum_{k,l} C_{ik}^{-1} S_{kl} C_{lj} = d_i \delta_{ij} \quad (6.29)$$

we find that the integrand of equation (6.26) can be evaluated as

$$\text{Tr}\{\ln[1 - \chi^{\text{KS}}\nu]\} + \text{Tr}\{\chi^{\text{KS}}\nu\} = \sum_i \ln(1 - d_i) + d_i. \quad (6.30)$$

The number of frequency points for the frequency integration enters the computational cost linearly. Thus, although the response function $\chi^{\text{KS}}(i\omega)$ is a smooth function of the imaginary frequency, an optimal choice for the frequency grid is desirable. A Gauss-Legendre integration scheme is implemented where the weights and supporting points are tabulated in VASP for up to 64 supporting points:

$$\int_0^\infty f(x) dx = \sum_i^N w_i f(x_i) \quad (6.31)$$

The smallest frequency is set to the value of SIGMA provided in the INCAR file.

⁴see Appendix B.2

6.3.2 Basis Set Convergence

The independent particle response function $\chi^{\text{KS}}(i\omega)$ in equation (6.26) is given by the expression of Adler and Wiser [30, 31]

$$\begin{aligned} \chi_{\mathbf{G},\mathbf{G}'}^{\text{KS}}(\mathbf{q}, i\omega) &= \\ &= \frac{1}{\Omega} \sum_{n,n',\mathbf{k}} 2g_{\mathbf{k}}(f_{n'\mathbf{k}+\mathbf{q}} - f_{n\mathbf{k}}) \frac{\langle \psi_{n'\mathbf{k}+\mathbf{q}} | e^{i(\mathbf{q}+\mathbf{G})\mathbf{r}} | \psi_{n\mathbf{k}} \rangle \langle \psi_{n\mathbf{k}} | e^{-i(\mathbf{q}+\mathbf{G}')\mathbf{r}'} | \psi_{n'\mathbf{k}+\mathbf{q}} \rangle}{\epsilon_{n'\mathbf{k}+\mathbf{q}} - \epsilon_{n\mathbf{k}} - i\omega}, \end{aligned} \quad (6.32)$$

where $\psi_{n\mathbf{k}}$ and $\epsilon_{n\mathbf{k}}$ are the KS orbitals and energies and Ω is the volume of the Brillouin zone. The summation is performed over all occupied and unoccupied orbitals n and n' , $f_{n\mathbf{k}}$ denotes the occupation number, which is one for occupied and zero for unoccupied orbitals. The value of reciprocal lattice vector G_{max} in equation (6.26) is defined via

$$\frac{(\mathbf{G} + \mathbf{q})^2}{2} < E_{\text{cut}}^{\chi} = \frac{G_{\text{max}}^2}{2}, \quad (6.33)$$

where E_{cut}^{χ} is set to the value of ENCUTGW provided in the INCAR file. Convergence of the RPA correlation energy with respect to E_{cut}^{χ} is very slow and can hardly be achieved. Harl and Kresse [32] found that energy differences of RPA correlation energies and, in the case of the frozen core approximation, also total RPA correlation energies depend on E_{cut}^{χ} as

$$E_c^{\text{RPA}}(E_{\text{cut}}^{\chi}) = E_c^{\text{RPA}}(\infty) + \frac{A}{(E_{\text{cut}}^{\chi})^{\frac{3}{2}}}, \quad (6.34)$$

A being a constant. As shown in [29], this extrapolation is necessary but remarkably accurate and allows to obtain meV convergence for relative energies and 0.1% precision for lattice constants at moderate settings. In VASP, the basis set limit extrapolated $E_c^{\text{RPA}}(\infty)$ is determined via a linear regression of eight values of E^{χ} in steps of 5% of the provided energy cutoff E_{cut}^{χ} . To obtain smooth curves for the RPA correlation energy as a function of E_{cut}^{χ} , VASP applies a Hann like window function ($0.5(1 + \cos(x))$), which sets in at 80% of E_{cut}^{χ} and smoothly cuts off the contributions to the correlation energy for large G values.

6.3.3 Total RPA Energies

The Hartree-Fock energy expression evaluated with Kohn-Sham orbitals⁵ yields $E_{\text{EXX}} = T_{\text{KS}} + E_{\text{ext}} + E_{\text{H}} + E_{\text{x}}$, where we denote this energy as exact exchange (EXX) energy. The RPA total energy is thus given by $E_{\text{tot}}^{\text{RPA}} = T_{\text{KS}} + E_{\text{ext}} + E_{\text{H}} + E_{\text{x}} + E_{\text{c}}^{\text{RPA}} = E_{\text{EXX}} + E_{\text{c}}^{\text{RPA}}$. The RPA correlation energy is calculated via equation (6.26). In VASP, three steps are thus required for the calculation of the RPA total energy

- Exact exchange energy E_{EXX} : The Hartree-Fock energy expression is evaluated with KS orbitals. In all RPA calculations which are presented in the following, the GGA parametrization of Perdew-Burke-Ernzerhof (PBE) is applied to calculate the KS orbitals. For details related to the implementation of the exact exchange energy routines see [33, 34].
- Unoccupied orbitals: These are required to set up the response function (see equation (6.32)) and are yielded by an exact diagonalization of the Hamiltonian $H_{\mathbf{G},\mathbf{G}'}$ with rank G_{max} . The G_{max} , in this case, is the cut off in equation (6.10).
- RPA correlation energy: The response function is set up according to equation (6.32) with the previous calculated occupied and unoccupied orbitals as input. The RPA correlation energy is evaluated via equation (6.26) and its value for the basis set limit is extrapolated according to equation (6.34).

⁵We use PBE orbitals as input. The difference between EXX and RPA lattice constants obtained from LDA and PBE orbitals and the difference in the energetics is smaller than 0.1%

Part II

Results

Chapter 7

Phonon Zero-Point Vibration Energies

Experimental lattice constants, bulk moduli, atomization energies and heats of formation are affected by contributions from phonon zero-point vibration energies, which are in general not accounted for in zero temperature DFT calculations. Zero-point vibration energies influence not only the absolute energy but also the equation of state (energy versus volume curve), because the phonon frequencies decrease with increasing volume. This zero-point anharmonic expansion (ZPAE) has to be taken into account for an accurate comparison of theoretical and experimental values.

The increase of the theoretical lattice constants caused by the ZPAE can be as large as 2 % for very light solids such as LiH. The influence on Li is still 0.7 % and 0.5 – 0.9 % for LiF, LiCl, and NaCl. In view of new and very accurate methods like PBEsol[15], AM05[18, 35], revTPSS[36], the random phase approximation (RPA)[37, 29], or the second-order screened exchange corrected RPA[38], which all yield average lattice constant errors as small as 0.5 %, it is evident that the effect of the ZPAE must not be neglected. The ZPAE is often accounted for by semi-empirical formulas as derived in [39]. The ab-initio evaluation of zero-point energies via the phonon density of states is well es-

tablished. In the context of ab initio calculations, such corrections have been first calculated for BN[40] and MgO[41].

We present here the method and results for a concise set of zero-point vibration corrections from ab-initio as first published in [42]: To estimate the ZPAE, the PBE lattice constants of the materials presented in Tab. 7.2 are evaluated as the minimum of the internal energy $U(V)$ versus volume V curves

$$U(V) = E_0(V) + U_{\text{zero}}(V) \quad (7.1)$$

and as the minimum of the electronic contribution $E_0(V)$ only. The zero-point vibrational energy is calculated as a frequency integration over the vibrational density of states $g(V, \omega)$:

$$U_{\text{zero}}(V) = \frac{1}{2} \int \hbar\omega g(V, \omega) d\omega. \quad (7.2)$$

We use a direct approach employing the force constant method as outlined in [43] to calculate the phonon dispersion relation and vibrational density of states $g(V, \omega)$ from ab-initio. In this work, ab-initio calculations were performed using $2 \times 2 \times 2$ conventional unit cells and a plane-wave energy cutoff approximately 30 % above the default value. Convergence is reached at $4 \times 4 \times 4$ k-points for insulators and semi-conductors and at $8 \times 8 \times 8$ k-points for metals, with the exception of Li, which requires a $12 \times 12 \times 12$ k-point grid. All results presented in this chapter have been obtained using the projector augmented-wave method[26, 27] as implemented in the Vienna Ab-Initio Simulation Package (VASP) [22, 23]. The parameters of the PAW potentials used in this chapter are summarized in table 7.1.

Fig. 7.1 visualizes the effect of the zero-point vibrations for the case of C. The energy versus volume curve resulting from electronic contributions only as well as the zero-point corrected curve are shown. Beside shifting the energy-volume curve to smaller binding energies, the addition of the zero-point vibrational energies leads to an increase of the lattice constants resulting from the anharmonic potential. The effect of the specific functional (e.g. LDA versus PBE)

Table 7.1: Parameters of the PAW data sets used in this chapter. "Valence" indicates which orbitals are treated as valence orbitals; r_c^l are the cutoff radii for the partial waves. If small indices are used, they indicate which cutoff was used for s -, p -, and d -partial waves. E_{cut} are the energy cutoffs used in the present work.

	Valence	r_c^l (a.u.)	E_{cut} (eV)
H	1s	0.8	700
Be	1s2s	1.5 _s , 1.8 _{pd}	310
S	2s2p	1.5	400
Ge	3d4s4p	2.3 _{sp} , 2.2 _d	310
In	4d5s5p	2.5	240
Sn	4d5s5p	2.5	240
Sb	5s5p	2.3	170
Li	1s2s2p	1.7	500
B	2s2p	1.5 _s , 1.7 _p	320
C	2s2p	1.2 _s , 1.5 _p	400
N	2s2p	1.2 _s , 1.5 _p	400
O	2s2p	1.2 _s , 1.5 _{2p}	400
F	2s2p	1.2 _s , 1.5 _{2p}	400
Na	2p3s	2.2	260
Mg	3s3p	2.0	270
Al	3s3p	1.9	245
Si	3s3p	1.9	250
P	3s3p	1.9	270
Cl	3s3p	1.9	280
Cu	3d4s	2.3	295
Ga	3d4s4p	2.3	285
As	4s4p	2.1	210
Rh	4p4d5s5p	2.1 _p , 2.4 _{s,d}	250
Pd	4p4d5s5p	2.1 _p , 2.4 _{s,d}	255
Ag	4d5s	2.4 _{s,d}	250

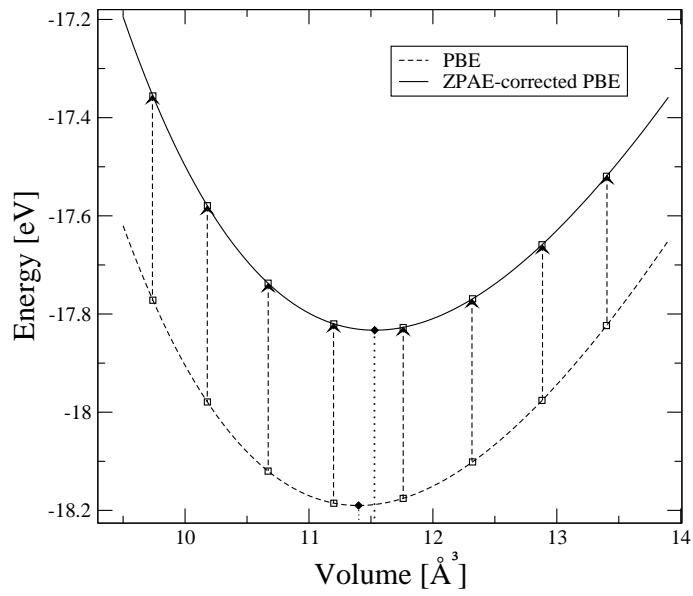


Figure 7.1: Energy versus volume for C-diamond including the zero-point vibrational energy (bold line) and neglecting zero-point vibrational effects (dashed line).

on the zero-point vibrational effect is found to be negligible. To show this, we evaluated the zero-point energies applying the LDA functional for some selected materials. For the vibrational frequencies, the deviations from PBE are typically only about 5%, and the resultant change of the ZPAE corrected lattice constants is typically only 0.05 % (5% of 1%). This suggests that it is irrelevant whether the ZPAE are calculated using the PBE functional or using a more accurate functional. Before commenting on the results in more detail, we would like to compare our results with existing literature data. Grabowski et al. have also calculated zero-point vibrational energies for few non magnetic fcc metals [44] using DFT within the quasi harmonic approximation. Their corrections for Al, Cu, Rh, Pd, Ag and Pt are essentially identical to our corrections. This is not astonishing, since similar codes and procedures were used, but it indicates that the authors of [44] and we have both reached technical convergence. The more interesting comparison is with the widely used semi empirical ZPAE corrections derived in [39]¹:

$$\frac{\Delta a_0}{a_0} = \frac{\Delta V_0}{3 V_0} = \frac{3}{16}(B_1 - 1) \frac{k_B \Theta_D}{B_0 V_0}. \quad (7.3)$$

In this equation, the lattice constants a_0 , the bulk moduli B_0 , and the Debye temperatures Θ_D are usually obtained from experiment, whereas the pressure derivative of the bulk modulus B_1 is usually calculated and thus depends on the applied functional. It is immediately obvious, that the semi empirical formula is remarkably accurate (see Tab.7.3), a posteriori validating its use. In particular for metals, our present values are practically identical to the simpler empirical correction. For semiconductors and insulators, however, the empirical ZPAE corrections are slightly too large, specifically for C, BN, LiF or MgO the empirical formula overestimates the ZPAE by about 30 %. This is most likely related to optical modes, which can not be properly described in the simple Debye model underlying Eq.(7.3). In Tab. 7.2 corrected and uncorrected PBE lattice constants are summarized for our test set of materials. As already

¹see Appendix C

mentioned above LDA ZPAE corrections would be almost identical to PBE ZPAE corrections. It seems therefore reasonable to correct the experimental lattice constants directly, and to compare with those corrected experimental lattice constants from now on, instead of applying the corrections to the theoretical energy-volume curves. Analog to lattice constants, we corrected also the experimental values for bulk moduli, atomization energies and heats of formation as presented in chapter 8.

Table 7.2: PBE lattice constants without (first column) and with (second column) zero-point vibrational energies. The change due to the resulting correction with respect to experiment is shown in column five. The experimental $T = 0$ K lattice constants in the third column have been taken from [45]. The fourth column shows the experimental lattice constants corrected for by the PBE ZPAE calculated from ab-initio phonon calculations. All lattice constants are given in Å. The Strukturbericht symbols (in parentheses) are used for the structure as follows: A1-fcc; A2-bcc; A4-diamond; B1-rocksalt; B3-zinc blende.

Solid	PBE	PBE+ZPAE corr	Exp.	Exp-ZPAE	% to Exp
Li(A2)	3.437	3.461	3.477	3.453	0.7
Na(A2)	4.197	4.208	4.225	4.214	0.3
Al(A1)	4.040	4.054	4.032	4.018	0.3
Rh(A1)	3.830	3.835	3.798	3.794	0.1
Pd(A1)	3.943	3.948	3.881	3.876	0.1
Cu(A1)	3.636	3.643	3.603	3.595	0.2
Ag(A1)	4.147	4.154	4.069	4.062	0.2
C(A4)	3.573	3.586	3.567	3.553	0.4
Si(A4)	5.469	5.478	5.430	5.421	0.2
Ge(A4)	5.761	5.769	5.652	5.644	0.1
Sn(A4)	6.656	6.664	6.482	6.474	0.1
LiH(B1)	4.006	4.090	4.064	3.979	2.1
LiF(B1)	4.064	4.102	4.010	3.972	0.9
LiCl(B1)	5.148	5.184	5.106	5.070	0.7
NaF(B1)	4.706	4.733	4.609	4.582	0.6
NaCl(B1)	5.699	5.724	5.595	5.569	0.5
MgO(B1)	4.260	4.278	4.207	4.189	0.4
SiC(B3)	4.379	4.391	4.358	4.346	0.3
BN(B3)	3.626	3.641	3.607	3.592	0.4
BP(B3)	4.547	4.560	4.538	4.525	0.3
BAs(B3)	4.808	4.830	4.777	4.755	0.5
GaN(B3)	4.546	4.557	4.520	4.509	0.2
GaP(B3)	5.506	5.515	5.448	5.439	0.2
GaAs(B3)	5.752	5.760	5.648	5.640	0.1
AlN(B3)	4.402	4.414	4.380	4.368	0.3
AlP(B3)	5.506	5.516	5.460	5.451	0.2
AlAs(B3)	5.735	5.743	5.658	5.649	0.2
InP(B3)	5.962	5.971	5.866	5.858	0.1
InAs(B3)	6.192	6.199	6.054	6.047	0.1
InSb(B3)	6.638	6.644	6.479	6.473	0.1

Table 7.3: Comparison of the semi-empirical and the ab-initio correction for lattice constants. The experimental $T = 0$ K lattice constants and the experimental lattice constants corrected for by the semi-empirical ZPAE given in Eq. (7.3) have been taken from [45] (first and second column).

Solid	Exp	Exp-ZPAE (empirical)	% to Exp.	Exp-ZPAE (present)	% to Exp
Li(A2)	3.477	3.451	0.7	3.453	0.7
Na(A2)	4.225	4.209	0.4	4.214	0.3
Al(A1)	4.032	4.019	0.3	4.018	0.3
Rh(A1)	3.798	3.793	0.1	3.794	0.1
Pd(A1)	3.881	3.876	0.1	3.876	0.1
Cu(A1)	3.603	3.596	0.2	3.595	0.2
Ag(A1)	4.069	4.062	0.2	4.062	0.2
C(A4)	3.567	3.544	0.6	3.553	0.4
Si(A4)	5.430	5.415	0.3	5.421	0.2
Ge(A4)	5.652	5.639	0.2	5.644	0.1
Sn(A4)	6.482	6.474	0.1	6.474	0.1
LiH(B1)	4.064			3.979	2.1
LiF(B1)	4.010	3.960	1.2	3.972	0.9
LiCl(B1)	5.106	5.072	0.7	5.070	0.7
NaF(B1)	4.609	4.576	0.7	4.582	0.6
NaCl(B1)	5.595	5.565	0.5	5.569	0.5
MgO(B1)	4.207	4.186	0.5	4.189	0.4
SiC(B3)	4.358	4.340	0.4	4.346	0.3
BN(B3)	3.607	3.585	0.6	3.592	0.4
BP(B3)	4.538	4.520	0.4	4.525	0.3
BAs(B3)	4.777	4.760	0.4	4.755	0.5
GaN(B3)	4.520	4.509	0.2	4.509	0.2
GaP(B3)	5.448	5.435	0.2	5.439	0.2
GaAs(B3)	5.648	5.637	0.2	5.640	0.1
AlN(B3)	4.380			4.368	0.3
AlP(B3)	5.460	5.445	0.3	5.451	0.2
AlAs(B3)	5.658	5.646	0.2	5.649	0.2
InP(B3)	5.866	5.856	0.2	5.858	0.1
InAs(B3)	6.054	6.044	0.2	6.047	0.1
InSb(B3)	6.479	6.471	0.1	6.473	0.1

Chapter 8

Assessing the RPA for Solids and Molecules

In this chapter, we present calculations applying three different functionals and compare their performance to RPA. Each of these four methods represents one rung in Perdew's 'Jacob's ladder' [46]. LDA is a pure local functional, PBE is a widely applied GGA (semi-local) functional (in particular in solid state physics), HSEsol involves a non-local potential, and finally RPA in the ACFDT framework includes unoccupied orbitals to calculate total energies. Results for lattice constants, bulk moduli and atomization energies for a test set of 24 solids of different bonding types (cohesive, ionic and metallic) are presented. Results of heats of formation for eight systems and molecular atomization energies for the G2-1 test set are shown as well.

8.1 Method of Calculation

All results presented in this chapter have been obtained using the projector augmented-wave method[26, 27] as implemented in the Vienna Ab-Initio Simulation Package (VASP) [22, 23].

The evaluation of the exact exchange energy in VASP as required for the

HSEsol functional has been discussed in [33, 34]. The parameters of the PAW potentials used in this chapter are summarized in table 7.1.

8.1.1 The HSEsol Functional

The HSEsol functional is a fairly recently published functional [42], accordingly we will present the fundamental idea and equations in the following. For solids, where the long-range part of the exact exchange is screened by correlation effects, faster numerical convergence of the hybrid functionals with k-points can be obtained by splitting the Coulomb interaction ν into a short-range (SR) and long-range (LR) part, e.g., by defining

$$\nu(r) = \frac{1}{r} = \underbrace{\frac{\text{Erf}(\mu r)}{r}}_{\nu^{\text{LR}}} + \underbrace{\frac{\text{Erfc}(\mu r)}{r}}_{\nu^{\text{SR}}}. \quad (8.1)$$

and by evaluating the long range part using DFT. In the screened hybrid functional introduced by Heyd, Scuseria, and Ernzerhof (HSE)[51], one quarter of the PBE short-range exchange is replaced by the exact exchange and the full PBE correlation energy is added. In the HSE06 functional (HSE06)[47] the range-separation parameter μ is set to $\mu = 0.207 \text{ \AA}^{-1}$, yielding a well balanced description for many properties. For the HSEsol functional, one quarter of the short-range PBEsol exchange is replaced by the exact exchange.

$$\begin{aligned} E_{\text{xc}}^{\text{HSEsol}} &= \\ &= E_{\text{c}}^{\text{PBEsol}} + E_{\text{x}}^{\text{PBEsol}} - \frac{1}{4} E_{\text{x}}^{\text{SR,PBEsol}} + \frac{1}{4} E_{\text{x}}^{\text{SR,EXX}}. \end{aligned} \quad (8.2)$$

The short-range PBEsol exchange can be calculated by multiplying the LDA exchange energy density with the enhancement factor $F_{\text{x}}^{\text{SR,PBEsol}}(s, \mu/k_{\text{F}})$, which depends on the dimensionless reduced gradient $s = |\nabla n|/(2k_{\text{F}}n)$ and the re-

duced range-separation parameter μ/k_F , $k_F = (3\pi^2n)^{1/3}$ (see e.g., [48]):

$$E_x^{\text{SR,PBEsol}} = \tag{8.3}$$

$$= \int d^3r n(\mathbf{r}) \epsilon_x^{\text{LDA}}[n(\mathbf{r})] F_x^{\text{SR,PBEsol}}(s(\mathbf{r}), \mu/k_F(\mathbf{r})). \tag{8.4}$$

The enhancement factor is determined by an integral of the range-separated Coulomb kernel $\nu^{\text{SR}} = \text{Erfc}(\mu u)/u$ times the spherically-averaged PBEsol exchange hole along $y = k_F u$:

$$F_x^{\text{SR,PBEsol},\mu}(s, \mu/k_F) = \tag{8.5}$$

$$= -\frac{8}{9} \int_0^\infty dy y J^{\text{PBEsol}}(s, y) \text{Erfc}((\mu/k_F) y).$$

For the PBEsol exchange hole, we use the form recently proposed by Henderson-Janesko-Scuseria (HJS)[49, 50] as formulated for the PBEsol functional. In contrast to the PBE[48] hole and the recently proposed PBEsol[53] exchange correlation hole by Perdew *et al.*, the HJS exchange hole allows a fully analytical evaluation of the range-separated enhancement factor. Additionally, it reproduces the PBEsol exchange energy within small error bars, if the bare Coulomb kernel is used.

The short-range exact exchange energy is obtained by replacing the Coulomb kernel in the exact exchange energy expression. The SR exact exchange is accordingly given as a double-sum over all occupied (occ) one-electron states $\psi_i(\mathbf{r})$:

$$E_x^{\text{SR,EXX}} = \tag{8.6}$$

$$= -\frac{1}{2} \sum_{ij, \text{occ}} \int d^3r d^3r' \nu^{\text{SR}}(|\mathbf{r} - \mathbf{r}'|) \times$$

$$\times \psi_i^*(\mathbf{r}) \psi_j(\mathbf{r}) \psi_j^*(\mathbf{r}') \psi_i(\mathbf{r}').$$

The convergence with respect to the k -point grid used in the Brillouin Zone sampling is the same as for the HSE06 functional and we therefore refer to

the detailed tests shown in [34]. Γ -centered Monkhorst-Pack like k -point grids were employed: $12 \times 12 \times 12$ k -points for insulators and $20 \times 20 \times 20$ k -points for metals. The reciprocal grid for the exact-exchange potential has been down sampled by a factor of two[54].

8.1.2 Settings for the RPA Calculations

The Calculation of the RPA correlation energy requires a large number of unoccupied states. To account for that, we use potentials constructed to describe the scattering properties of the atoms very accurately up to about 10 Ry above the vacuum level (for more details see Ref.[55]). Table 8.1 summarizes the parameters of the potentials applied in this chapter. We use PBE orbitals as input for the RPA correlation and the exact exchange energy (see section 6.3.3). More details about the cutoffs and k -point settings are tabulated in [29].

Table 8.1: PAW potentials applied for the LDA and RPA calculations. The states treated as valence are indicated in the second column. As local potential, a pseudopotential was generated for the states indicated in the column 'local'. For some elements the local potential was generated by replacing the all-electron potential by a soft potential within the cutoff radius r_{loc} (a.u.), which, in these cases, is provided in the 'local' column. The number of partial waves and projectors for different angular momentum numbers l is specified in columns four to seven. The energy E_{cut} refers to the standard energy cutoff of DFT calculations.

	valence	r_{loc}	s	p	d	f	$E_{\text{cut}}(\text{eV})$
Li	1s 2s	1.0	3	2			433
C	2s 2p	3d	2	2			414
N	2s 2p	3d	2	2			420
O	2s 2p	3d	2	2			414
F	2s 2p	4f	3	3	2		487
Na	2s 2p 3s	4f	3	3	2		260
Mg	2s 2p 3s	1.5	3	3	1		470
Al	3s 3p	4f	2	2	2		241
Si	2s 2p 3s 3p	4f	3	3	2		475
P	3s 3p	4f	2	2	2		255
Cl	3s 3p	4f	2	2	2		262
Cu	3d 4s	1.5	2	2	2		417
Ga	3s 3p 3d 4s 4p	4f	3	3	3		503
Ge	3d 4s 4p	4f	2	2	2		310
As	4s 4p	4f	2	2	1		209
Rh	4d 5s	1.6	2	2	2	2	247
Pd	4d 5s	1.6	2	2	2	2	251
Ag	4d 5s	1.4	2	2	2	2	250
In	4d 5s 5p	5f	2	2	3		279
Sb	4d 5s 5p	1.6	2	2	3	2	263

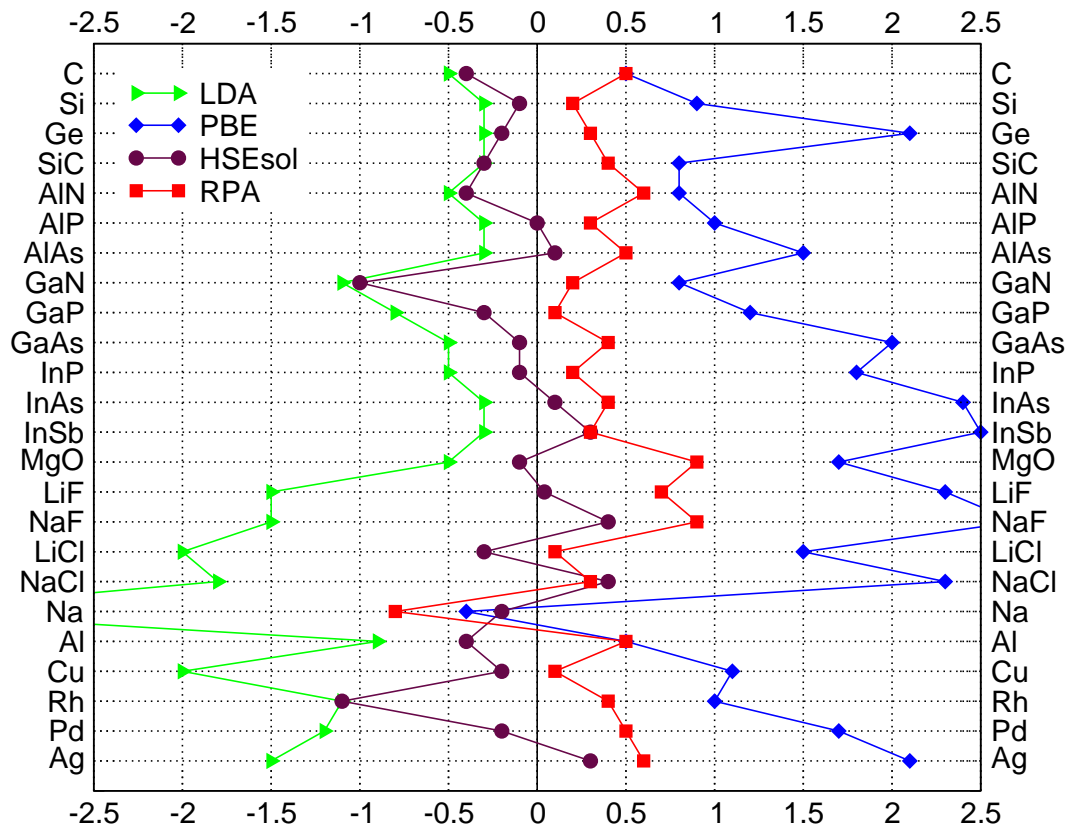


Figure 8.1: Lattice constant errors (%) compared to ZPAE corrected experimental lattice constants.

8.2 Results

8.2.1 Lattice Constants

Lattice constants obtained from RPA calculations are summarized in table 8.2 and are compared to LDA, PBE and HSEsol. The errors with respect to experimental lattice constants, which are corrected for the effect of zero-point vibrational energies are visualized in figure 8.1. The calculated lattice constants were obtained by a Birch-Murnaghan equation of state fitted to energies obtained for seven volumes centered around the experimental value.

Inspection of figure 8.1 reveals immediately that LDA yields in general too small, PBE too large and HSEsol and RPA very accurate lattice constants (MRE: LDA:−1.0%, PBE:1.6%, HSEsol:−0.2%, RPA: 0.4%). In the case of LDA, the overbinding is especially pronounced for metals, whereas PBE shows better than average agreement with experiment (MRE metal: LDA: −1.7 %, PBE: 1.0 %). Comparing the mean relative errors (MRE) of HSEsol and RPA for insulators and metals demonstrates that these two functionals are very well balanced; the performance hardly depends on the type of bonding (MRE insul/MRE metal: HSEsol: −0.1%/−0.3%, RPA: 0.4%/0.2%). A characteristic feature of DFT functionals is the increase of the error along a series of elements in one main group with increasing atomic number, e.g. C-Si-Ge. This is also true for alloys, e.g. GaN-GaP-GaAs, AlN-AlP-AlAs or InP-InAs-InSb. RPA is the only functional represented here which does not follow this trend. The mean absolute relative error (MARE) illustrates that LDA (MARE:1.0%) yields more accurate lattice constants than the GGA-functional PBE (MARE: 1.5%). HSEsol (MARE: 0.3%) and RPA (MARE: 0.4%) on the other hand clearly outperform LDA and PBE for lattice constants.

Table 8.2: Theoretical lattice constants (\AA) using the LDA, PBE, HSEsol and the RPA functional. The experimental lattice constants are corrected for zero-point vibrational energies (see table 7.2).

Solid	lattice constant (\AA)								
	LDA	%	PBE	%	HSEsol	%	RPA	%	Exp
C(A4)	3.534	-0.5	3.573	0.6	3.538	-0.4	3.572	0.5	3.553
Si(A4)	5.404	-0.3	5.469	0.9	5.415	-0.1	5.432	0.2	5.421
Ge(A4)	5.627	-0.3	5.761	2.1	5.633	-0.2	5.661	0.3	5.644
SiC(B3)	4.332	-0.3	4.379	0.8	4.334	-0.3	4.365	0.4	4.346
AlN(B3)	4.344	-0.5	4.402	0.8	4.351	-0.4	4.394	0.6	4.368
AlP(B3)	5.435	-0.3	5.506	1.0	5.45	0.0	5.467	0.3	5.451
AlAs(B3)	5.630	-0.3	5.735	1.5	5.656	0.1	5.675	0.5	5.649
GaN(B3)	4.460	-1.1	4.546	0.8	4.464	-1.0	4.519	0.2	4.509
GaP(B3)	5.396	-0.8	5.506	1.2	5.42	-0.3	5.442	0.1	5.439
GaAs(B3)	5.611	-0.5	5.752	2.0	5.635	-0.1	5.661	0.4	5.640
InP(B3)	5.827	-0.5	5.962	1.8	5.854	-0.1	5.867	0.2	5.858
InAs(B3)	6.029	-0.3	6.192	2.4	6.055	0.1	6.07	0.4	6.047
InSb(B3)	6.452	-0.3	6.638	2.5	6.493	0.3	6.494	0.3	6.473
MgO(B1)	4.169	-0.5	4.260	1.7	4.184	-0.1	4.225	0.9	4.189
LiF(B1)	3.913	-1.5	4.064	2.3	3.974	0.1	3.998	0.7	3.972
NaF(B1)	4.511	-1.5	4.706	2.7	4.599	0.4	4.625	0.9	4.582
LiCl(B1)	4.967	-2.0	5.148	1.5	5.052	-0.4	5.074	0.1	5.070
NaCl(B1)	5.469	-1.8	5.699	2.3	5.592	0.4	5.588	0.3	5.569
Na(A2)	4.056	-3.7	4.197	-0.4	4.206	-0.2	4.182	-0.8	4.214
Al(A1)	3.983	-0.9	4.040	0.5	4.003	-0.4	4.037	0.5	4.018
Cu(A1)	3.523	-2.0	3.636	1.1	3.587	-0.2	3.597	0.1	3.595
Rh(A1)	3.753	-1.1	3.830	0.9	3.753	-1.1	3.811	0.4	3.794
Pd(A1)	3.830	-1.2	3.943	1.7	3.869	-0.2	3.896	0.5	3.876
Ag(A1)	4.002	-1.5	4.147	2.1	4.073	0.3	4.087	0.6	4.062
MRE insul.		-0.8		1.6		-0.1		0.4	
MRE metals		-1.7		1.0		-0.3		0.2	
MRE all		-1.0		1.5		-0.2		0.4	
MARE insul.		0.8		1.6		0.3		0.4	
MARE metals		1.7		1.1		0.4		0.5	
MARE all		1.0		1.5		0.3		0.4	

8.2.2 Bulk Moduli

The presented bulk moduli were obtained by a Birch-Murnaghan equation of state fitted to energies evaluated by seven volumes centered around the experimental value. The comparison to corrected bulk moduli follows the results for the lattice constants: LDA overestimates bulk moduli (MRE: 6.0 %), especially for metals (MRE:17.2%), whereas PBE underestimates bulk moduli (MRE:−12.7%), especially for insulators (MRE:−14.2%). Overall, HSEsol and RPA perform significantly better than the pure DFT functionals LDA and PBE (MARE: LDA: 7.8%, PBE: 12.8 %, HSEsol: 3.6 %, RPA: 3.6 %).

Table 8.3: Bulk moduli in GPa using the LDA, PBE, HSEsol and the RPA functional. The last column summarizes the experimental bulk moduli (taken from [45] and references therein) for ZPE corrected and uncorrected (in parenthesis) values. Theoretical results are compared to the corrected values.

Solid	bulk moduli (GPa)								Exp
	LDA	%	PBE	%	HSEsol	%	RPA	%	
C(A4)	465	2.3	433	-4.7	480	5.7	441	-3.0	455(443)
Si(A4)	97	-3.8	88	-12.4	101	0.5	99	-1.8	101(99)
Ge(A4)	72	-6.8	59	-24.0	78	1.3	77	-0.4	77(76)
SiC(B3)	229	0.0	212	-7.7	237	3.6	223	-2.6	229(225)
AlN(B3)	211	2.4	193	-6.1	218	5.9	200	-2.9	206(202)
AlP(B3)	90	3.0	83	-5.6	94	7.0	92	5.2	87(86)
AlAs(B3)	75	-0.6	67	-11.2	79	4.3	77	2.1	75(74)
GaN(B3)	201	-5.9	170	-20.5	209	-2.0	189	-11.5	214(210)
GaP(B3)	90	0.5	76	-15.4	93	3.6	87	-2.9	90(89)
GaAs(B3)	74	-3.5	61	-21.1	77	0.9	77	0.4	77(76)
InP(B3)	71	-1.4	59	-18.0	74	2.9	71	-1.4	72(71)
InAs(B3)	60	2.4	48	-17.3	63	7.3	59	0.7	59(58)
InSb(B3)	46	-0.2	37	-20.4	47	2.7	44	-4.5	46(46)
MgO(B1)	172	1.3	149	-12.1	172	1.5	168	-1.0	170(165)
LiF(B1)	87	14.0	68	-11.4	77	1.1	76	-0.5	76(70)
NaF(B1)	61	15.0	45	-15.5	53	-0.7	53	-0.1	53(51)
LiCl(B1)	41	5.8	32	-18.0	36	-6.3	37	-4.5	39(35)
NaCl(B1)	32	16.1	24	-14.1	27	-3.2	29	5.2	28(27)
Na(A2)	9	17.1	8	1.4	8	0.0	8	4.1	8(8)
Al(A1)	84	2.4	76	-6.7	86	4.4	77	-6.1	82(79)
Cu(A1)	186	28.3	137	-5.3	146	0.9	153	5.5	145(142)
Rh(A1)	317	16.5	256	-5.9	318	16.8	258	-5.2	272(269)
Pd(A1)	226	14.1	167	-15.5	199	0.3	181	-8.6	198(195)
Ag(A1)	138	24.6	91	-17.5	106	-3.9	105	-5.2	111(109)
MRE insul.		2.2		-14.2		2.0		-2.8	
MRE metals		17.2		-8.3		3.1		-2.6	
MRE all		6.0		-12.7		2.3		-1.6	
MARE insul.		4.7		14.2		3.4		2.8	
MARE metals		17.2		8.7		4.4		5.8	
MARE all		7.8		12.8		3.6		3.6	

8.2.3 Atomization Energies of Solids

Atomization energies as defined in

$$E_{\text{Atm}}(\text{M}) = \frac{1}{N} \left\{ \sum_{\text{atoms}} E(\text{X}) - E(\text{M}) \right\} \quad (8.7)$$

of a material M with N atoms in a unit cell are reported in table 8.4 for a test set of 24 solids. $E(\text{M})$ is the total energy of the solid and $E(\text{X})$ denotes the corresponding energy of the constituent atoms. The values for LDA and RPA were published in [29], the atomization energies for HSEsol and PBE in [42]. Of the four compared functionals, PBE yields the most accurate results (MARE: 4.5 %). It slightly underestimates the atomization energies, independent of the bonding type (MRE metals: -4.5% , MRE insul.: -4.2%). The mean absolute relative error (MARE) of HSEsol is very similar (MARE: 4.2%). However, it yields too small values compared to experiment for metals (MRE metals: -5.2%) and overestimates the atomization energies for insulators (MRE insul.: 1.5%). This leads (by cancellation of errors) to an overall mean relative error of almost zero (MRE: -0.2%). RPA consistently underestimates atomization energies for this test set (MRE metals: -9.8% , MRE insul.: -6.4% , MRE all: -7.3%). As expected, LDA yields too large atomization energies for all solids (MRE insul.: 16% , MRE metals: 23.9% , MRE all: 18.0%).

For the RPA atomization energies, it is important to notice that the choice of the initial orbitals and one electron energies does influence the atomization energies for solids (contrary to the results for lattice constants and bulk moduli). This fact originates from the determination of the ground state energy of atoms. PBE favors a non spherical, symmetry broken solution for most atoms, whereas LDA often favors a spherical solution. As a result, in PBE, all orbitals are either fully occupied or unoccupied, whereas in LDA fractional occupancies are often found for atoms. Accordingly, the ground state energies of atoms differ significantly for LDA and PBE. As a pragmatic choice, all results presented here are calculated with PBE orbitals as input. For more details see

[29] section B..

Table 8.4: Atomization energies in kJ/mol/atom using the LDA, PBE, HSEsol and RPA functional. The last column summarizes the experimental atomization energies for ZPE corrected and uncorrected (in parenthesis) values. Experimental atomization energies for InP, InAs and InSb are taken from [57], for Ge and from [58]; all other experimental atomization energies are from [56].

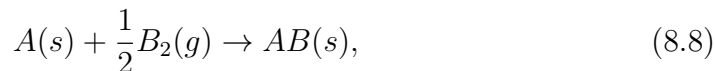
atomization energies (kJ/mol/atom)									
Solid	LDA	%	PBE	%	HSEsol	%	RPA	%	Exp
C(A4)	869	19.3	744	2.1	775	6.4	675	-7.3	728(711)
Si(A4)	515	14.1	440	-2.6	467	3.4	424	-6.2	452(446)
Ge(A4)	446	17.9	360	-4.8	390	3.1	346	-8.4	378(374)
SiC(B3)	719	15.0	618	-1.2	650	3.9	583	-6.8	625(612)
AlN(B3)	645	14.2	551	-2.5	570	1.0	527	-6.7	564(556)
AlP(B3)	470	12.7	395	-5.4	421	1.0	393	-5.8	417(411)
AlAs(B3)	436	18.3	356	-3.4	382	3.8	354	-3.9	369(365)
GaN(B3)	527	20.0	424	-3.5	450	2.4	408	-7.0	439(432)
GaP(B3)	424	21.6	337	-3.3	368	5.5	336	-3.6	348(343)
GaAs(B3)	395	22.5	304	-5.7	334	3.6	303	-6.0	322(319)
InP(B3)	400	19.6	304	-9.2	332	-0.9	301	-10.1	335(331)
InAs(B3)	367	23.4	279	-6.2	307	3.2	275	-7.5	297(294)
InSb(B3)	338	24.6	255	-6.0	280	3.2	250	-7.8	271(269)
MgO(B1)	567	13.1	481	-4.1	498	-0.7	474	-5.6	502(497)
LiF(B1)	477	10.8	418	-2.9	421	-2.2	405	-5.8	430(425)
NaF(B1)	423	10.3	369	-3.8	370	-3.5	364	-5.0	383(379)
LiCl(B1)	370	6.7	324	-6.4	338	-2.5	324	-6.4	346(343)
NaCl(B1)	338	4.8	298	-7.5	309	-4.2	304	-5.7	322(319)
Na(A2)	122	12.5	104	-3.6	105	-2.7	96	-10.7	108(107)
Al(A1)	390	17.8	331	0.0	354	7.0	311	-6.1	331(327)
Cu(A1)	439	29.3	336	-1.1	334	-1.7	324	-4.5	340(337)
Rh(A1)	740	32.7	552	-1.0	475	-14.9	487	-12.6	558(555)
Pd(A1)	490	28.9	358	-5.8	334	-12.2	329	-13.5	380(377)
Ag(A1)	351	22.1	243	-15.4	268	-6.7	255	-11.4	288(286)
MRE insul.		16.0		-4.2		1.5		-6.4	
MRE metals		23.9		-4.5		-5.2		-9.8	
MRE all		18.0		-4.3		-0.2		-7.3	
MARE insul.		16.0		4.5		3.0		6.4	
MARE metals		23.9		4.5		7.5		9.8	
MARE all		18.0		4.5		4.2		7.3	

Table 8.5: Heats of formation at $T=0$ K in kJ/mol (per formula unit; with respect to the elemental phases in their normal state under ambient conditions). Experimental values are collected in Ref. [56] and have been corrected for zero-point vibration energies.

Solid	heats of formation (kJ/mol)								
	LDA	%	PBE	%	HSEsol	%	RPA	%	Exp
LiF	613	-1.0	569	-8.1	599	-3.2	609	-1.6	619(614)
NaF	558	-3.3	522	-9.5	546	-5.4	567	-1.7	577(573)
NaCl	381	-7.7	355	-14.0	374	-9.4	405	-1.9	413(411)
SiC	54	-21.7	52	-24.6	60	-13.0	64	-7.2	69(72)
AlN	327	1.9	260	-19.0	303	-5.6	291	-9.3	321(313)
MgH2	89	14.1	52	-33.3	72	-7.7	72	-7.7	78(68)
MgO	595	-1.5	517	-14.4	558	-7.6	577	-4.5	604(597)
MRE all		-2.8		-17.6		-7.4		-4.9	
MARE all		7.3		17.6		7.4		4.9	

8.2.4 Heats of Formation

The heats of formation presented in table 8.5 are calculated according to the following definition: For the elementary reaction



the heats of formation are defined as

$$E_f[AB(s)] = -(E[AB(s)] - (E[A(s)] + \frac{1}{2}E[B_2(g)])), \quad (8.9)$$

where s and g refer to a compound in the solid or gas phase.

Although PBE performs well for the atomization energies of solids, heats of formation for the presented eight compounds are fairly inaccurate (MARE: 17.6%). LDA and HSEsol on the other hand show reasonable results (MARE LDA: 7.3%, MARE HSEsol: 7.4%). RPA performs best with a MARE of 4.9%.

8.3 Discussion

As a starting point, we summarize the above shown results by writing down the four compared functionals in order of increasing mean absolute relative errors. An up/down arrow indicates whether the mean relative error is positive (too large values compared to experiment) or negative (too small error compared to experiment).

- lattice constants: HSEsol(\downarrow) < RPA(\uparrow) < LDA(\downarrow) < PBE(\uparrow)
- bulk moduli: RPA(\downarrow), HSEsol(\uparrow) < LDA(\uparrow) < PBE(\downarrow)
- atomization energies of solids: HSEsol(\downarrow) < PBE(\downarrow) < RPA(\downarrow) < LDA(\uparrow)
- heats of formation: RPA(\downarrow) < LDA(\downarrow) < HSEsol(\downarrow) < PBE(\downarrow)

Having the computational demand for these methods in mind,

RPA \gg HSEsol \gg PBE $>$ LDA,

it is obvious that the additional investment in terms of computational cost is not reflected by this ranking in every single case.

The good performance of PBE and HSEsol for atomization energies of solids is remarkable, since heats of formation are, especially for PBE, very inaccurate. One common explanation for this error is the overestimation of the binding energy of dimers (O_2, N_2, F_2 , etc.) but this does not explain the error for MgH_2 or SiC. Hence, it seems that the fairly accurate results of PBE for atomization energies of solids is largely fortitious, maybe related to an error cancellation between solids and atoms.

To reinforce this idea, we also calculated atomization energies of 55 molecules (the G2-1 test set [60, 61]). The MAEs are 151 kJ/mol for LDA[62], 45.1 kJ/mol for RPA[59], 36 kJ/mol for PBE and 32 kJ/mol for HSEsol [42] (details of the 55 molecules are listed in Appendix D).

Hence, the performance of the four tested functionals is very similar to the one for atomization energies of solids. To get an alternative point of view regarding the quality of the data for molecular energies, but now disregarding the

atomic energies, we fitted the atomic energies in order to minimize the mean absolute error (MAE) of the G2-1 test set applying a Nelder-Mead Simplex algorithm. We found an MAE of 16.9 kJ/mol for LDA, 10.8 kJ/mol for HSEsol and PBE and 8.3 kJ/mol for RPA. We could of course proceed in the same way for atomization energies of solids but as of yet the solids set is simply too small (respectively the number of unknown atomic energies is too large).

Comparing the MAE of the G2-1 set with the MAE of the fitted atomic energies, we conclude that the good performance of PBE for atomization energies of solids stems in fact from a compatible description of the atoms (and thus from a cancellation of errors). However, the physical more relevant heats of formation and reaction energies are more accurately described by RPA.

Even the performance of RPA for atomization energies of solids (MARE:7.3%) is remarkably good if we keep in mind that total correlation energies in the random phase approximation are known to differ by more than 30% from the exact correlation energy[63].

The small mean absolute errors for lattice constants (MARE: 0.4%) and bulk moduli (MARE:3.6%) suggest on the other hand that the volume dependence of the total (correlation) energy is very well reproduced by RPA.

8.4 Conclusions

HSEsol is a hybrid functional based on PBEsol designed to improve the description of solids. The ideal hybrid functional for solids should yield very accurate lattice constants and bulk moduli as well as atomization energies for solids. The HSEsol functional provides all that: the mean absolute relative error of lattice constants compared to experiment is only 0.28% and also bulk moduli are very accurately described (MARE: 3.6%). For metallic systems, the HSE06 error for atomization energies of solids is almost halved, the performance for insulators and semiconductors is also slightly improved. In addition, band gaps are of comparable quality as for the HSE06 functional [42].

Concerning RPA, the above presented values for lattice constants, bulk moduli, atomization energies and heats of formation show that it is a very balanced approximation which yields very accurate results for the energetics as well as for structure calculations for cohesive, metallic and ionic type of bondings. Furthermore, RPA also describes seamless van der Waals bonding, without any introduction of parameters[32]. These results are very encouraging for the further investigation of the performance of RPA and suggest to apply RPA to more complex and 'realistic' problems. Although RPA is computationally very demanding, we can apply it nowadays to extended systems of up to 100 atoms. Hence, the heart of this thesis is the discussion of two (at the DFT level) unsolved problems in solid state physics: The adsorption of water on graphene (see chapter 9) and the adsorption of a CO molecule on transition metal surfaces (see chapter 10).

Chapter 9

Carbon Water Interaction

In this chapter we follow closely reference [88].

9.1 Carbon Water Interaction: A Complex Problem Worthwhile a Closer Investigation

To understand phenomena such as lubrication, the function of carbon nanotubes in biological media, or heterogeneous ice nucleation it is very important to explore the interaction of water with surfaces. Maybe the simplest model system that captures essential ingredients of a surface is graphene. The interaction of water with graphene is also interesting from a fundamental point of view. However, at the molecular level, understanding is far from complete even for the most fundamental question of how strong is the bond between water molecules and any carbon surface. Recently it was shown that RPA describes cohesive properties and the asymptotics of the dispersion interaction in graphite very accurately compared to available experimental data [84]. This makes RPA an interesting candidate for further analysis of carbon surfaces and their interaction with e.g. water. As a first benchmark for the carbon water interaction we calculated the binding energy curve for the adsorption of water on benzene using the RPA. Fig. 9.1 compares our RPA results to DMC results

published in [85]. The adsorption energy agrees with the DMC results within 10meV.

Hence, we applied the RPA to investigate the more challenging problem of one isolated water monomer adsorbing on a sheet of graphene. How important a precise description of this bonding situation is, reflects the following examples. Empirical potential calculations with one choice of water carbon interaction predicts filled carbon nanotubes, whereas other calculations, with slightly smaller assumed attraction between water and the tube walls predict almost empty tubes [86]. Similar, other simulations show that only a small variation in the strength of the water carbon bond leads graphite surfaces to appear as hydrophobic, or hydrophilic [87]. An accurate description of the adsorption is thus highly desirable.

9.2 Computational Setup

The setup described here concerns all RPA calculations in this chapter. The settings for the other presented methods can be found in [88].

The energy cutoff was set at 400 eV, PAW potentials in the implementation of Kresse and Joubert as indicated in table 9.1 were applied.

The benzene molecule is calculated at the Γ point only. The oxygen atom of the water molecule is placed above the center of the benzene molecule with two hydrogen atoms of water pointing symmetrically toward two carbon atoms (see inset of Fig. 1(a) in [85]). For a supercell with a volume of 1950 \AA^3 the adsorption energy is converged within error bars of 5 meV and agree with the DMC results within 10 meV.

The graphene sheet is represented by a hexagonal 5×5 supercell. The Brillouin zone is initially sampled at the Γ point only. This is large enough to model adsorption of an isolated water monomer. To converge the results with

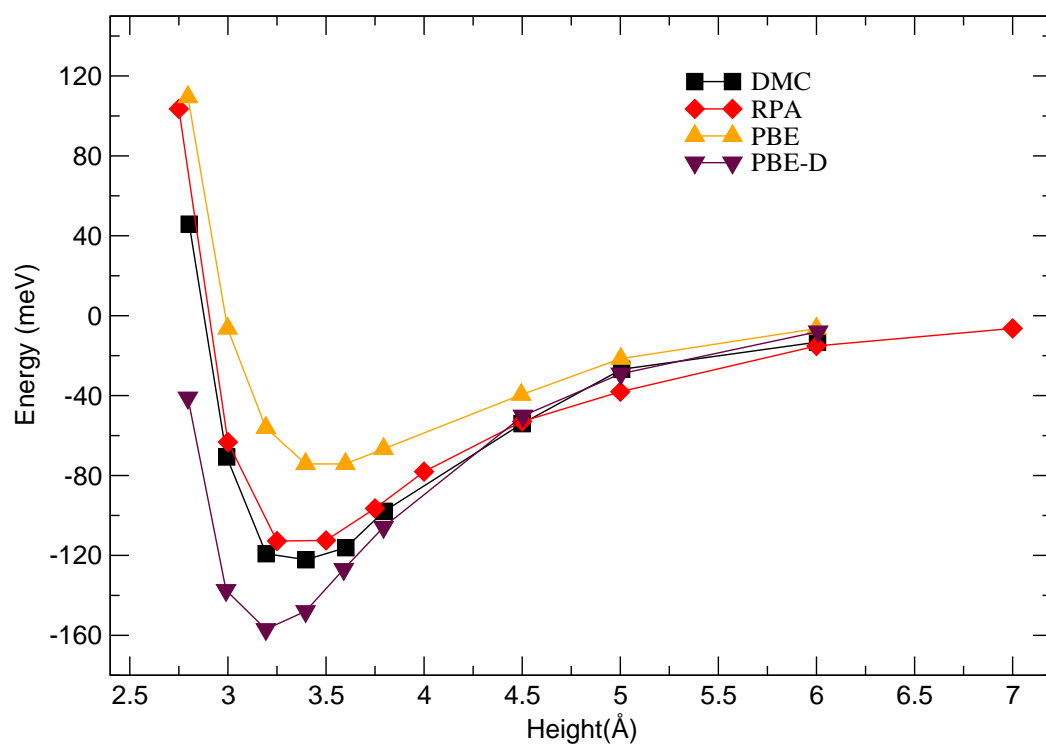


Figure 9.1: Adsorption energy of water on benzene versus O atom height obtained with DMC [85] and RPA.

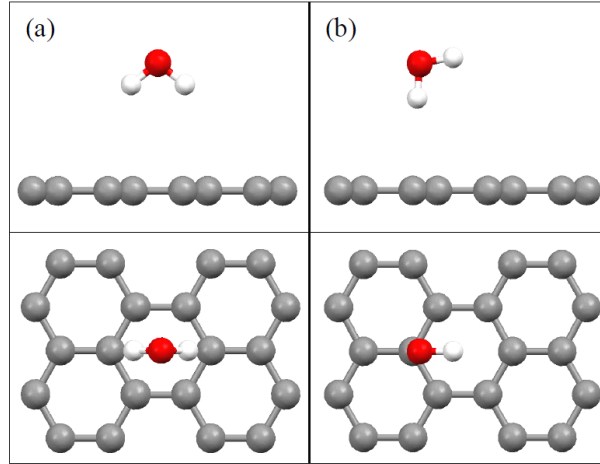


Figure 9.2: Water adsorption structures considered. (a) The two leg structure shown from the side (top) and from above (bottom). (b) The one leg structure shown from the side (top) and from above (bottom). For clarity only a small part of the periodic simulation cell is shown. The figure was originally published in [88].

Table 9.1: Applied PAW potentials. The states treated as valence are indicated in the second column. As local potential, a pseudopotential was generated for the states indicated in the column 'local'. For H the local potential was generated by replacing the all electron potential by a soft potential within the cutoff radius r_{loc} (a.u.), which in this case is provided in the 'local' column. The number of partial waves and projectors for different angular momentum numbers l is specified in columns four to seven. The energy E_{cut} refers to the standard energy cutoff for DFT calculations.

	valence	local	s	p	d	$E_{\text{cut}}(\text{eV})$
C	2s 2p	3d	2	2		414
H	1s	0.7	2	2		401
O	2s 2p	3d	2	2		414

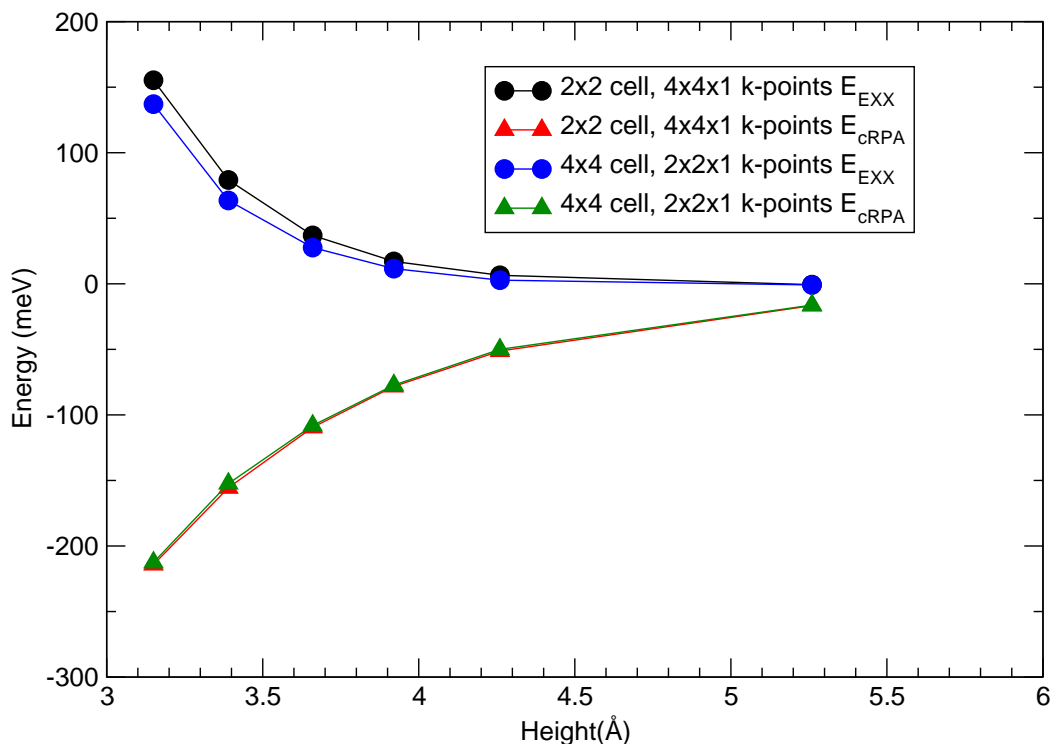


Figure 9.3: Comparison of the 2×2 cell and 4×4 cell with identical k-point sampling for the two leg structure.

respect to Brillouin zone sampling, additional calculations for a 4×4 cell using $2 \times 2 \times 1$ k-points and a 2×2 cell with up to $8 \times 8 \times 1$ k-points were performed. The changes of the correlation energy upon adsorption of water are identical to within 5 meV for the 4×4 and 2×2 cell, if identical k-point densities are applied. This indicates that correlation energy differences are fairly independent of coverage (see figure 9.3). This, however, does not apply to the exact exchange energy. Very accurate results were obtained by combining the correlation energies for a 2×2 cell using $8 \times 8 \times 1$ k-points with the exact exchange energy evaluated for a larger 8×8 cell and $2 \times 2 \times 1$ k-points. We refer to these results as converged energies as opposed to the Γ point only calculations.

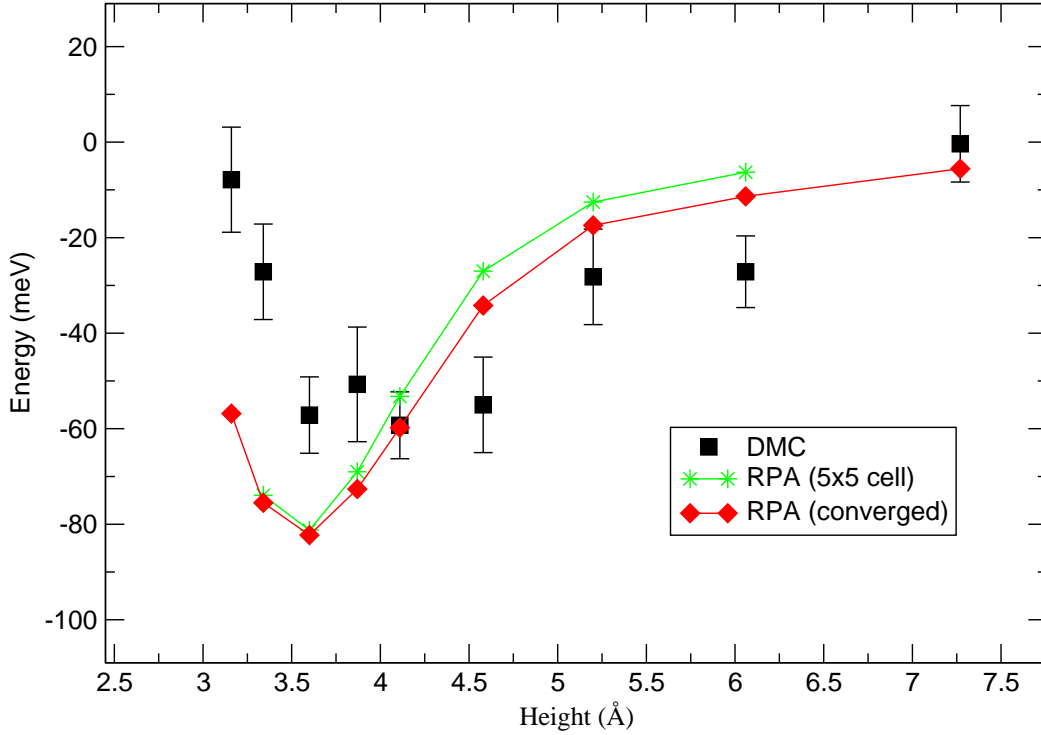


Figure 9.4: One-leg configuration: Adsorption energy versus O atom height for water on graphene obtained with DMC and RPA.

9.3 Results

Figures 9.4 and 9.5 show the binding energy curves for water on graphene obtained with diffusion Monte Carlo (DMC) and RPA. Results for two adsorption structures previously discussed in literature [89] are reported. For the one-leg structure, one of the OH bonds is directed towards the surface (see Fig. 9.2). For the second structure, referred to as two-leg structure, the water is located over the center of a hexagon ring with the two hydrogens equidistant from the carbon atoms. Table 9.2 summarizes the details of the adsorption structure and the adsorption energy E_{ads} at the minimum of each adsorption energy curve.

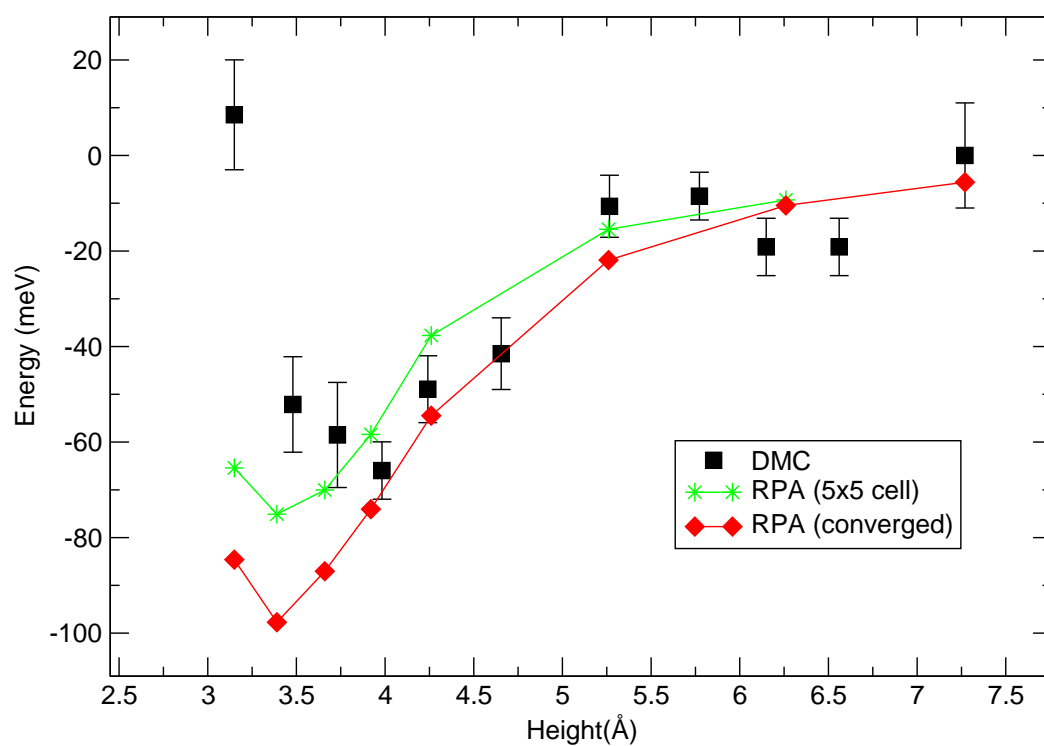


Figure 9.5: Two-leg configuration: Adsorption energy versus O atom height for water on graphene obtained with DMC and RPA.

The RPA calculations were initially performed in the 5×5 unit cell, yielding $E_{\text{ads}} = -81$ meV for the one-leg and $E_{\text{ads}} = -77$ meV for the two-leg structure. This results are in good agreement with DMC (see Figs. 9.4 and 9.5). The main difference from DMC is a slight shift towards smaller O-surface distances in the RPA and the absence of the shallow minimum at large distances. The converged RPA values differ from the Γ point only results with a string dependence on the orientation of the water molecule. For the two-leg structure, the Γ point only calculation in the 5×5 cell underestimates the binding energy by 20 meV, whereas for the one-leg configuration the results of the converged calculations are practically identical to the Γ point only calculation in the 5×5 cell. This result for the two-leg structure is also in good agreement with a recently published CCSD(T) study by Voloshina et al. [90].

Table 9.2: Adsorption energy E_{ads} and height (O-graphene surface distance in Å) for the one- and two-leg configuration. Due to the broad minimum in DMC, an error bar of ± 10 meV is given. RPA values in parenthesis are for the 5×5 unit cell, the others are the converged values with respect to k point sampling as described in section 9.2. Results other than for RPA are taken from [88].

Approach	Two leg		One leg	
	E_{ads} (meV)	Height (Å)	E_{ads} (meV)	Height (Å)
DMC	-70 ± 10	3.4-4.0	-60 ± 10	3.4-4.0
RPA	$-98(-77)$	3.42	$-82(-81)$	3.55
LDA	-151	3.04	-139	3.15
PBE	-27	3.65	-31	3.65
PBE-D	-90	3.35	-87	3.45

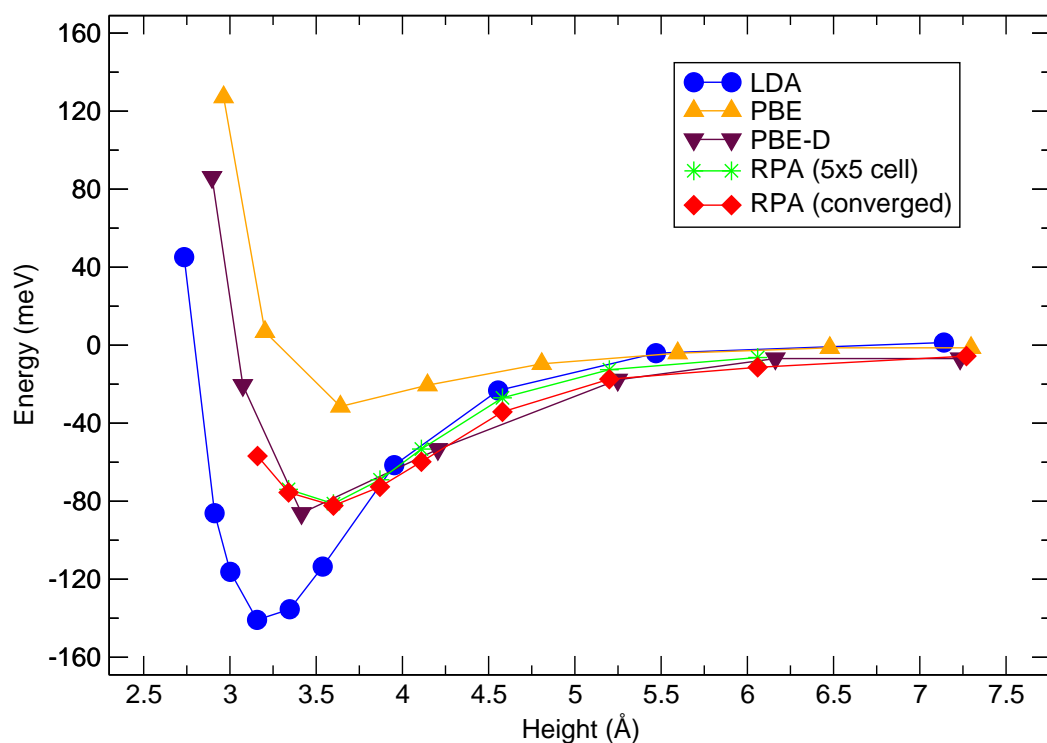


Figure 9.6: One-leg configuration: Adsorption energy versus O atom height for water on graphene obtained with various functionals. RPA and various DFT functionals are compared.

9.4 Discussion

The RPA correlation energy is sufficiently smooth to analyze its analytical behaviour. As expected for the interaction between an insulating/semiconducting sheet and a molecule, the correlation energy is proportional to $\frac{1}{(d-c)^4}$, where d is the distance between the O-atom and the graphene slab in Å and c is a constant which equals 0.47 and 0.28 for the one- and the two-leg configuration, respectively¹; the center of polarizability of the water molecule is obviously shifted towards the H atoms. Due to the large computational cost, analysis

¹see Appendix E.1

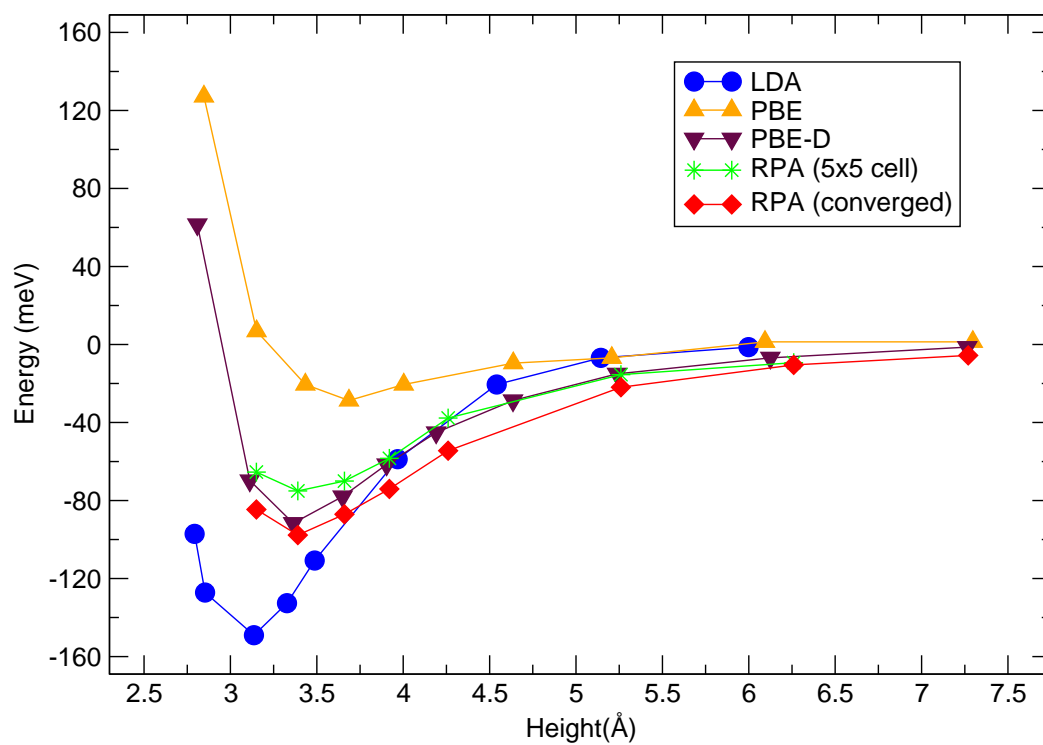


Figure 9.7: Two-leg configuration: Adsorption energy versus O atom height for water on graphene obtained with various functionals. RPA and various DFT functionals are compared.

at very large distances is at present not possible. However, at intermediate distances as considered here, a simple pairwise additive R^{-6} potential between the carbon atoms and the water molecule is compatible with the calculated $1/d^4$ behaviour. Hence, the use of a pairwise additive C_6R^{-6} correction, where R is the distance between atoms, should yield accurate results. Furthermore, the RPA calculations and the simple analytical behaviour up to a distance of 7 Å from the graphene slab suggest that the shallow DMC minimum at large distances is a sampling artefact rather than a physical feature.

With the converged RPA results as reference, it is interesting to assess the performance of selected DFT functionals, which is currently the method of choice for studies of the adsorption of water. It is clear from Figs. 9.6 and 9.7 that different DFT functionals yield very different results. PBE gives an adsorption energy of $E_{\text{ads}} = -31$ meV and the two configurations are almost degenerated (one-leg: $E_{\text{ads}} = -27$ meV, two-leg: $E_{\text{ads}} = -31$ meV). The adsorption minima are for both configurations at 3.65 Å, about 0.6 Å higher than the LDA value. LDA predicts a stronger binding than our reference values of $E_{\text{ads}} = -151$ meV and $E_{\text{ads}} = -139$ meV for the two-leg and the one-leg structure, respectively. In passing we note that BLYP predicts a repulsive interaction for both configurations and is thus not shown in the plots. None of the DFT functionals come even within 20 – 30% of the reference energy. Furthermore, they fail to predict the $1/d^4$ midrange behaviour.

Taken all this together, we conclude that the poor performance of the DFT functionals arises from their inadequacies in treating van der Waals forces. Considering the RPA binding curve with an almost perfect $1/d^4$ behaviour, DFT-D [91] seems to be a good choice for correcting for the deficiencies of DFT. The resulting E_{ads} , the binding distances and the energy binding curves are shown in Tab.9.2, Fig.9.6 and Fig.9.7.

For the adsorption of water on graphene, it is immediately obvious that this approach outperforms standard DFT functionals. The agreement with RPA is in fact excellent and even the slight preference for the two-leg structure is

reproduced. In particular, the equilibrium distances as well as the long-range behaviour are in reasonable agreement with RPA.

9.5 Conclusions

The RPA (and DMC) results presented here are the first explicitly correlated results for adsorption on a periodic graphene sheet. RPA predicts a value for the adsorption energy of $E_{\text{ads}} = -82$ meV and $E_{\text{ads}} = -98$ meV for the one- and the two-leg structure, respectively. These values are significantly below the range obtained from calculations for cluster models. The rather close agreement between DMC and RPA suggests that these values can serve as a benchmark for the development of other DFT functionals to treat water-carbon interfaces.

Chapter 10

Carbon Monoxide Adsorption on Transition Metal Surfaces

In this chapter we present details of our publication [64]: The adsorption of carbon monoxide on late transition metals is among the best studied surface science problems [65, 67, 66]. In 2001, Peter Feibelman and coworkers observed in their now classical paper that density functional theory is not able to predict the correct adsorption site for CO on Pt(111)[68]. Since then, many different variants of Kohn-Sham density functional theory have been applied to this prototypical problem, but until now parameter free (*ab-initio*) methods have not been able to resolve the discrepancy between theory and experiment [69, 70]. Furthermore, there is evidence of a general tendency of Kohn Sham density functionals to underestimate surface energies and overestimate chemisorption energies. This behaviour is counterintuitive, since a too small surface energy implies a too stable surface, which should result in too small adsorption energies. However, the contrary is found. To exemplify this problem we show in Fig. 10.1 the calculated surface energies and the calculated adsorption energies for CO on Pt(111) and Rh(111) for various functionals. One of these functionals is the PBE functional, which indeed predicts too small surface energies and too large adsorption energies. Semi-local functionals can

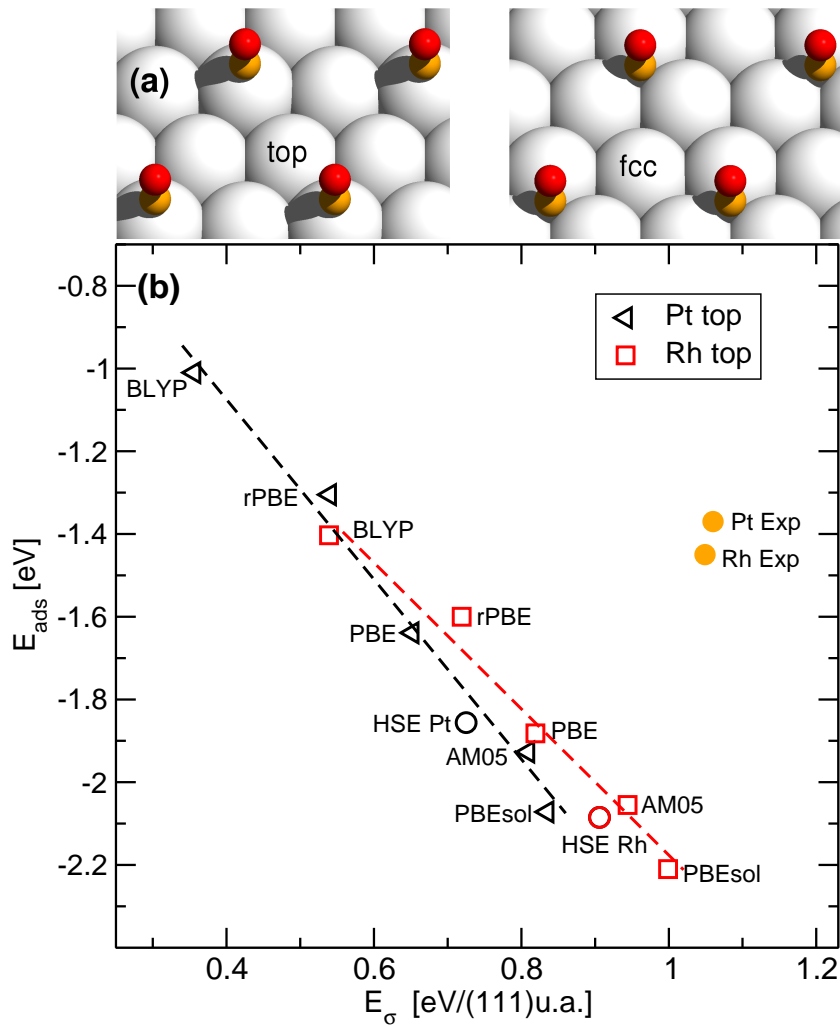


Figure 10.1: Atop CO adsorption and surface energies for Pt(111) and Rh(111). (a) Considered CO adsorption geometries for a (2×2) surface cell. Semi-local functionals predict CO to adsorb in the fcc hollow site coordinated to three metal atoms on Pt and Rh, whereas experiments unequivocally show adsorption atop a metal atom. (b) Atop adsorption energies versus surface energies for Pt(111) and Rh(111). Various semi-local functionals were used: AM05[18], PBEsol[15], PBE[14], rPBE[16] and BLYP[17], in order of increasing gradient corrections. Furthermore the hybrid functional HSE[71] based on the PBE functional was used. As expected, PBE yields in both cases a too small surface energy and a too large adsorption energy.

be modified by either enhancing or reducing the gradient correction. In one extreme, the local density functional approximation is recovered, which predicts reasonable surface energies but vastly overestimates adsorption energies, whereas a functional representative of the other extreme is the BLYP (Becke Lee Young Parr) functional. The important observation is that all semi-local functionals are lying roughly on a straight line: as expected, increasing the surface energy increases also the adsorption energy, and decreasing the surface energy decreases the adsorption energy. However, the theoretical line is clearly set off from the experimental values. Based on this observation, Stroppa et al. already concluded in Ref. [70] that semi-local functionals are not going to solve the CO adsorption problem. As a possible solution to the problem hybrid functionals that admix a fixed fraction of the non-local Hartree-Fock exchange were considered, and indeed they predict the correct adsorption site and adsorption energy for CO on Cu(111) [70], but for the open shell transition metals, specifically for Pt, the site adsorption problem was not solved, and worse, adsorption energies are even larger than with the equivalent semi-local functional without Hartree-Fock exchange (see Fig. 10.1) [70].

10.1 Computational Setup and Methods

The ab-initio calculations presented here were performed using PAW[26] potentials in the implementation of Kresse and Joubert[27]. See table 10.1 for specifics concerning the applied PAW potentials. Since trends are the main focus of this study, all metals were considered in the fcc (face centered cubic) structure, although Ru crystallizes in the hcp (hexagonal closed packed) structure. Adsorption at the atop and fcc hollow site was considered for Cu, Pd and Pt, whereas for Ru and Rh the top and hcp hollow sites were considered. The GW-RPA implementation is discussed in [72]. GW-RPA is compatible with RPA total energies insofar that both predict identical electron addition and removal energies.

Table 10.1: PAW potentials applied here. The states treated as valence are indicated in the second column. The third column indicates the cutoff radius for the local potential in (a.u.). The number of partial waves and projectors for different angular momentum numbers l is specified in columns four to seven. The energy E_{cut} refers to the standard energy cutoff for DFT calculations.

	valence	r_{loc}	s	p	d	f	$E_{\text{cut}}(\text{eV})$
Cu	3d 4s	1.5	2	2	2		417
Ru	4d 5s	1.8	2	2	2	2	269
Rh	4d 5s	1.6	2	2	2	2	247
Pd	4d 5s	1.6	2	2	2	2	251
Pt	4d 5s	1.6	2	2	2	2	249

10.1.1 Settings for the Calculation of Surface Energies

The presented surface energies are calculated as

$$E_{\sigma} = \frac{1}{2} \left(E_{\text{slab}} - \frac{N_{\text{slab}} E_{\text{bulk}}}{N_{\text{bulk}}} \right), \quad (10.1)$$

where E_{slab} and E_{bulk} are ground state energies per unit cell and N_{slab} , N_{bulk} are the number of atoms in the respective cell. The cutoff energy was set to 300 eV for all calculations. The Brillouin Zone was sampled by $16 \times 16 \times 1$ k-points for the evaluation of E_{slab} . For the E_{bulk} reference calculation an fcc supercell with three unit cells was applied. Table 10.2 summarizes further settings that were applied to obtain the surface energies.

10.1.2 Auxiliary Basis Set and k-point Extrapolation for Adsorption Energies

The adsorption energies presented in this chapter are defined as

$$E_{\text{ads}} = E_{\text{CO+slab}} - E_{\text{CO}} - E_{\text{slab}} \quad (10.2)$$

Table 10.2: Settings for the calculation of surface energies. Number of layers used to represent the clean metal slab are given in column one. Column two lists the applied k-point grids for the bulk reference calculation.

metal	nb. of layers	k-points
	E_{slab}	E_{bulk}
Cu	6	$16 \times 16 \times 6$
Ru	4	$16 \times 16 \times 8$
Rh	6	$16 \times 16 \times 6$
Pd	4	$16 \times 16 \times 8$
Pt	4	$16 \times 16 \times 6$

The molecule reference energy E_{CO} was calculated in a $11\text{\AA} \times 11\text{\AA} \times 13\text{\AA}$ super cell with the CO axis parallel to the z -axis. For the RPA adsorption energy calculations, the surfaces were modeled by a laterally periodic four layer metal slab with a $(\sqrt{3} \times \sqrt{3})$ periodicity for Pd and Rh and with a 2×2 periodicity for Cu, Rh and Pt. The cutoff energy (ENCUT) was set to 400 eV. The DFT and hybrid functional calculations were performed using (2×2) super cells and 6 layer slabs. For the 6 layer DFT calculations, the k-point grid was increased until meV convergence was obtained (up to $16 \times 16 \times 1$ k-points).

RPA is in terms of memory per core and in terms of computation time a fairly demanding method. Hence, despite the extrapolation to the infinite basis set limit as described in chapter 6, further extrapolations have been employed. The correlation part of the reported RPA energies $E_{\text{cRPA}}(\text{ENCUTGW}, \text{k-points})$ were calculated with a cutoff energy for the response function (see equation 6.33) of 100, 150 and 250 eV for identical k-point grids. For the 100 eV and the 150 eV runs we included only a quarter and half of the unoccupied bands,

respectively¹. Figure 10.2 shows that the correlation energy differences for calculations with 100 and 150 eV cutoff energy are for $3 \times 3 \times 1$ k-points converged within 20 meV (blue curve). Figure 10.2 presents data for Cu in a $(\sqrt{3} \times \sqrt{3})$ cell, but careful testing for the other presented metals suggests that this fast convergence of energy differences with respect to the k-point grid holds in general. For n larger than 3 we can now safely assume that

$$\begin{aligned} E_{\text{cRPA}}(150\text{eV}, 3 \times 3 \times 1) - E_{\text{cRPA}}(100\text{eV}, 3 \times 3 \times 1) &\approx \\ &\approx E_{\text{cRPA}}(150\text{eV}, n \times n \times 1) - E_{\text{cRPA}}(100\text{eV}, n \times n \times 1) \end{aligned} \quad (10.3)$$

As a consequence, the following extrapolation scheme is applied:

$$\begin{aligned} E_{\text{cRPA}}(150\text{eV ex}, 8 \times 8 \times 1) &= \\ &= E_{\text{cRPA}}(150\text{eV}, 3 \times 3 \times 1) - E_{\text{cRPA}}(100, 3 \times 3 \times 1) + E_{\text{cRPA}}(100, 8 \times 8 \times 1). \end{aligned} \quad (10.4)$$

$E_{\text{cRPA}}(100 \text{ eV}, n \times n \times 1)$ was calculated up to $n = 8$ and for selected cases up to $n = 10$. These values were further extrapolated using DFT: In Figure 10.2 we show that the total energy differences for RPA and DFT (here PBE) calculations with identical BZ sampling are for $8 \times 8 \times 1$ k-points converged to within 10 meV (red curve). Hence we may write

$$\begin{aligned} E_{\text{RPA}}(150\text{eV ex}, 8 \times 8 \times 1) - E_{\text{DFT}}(8 \times 8 \times 1) &\approx \\ &\approx E_{\text{RPA}}(150\text{eV ex}, 16 \times 16 \times 1) - E_{\text{DFT}}(16 \times 16 \times 1) \end{aligned} \quad (10.5)$$

from which follows

$$\begin{aligned} E_{\text{RPA}}(150\text{eV ex}, 16 \times 16 \times 1\text{ex}) &= \\ &= E_{\text{RPA}}(150\text{eV ex}, 8 \times 8 \times 1) - E_{\text{DFT}}(8 \times 8 \times 1) + E_{\text{DFT}}(16 \times 16 \times 1). \end{aligned} \quad (10.6)$$

¹N.B.: This is accurate for energy differences but not for total energies.

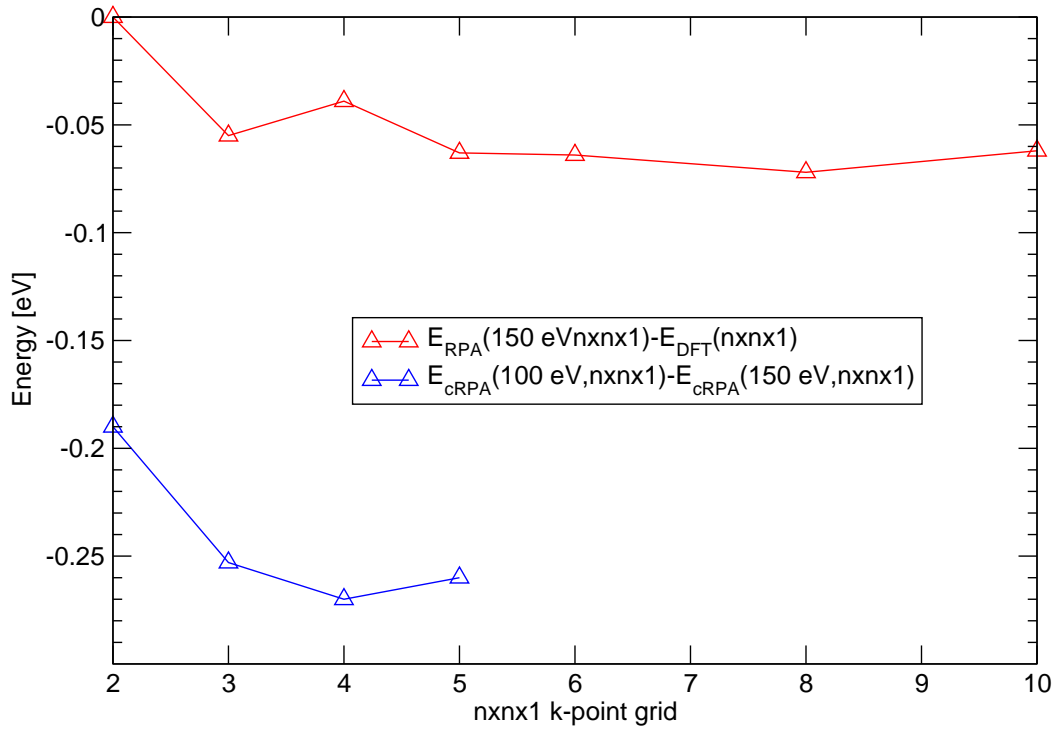


Figure 10.2: Convergence of energy differences for identical k-point sampling; here shown for CO adsorption on a $(\sqrt{3} \times \sqrt{3})$ periodically Cu surface of four layers. The first value in parenthesis of RPA (correlation) energies is the cutoff energy of the auxiliary basis set for the response function. To allow for a better comparison, the curves have been shifted.

Finally, we extrapolated from 150 eV to 250 eV again with the same reasoning as in equation (10.3):

$$\begin{aligned}
 E_{\text{cRPA}}(250 \text{ eV}, 16 \times 16 \times 1 \text{ ex}) &= \\
 &= E_{\text{cRPA}}(150 \text{ eV}, 16 \times 16 \times 1 \text{ ex}) - E_{\text{cRPA}}(150 \text{ eV}, 3 \times 3 \times 1) + \\
 &+ E_{\text{cRPA}}(250 \text{ eV}, 3 \times 3 \times 1).
 \end{aligned} \tag{10.7}$$

10.1.3 Applied Groundstate Geometries

The RPA calculations were performed at the PBE groundstate geometries. To evaluate this procedure, the CO bond length and distance from the surface were also optimized using RPA for Pt and Rh. For the top and hcp sites, the distance from the surface increases by about 0.03 Å from the PBE values, whereas the bond length remains almost identical to the PBE values. Due to the change in CO bond length and molecule-surface distance, the adsorption energies changed by at most 10 meV. Hence for the other metals, the PBE geometry was used. For reasons of consistency, all DFT calculations were performed at the PBE groundstate geometries, as well. In extreme cases (e.g. BLYP), the use of the respective relaxed structures would change the energy visibly on the scale of the plots. Nevertheless, this does in no way change the presented trends in adsorption and surface energies.

10.2 Results

10.2.1 Surface Energies

The surface energies for BLYP, PBEsol and RPA are summarized in table 10.3. RPA and PBEsol both show good agreement with experiment. As expected, BLYP underestimates the surface energy in general vastly with Ru being an exception. The experimental surface energies are deduced from liquid metal data [73] and are given in in J/m^2 . In table 10.4, the parameters to convert J/m^2 into $\text{eV}/\text{unit area}$ are given.

Table 10.3: Fcc(111) surface energies (E_σ) for PBEsol, BLYP and RPA in eV per unit area (u.a.). Experimental surface energies are deduced from liquid metal data [73].

	PBEsol	BLYP	RPA	Exp.
Cu	0.520	0.262	0.509	0.641
Ru	1.170	0.981	1.174	1.188
Rh	0.999	0.539	0.960	1.049
Pd	0.730	0.357	0.732	0.840
Pt	0.835	0.356	0.832	1.060

10.2.2 Adsorption Energies

The adsorption energies for CO at the metal top and hollow sites are summarized in Table 10.5 for Cu, the late $4d$ metals, and Pt. Excellent agreement with experiment is found for the RPA adsorption energies. Furthermore, RPA predicts the correct adsorption site in every single case, but we feel that the correct description of the adsorption energies is even more relevant. The three most critical cases are Cu, Pt and Rh, where most DFT functionals predict the

Table 10.4: Experimental surface energies in J/m^2 (column three) are deduced from liquid metal data [73]. The applied PBE-fcc lattice constants and the corresponding (111)-unit area (u.a.) are listed in column one and two in order to convert the experimental surface energies into $\text{eV}/(\text{u.a.})$ (column four).

	lattice constant [\AA]	$A_{u.a.}$ [$\text{eV}/\text{\AA}^2$]	Exp. [J/m^2]	Exp. [$\text{eV}/\text{u.a.}$]
Cu	3.64	5.737	1.790	0.641
Ru	3.80	6.253	3.043	1.188
Rh	3.82	6.319	2.659	1.049
Pd	3.94	6.722	2.003	0.840
Pt	3.97	6.825	2.489	1.060

Table 10.5: Adsorption energies for the hollow/atop sites of CO on Cu, late $4d$ metals and Pt for PBEsol, RPA and BLYP. Experimental data with error bars are from Ref. [74]. The preferred site is in bold font. All energies are given in eV. The fifth column indicates the experimentally preferred site.

	PBEsol	BLYP	RPA	Exp.	Exp.ads.site
Cu	-1.32 / -1.06	-0.23 / -0.23	-0.31 / -0.43	-0.5 ± 0.05	top
Ru	-2.43 / -2.18	-1.17 / -1.37	-1.27 / -1.48	-1.49 ± 0.22	top
Rh	-2.44 / -2.21	-1.24 / -1.40	-1.24 / -1.42	-1.45 ± 0.14	top
Pd	-2.54 / -1.81	-1.27 / -0.89	-1.40 / -1.07	-1.48 ± 0.09	hollow
Pt	-2.32 / -2.07	-1.02 / -1.01	-1.19 / -1.29	-1.37 ± 0.13	top

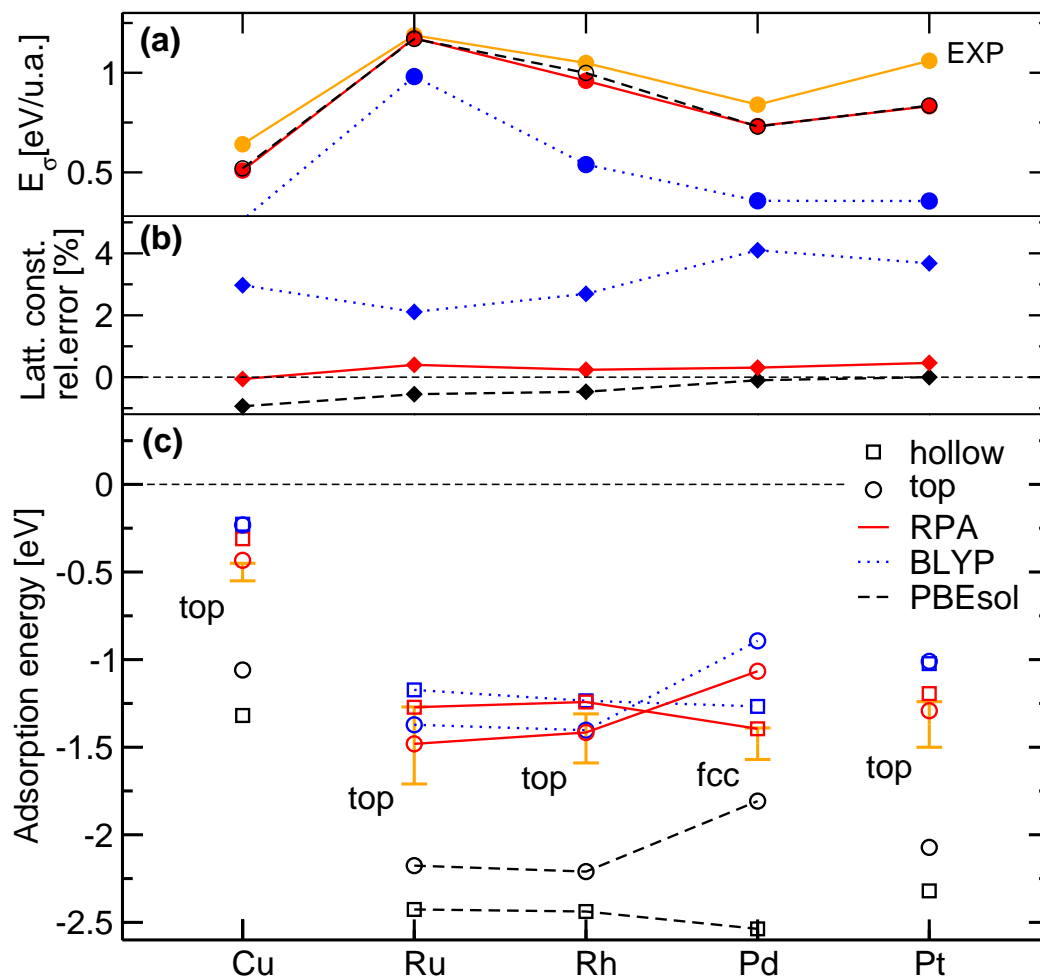


Figure 10.3: Surface energies, lattice constants and adsorption energies. (a) fcc(111) surface energies (E_σ) for PBEsol, BLYP and RPA. Experimental surface energies are deduced from liquid metal data Ref. [73]. (b) Lattice constants for PBEsol, RPA and BLYP. (c) Adsorption energies for the atop and hollow sites of CO on Cu, late 4d metals and Pt for PBEsol, RPA and BLYP. Experimental data with error bars are from Ref. [74].

wrong site order. The RPA restores the correct site order in all cases: -0.43 eV (Cu-top) < -0.31 (Cu-fcc), -1.29 eV (Pt-top) < -1.19 (Pt-fcc) and -1.42 eV (Rh-top) < -1.24 (Rh-hcp).

10.2.3 Summary

To reinforce our previous arguments, figure 10.3 summarizes results for lattice constants, surface energies and adsorption energies using the functionals that predict the largest (PBEsol) and smallest (BLYP) surface energy and compare them to RPA. The functional with weak gradient corrections, PBEsol, yields good lattice constants, and the functional with the largest gradient corrections, BLYP, predicts good adsorption energies. Clearly, however, the BLYP functional (good adsorption energies) predicts much too small surface energies and too large lattice constants, whereas the PBEsol functional (good lattice constants) fails dramatically for the adsorption energies, and only RPA reproduces both.

10.3 Discussion

The ACFDT-RPA approach for total energies leads to a quantitative and qualitative improvement over semi local KS functionals. Starting from PBE orbitals, RPA increases the surface energy, but decreases the adsorption energy yielding very good agreement with experiment (see Fig. 10.4). To gain insight into this behaviour we have evaluated the quasi-particle energies using a method that is compatible with RPA total energy calculations, the so called GW method in the RPA approximation (GW-RPA)[75]. This method allows direct comparison with experimental photo emission or inverse photo emission measurements. The electronic densities of states (DOS) for a semi-local DFT functional (PBE), for GW-RPA and for a hybrid functional (HSE) are shown in Fig. 10.5. The common model to describe CO adsorption is the Blyholder model[78, 79], which invokes interactions of the two CO frontier orbitals, the

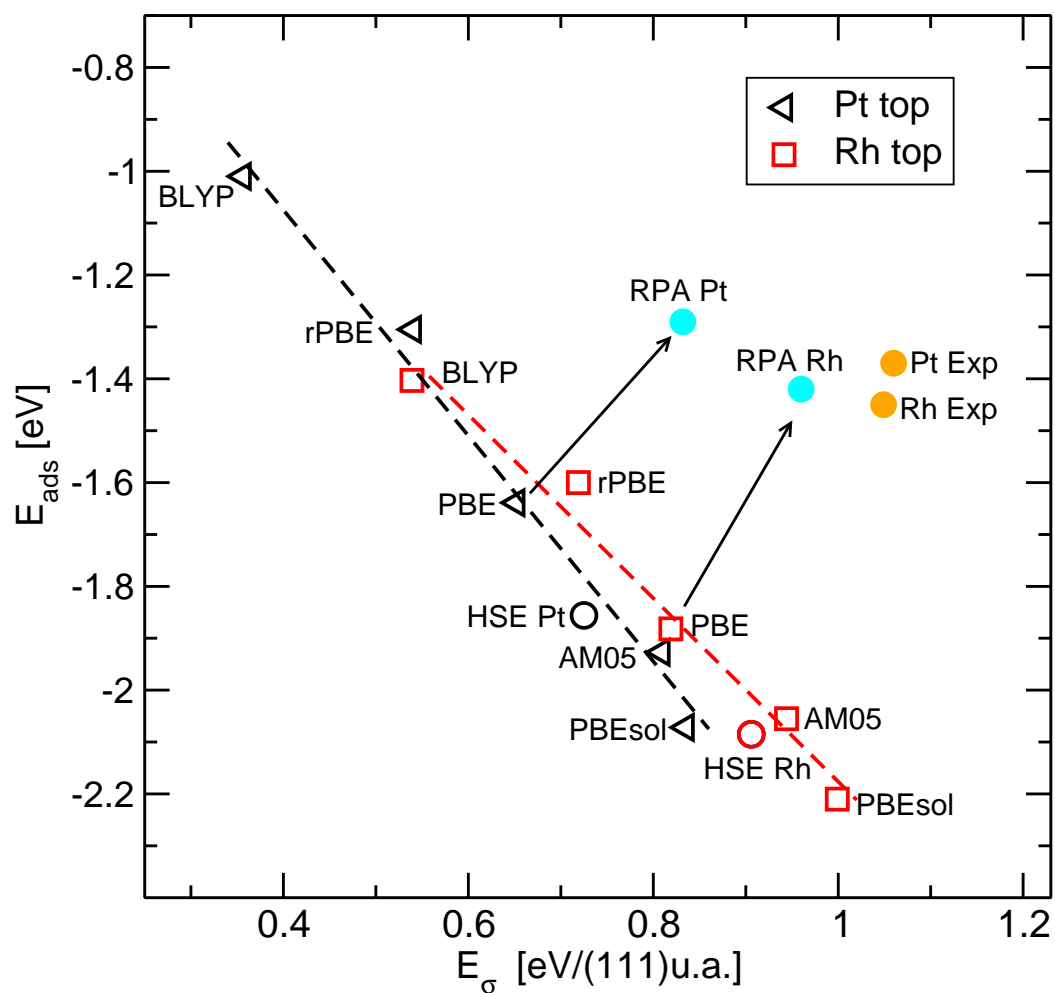


Figure 10.4: Atop CO adsorption and surface energies for Pt(111) and Rh(111). Starting from PBE orbitals, RPA increases the surface energy, but decreases the adsorption energy yielding very good agreement with experiment.

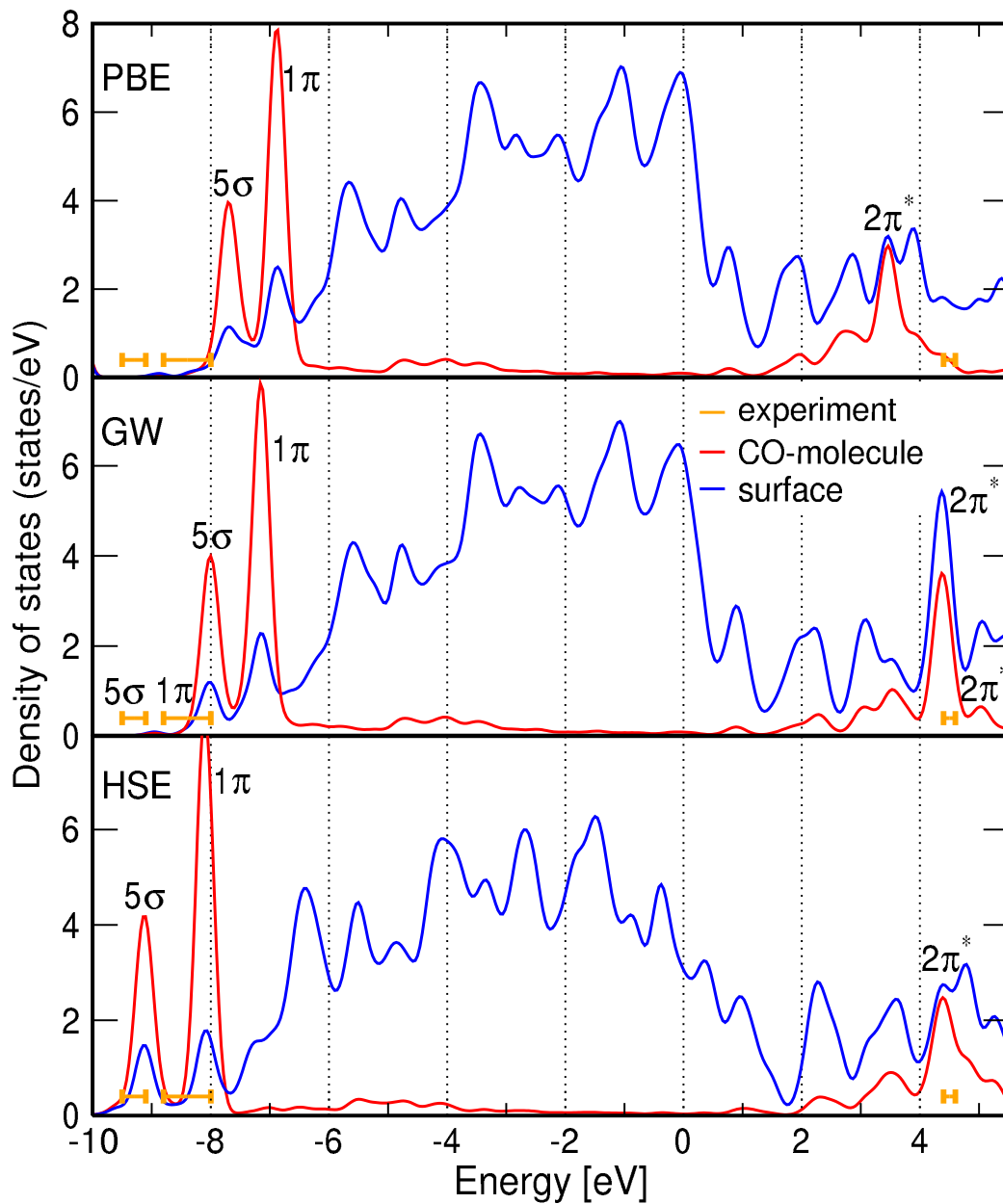


Figure 10.5: Electronic density of states (DOS) for CO adsorbed atop a Pt atom on Pt(111). The DOS is evaluated using density functional theory (PBE), the random phase approximation (GW-RPA) and a hybrid functional (HSE). Experimental photo emission data for the $2\pi^*$ state are from [76], for the 5σ and 1π state from [77].

5σ HOMO (highest occupied molecular orbital) and the $2\pi^*$ LUMO (lowest unoccupied molecular orbital), with the metal states. Because of the interaction with the metal states, bonding and anti-bonding 5σ -metal hybrid orbitals develop, and the latter are partly shifted above the Fermi-level of the metal, causing a net bonding interaction (donation to surface). Likewise, bonding $2\pi^*$ -metal hybrid states become populated (back-donation). From symmetry arguments it follows that the highly directional 5σ -metal interaction is particularly strong for atop adsorption, whereas the $2\pi^*$ interaction is more important for hollow site adsorption [66, 80, 83]. It is quite well established that semi-local functionals predict a very reasonable d band width for Pt. Indeed comparison of the DFT results with GW-RPA, and comparison of the bulk DOS with experimental spectra confirms this. However, PBE fails to predict the position of the CO frontier orbitals. Both the 5σ and, in particular, the $2\pi^*$ orbitals are located too close to the Fermi-level, which we believe to cause the observed overestimation of the adsorption energies [80]. Upon modification of the semi-local density functional, the DOS remains essentially unchanged, but the surface energies and adsorption energies increase or decrease observing a linear relationship. Since the molecular frontier orbitals are too close to the Fermi-level, the adsorption energy is too large, if the surface energy is correct. Good agreement with the experimental adsorption energies is only obtained by making surfaces artificially stable using, for instance, the BLYP functional. In this case, however, a better overall description is not obtained either, since BLYP underbinds the solids dramatically and yields e.g. much overestimated lattice constants (see Fig. 10.3b). The hybrid functional describes the position of the $2\pi^*$ and 5σ frontier orbitals best, but the band width of the transition metal is overestimated compared to experiment. Since this increases the surface energy and concomitantly the capability of the surface to form bonds with adsorbates, the beneficial effects of the hybrid functional on the description of the CO molecule are counteracted by the adverse effects on the description of the substrate. The GW-RPA method yields excellent results for the metal

band-width and the $2\pi^*$ frontier orbital, but somewhat underbinds the 5σ orbital, which is a known problem of the GW-RPA approximation and commonly observed for localized states (5σ and 1π in our case). Overall, the RPA seems to offer a very reasonable description of the electronic properties (DOS) of CO and the metal, which is also reflected in the improved energetics. We note that for metals with a closed d shell, .e.g. Cu, hybrid functionals [81] yield good agreement with experiment. In this case, even low-order many-body perturbation theory, such as second-order Møller-Plesset perturbation theory, applied to small clusters [81] yields results in good agreement with cluster-based RPA calculations [82]. However, open-shell transition metals are more difficult and pose a more stringent test for the accuracy of the RPA.

10.4 Conclusion

In summary, we suggest that the RPA is an excellent choice for predicting surface and adsorption energies. If surfaces reconstruct upon adsorption of molecules, a reliable prediction of both properties is absolutely required. Presently, this can be only achieved using the methods proposed here. Combined with the improved description of bulk materials (see chapter 8), the method seems to be an ideal supplement to density functional theory calculations and an important step towards the accurate and quantitative description of materials properties. It is readily applicable to more applied problems in heterogeneous catalysis or energy storage materials.

Chapter 11

Conclusions and Summary

This thesis was devoted to the assessment and application of the random phase approximation (RPA) in the adiabatic-connection fluctuation-dissipation (ACFD) framework.

The ACFD theorem provides an exact expression for the exchange-correlation energy as a function of the density-density response function of the respective system. The exact response function is unknown and hence approximated by the RPA. This formalism provides us with an approximative expression for the total energy that we evaluate using one-electron orbitals from a preceding calculation.

In the theory and methods part, a review of density functional theory (DFT) and the ACFD theorem in the RPA was presented. It includes an introduction to the many-body problem as well as a description of the implementation of RPA in the Vienna Ab-initio Simulation Package (VASP).

To assess the quality of the RPA, we compared its performance to three (beyond) DFT functionals: the local density approximation (LDA), the Perdew-Burke-Ernzerhof (PBE) functional and the hybrid functional HSEsol. We presented results for lattice constants, bulk moduli and atomization energies for

a test set of 24 solids of different bonding types (covalent, ionic and metallic). Results for heats of formations for eight systems and molecular atomization energies for the G2-1 test set were shown as well. The experimental values were corrected for the effect of phonon zero-point vibrational energies which had been calculated at DFT level from ab-initio.

We found that the RPA describes all bonding situations equally accurately. Furthermore, the RPA accounts seamlessly for van-der-Waals interactions and includes the description of long range dispersion forces while at the same time remaining accurate in the case of overlapping electron densities.

This makes the RPA a promising candidate for more complex problems in solid state physics and molecular as well as supra molecular chemistry.

To this end, we investigated the carbon-water interaction in two situations: the adsorption of water on benzene and the adsorption of water on a graphene layer. We compared our results to another correlated method: diffusion Monte Carlo (DMC). We found very good agreement and thus believe that these values can serve as a benchmark for the development of other DFT functionals to treat water-carbon interfaces.

The crucial section of this thesis was the successful application of the RPA to the long-standing and (at DFT level) unsolved *CO adsorption puzzle*. We saw results for CO adsorption on Cu, late 4d metals and Pt. RPA is at present the only ab-initio method that describes adsorption and surface energies accurately at the same time and predicts the correct adsorption site in every single case.

Despite this remarkable success, there is still room for improvement of the RPA:

At present, structural relaxation is not possible, since forces are not available in the current implementation. Although we could show, that relaxation is not necessary for the presented results, there are cases where structural relaxation is inevitable.

Furthermore, all RPA results presented in this thesis were obtained non-self-consistently, with DFT orbitals as input. To avoid this dependence on the input, Optimized Effective Potential methods yield a formalism which allows a self-consistent evaluation of the RPA. This approach is computationally rather demanding and no results have been published thus far. Another shortcoming of RPA is that it is not self-correlation free. It yields a finite correlation energy even for one-electron systems. A second order screened exchange (SOSEX) correction was recently proposed [38]. SOSEX is indeed self-correlation free and appears to improve upon RPA atomization energies. The scaling of RPA+SOSEX is the same as for conventional RPA, however, the prefactors are roughly two magnitudes larger. A largely complete review of RPA, its implementation in different codes, possible further corrections to approximate the correlation energy beyond RPA, as well as a summary of current results is presented in [93].

In summary, all presented results taken together lead us to the conclusion that RPA is an ideal supplement to density functional theory calculations and an important step towards the accurate and quantitative description of materials properties. It is applicable to systems of more than 100 atoms and thus to even more applied problems like heterogeneous catalysis or energy storage materials. In contrast to other methods, the RPA does not require fitting to experimental data and is truly parameter-free.

Appendix A

Adiabatic Connection Fluctuation-Dissipation Theorem

A.1 Proof of Equation (4.5)

$$\begin{aligned}\langle \Psi_1 | \hat{V}_{\text{ext}} | \Psi_1 \rangle &= \int d^3 r_1 \dots d^3 r_N \Psi_1^*(\mathbf{r}_1, \mathbf{r}_2, \dots, \mathbf{r}_N) \sum_i \hat{v}_{\text{ext}}(\mathbf{r}_i) \Psi_1(\mathbf{r}_1, \mathbf{r}_2, \dots, \mathbf{r}_N) \\ &= \int d^3 r \hat{v}_{\text{ext}}(\mathbf{r}) N \int d^3 r_2 \dots d^3 r_N \Psi_1^*(\mathbf{r}, \mathbf{r}_2, \dots, \mathbf{r}_N) \Psi_1(\mathbf{r}, \mathbf{r}_2, \dots, \mathbf{r}_N) \\ &= \int d^3 r n(\mathbf{r}) \hat{v}_{\text{ext}}(\mathbf{r}) = \int d^3 r \hat{v}_{\text{ext}}(\mathbf{r}) \sum_{i=1}^N \psi_i^*(\mathbf{r}) \psi_i(\mathbf{r}) = \\ &= \int d^3 r \hat{v}_{\text{ext}}(\mathbf{r}) \psi_1^*(\mathbf{r}) \psi_1(\mathbf{r}) + \dots + \int d^3 r \hat{v}_{\text{ext}}(\mathbf{r}) \psi_N^*(\mathbf{r}) \psi_N(\mathbf{r}) = \\ &= \int d^3 r_1 \hat{v}_{\text{ext}}(\mathbf{r}_1) \psi_1^*(\mathbf{r}_1) \psi_1(\mathbf{r}_1) + \dots + \int d^3 r \hat{v}_{\text{ext}}(\mathbf{r}_1) \psi_N^*(\mathbf{r}_1) \psi_N(\mathbf{r}_1) = \\ &= \int d^3 r_1 \dots d^3 r_N \sum_{i=1}^N \hat{v}_{\text{ext}}(\mathbf{r}_i) \Psi_0^*(\mathbf{r}_1, \mathbf{r}_2, \dots, \mathbf{r}_N) \Psi_0(\mathbf{r}_1, \mathbf{r}_2, \dots, \mathbf{r}_N) = \\ &= \langle \Psi_0 | \hat{V}_{\text{ext}} | \Psi_0 \rangle.\end{aligned}\tag{A.1}$$

The ground state of the non-interacting particle system $\Psi_0(\mathbf{r}_1, \mathbf{r}_2, \dots, \mathbf{r}_N)$ is defined as

$$\Psi_0(\mathbf{r}_1, \mathbf{r}_2 \dots \mathbf{r}_N) = S[\psi_1(\mathbf{r}_1)\psi_2(\mathbf{r}_2)\dots\psi_n(\mathbf{r}_n)\dots\psi_N(\mathbf{r}_N)] \quad (\text{A.2})$$

where N denotes the number of electrons, and S is the antisymmetrization operator. The fact that the orbitals ψ_i fulfill the relation

$$\int d^3r \psi_i^*(\mathbf{r})\psi_j(\mathbf{r}) = \delta_{ij}. \quad (\text{A.3})$$

is used from line five to line six.

A.2 Proof of Equation (4.7)

$$\frac{d}{d\lambda} \langle \Psi_\lambda | \hat{V}_\lambda | \Psi_\lambda \rangle = \langle \Psi_\lambda | \frac{d\hat{V}_\lambda}{d\lambda} | \Psi_\lambda \rangle + \langle \frac{d\Psi_\lambda}{d\lambda} | \hat{V}_\lambda | \Psi_\lambda \rangle + \langle \Psi_\lambda | \hat{V}_\lambda | \frac{d\Psi_\lambda}{d\lambda} \rangle \quad (\text{A.4})$$

The second and the third term on the right hand side yield

$$\begin{aligned} & \sum_{i=1}^N \int d^3r_1 \dots d^3r_N \frac{d\Psi_\lambda^*}{d\lambda}(\mathbf{r}_1, \dots, \mathbf{r}_N) \hat{v}_\lambda(\mathbf{r}_i) \Psi_\lambda(\mathbf{r}_1, \dots, \mathbf{r}_N) + \\ & + \sum_{i=1}^N \int d^3r_1 \dots d^3r_N \Psi_\lambda^*(\mathbf{r}_1, \dots, \mathbf{r}_N) \hat{v}_\lambda(\mathbf{r}_i) \frac{d\Psi_\lambda}{d\lambda}(\mathbf{r}_1, \dots, \mathbf{r}_N) = \\ & = \sum_{i=1}^N \int d^3r_1 \dots d^3r_N \hat{v}_\lambda(\mathbf{r}_i) \frac{d}{d\lambda} (\Psi_\lambda^*(\mathbf{r}_1, \dots, \mathbf{r}_N) \Psi_\lambda(\mathbf{r}_1, \dots, \mathbf{r}_N)) = \\ & = \int d^3r \hat{v}_\lambda(\mathbf{r}) \frac{d}{d\lambda} \left(N \int d^3r_2, \dots, d^3r_N \Psi_\lambda^*(\mathbf{r}, \mathbf{r}_2, \dots, \mathbf{r}_N) \Psi_\lambda(\mathbf{r}, \mathbf{r}_2, \dots, \mathbf{r}_N) \right) = \\ & = \int d^3r \hat{v}_\lambda(\mathbf{r}) \frac{d}{d\lambda} n_\lambda(\mathbf{r}) = 0 \end{aligned} \quad (\text{A.5})$$

The term $\frac{d}{d\lambda} n_\lambda(\mathbf{r})$ equals zero because the ground state density in the Adiabatic Connection Theorem is exact and therefore constant for every λ , so that we finally arrive at the equality

$$\frac{d}{d\lambda} \langle \Psi_\lambda | \hat{V}_\lambda | \Psi_\lambda \rangle = \langle \Psi_\lambda | \frac{d\hat{V}_\lambda}{d\lambda} | \Psi_\lambda \rangle \quad (\text{A.6})$$

A.3 Proof of Equation (4.11)

$$\begin{aligned}
 \langle \Psi_\lambda | \hat{W} | \Psi_\lambda \rangle &= \frac{1}{2} \int d^3 r_1 \dots d^3 r_N \sum_{i \neq j} \frac{1}{|\mathbf{r}_i - \mathbf{r}_j|} |\Psi(\mathbf{r}_1 \dots \mathbf{r}_N)|^2 \\
 &= \frac{1}{2} N(N-1) \int d^3 r d^3 r' \frac{1}{|\mathbf{r} - \mathbf{r}'|} \int d^3 r_3 \dots d^3 r_N |\Psi(\mathbf{r}, \mathbf{r}', \mathbf{r}_3 \dots \mathbf{r}_N)|^2 \\
 &= \frac{1}{2} \int d^3 r d^3 r' \frac{n^{2,\lambda}(\mathbf{r}, \mathbf{r}')}{|\mathbf{r} - \mathbf{r}'|}
 \end{aligned} \tag{A.7}$$

From line one to two the antisymmetry of the many electron wavefunction is used.

A.4 Proof of Equation (4.12)

$$\begin{aligned}
 &\frac{1}{2} \int d^3 r d^3 r' \frac{1}{|\mathbf{r} - \mathbf{r}'|} (\langle \Psi_\lambda | \hat{n}(\mathbf{r}) \hat{n}(\mathbf{r}') | \Psi_\lambda \rangle - \delta(\mathbf{r} - \mathbf{r}') \langle \Psi_\lambda | \hat{n}(\mathbf{r}) | \Psi_\lambda \rangle) = \\
 &= \frac{1}{2} \int \frac{d^3 r d^3 r'}{|\mathbf{r} - \mathbf{r}'|} \int d^3 r_1 \dots d^3 r_N \left\{ \sum_{i,j} \delta(\mathbf{r} - \mathbf{r}_i) \delta(\mathbf{r} - \mathbf{r}_j) - \delta(\mathbf{r} - \mathbf{r}') \sum_i \delta(\mathbf{r} - \mathbf{r}_i) \right\} |\Psi_\lambda|^2 = \\
 &= \frac{1}{2} \int \frac{d^3 r d^3 r'}{|\mathbf{r} - \mathbf{r}'|} \int d^3 r_1 \dots d^3 r_N \left\{ \sum_{i,j \neq i} \delta(\mathbf{r} - \mathbf{r}_i) \delta(\mathbf{r} - \mathbf{r}_j) + \delta(\mathbf{r} - \mathbf{r}') \sum_i \delta(\mathbf{r} - \mathbf{r}_i) \right. \\
 &\quad \left. - \delta(\mathbf{r} - \mathbf{r}') \sum_i \delta(\mathbf{r} - \mathbf{r}_i) \right\} |\Psi_\lambda|^2 = \\
 &= \frac{1}{2} \int \frac{d^3 r d^3 r'}{|\mathbf{r} - \mathbf{r}'|} \int d^3 r_1 \dots d^3 r_N \sum_{i,j \neq i} \delta(\mathbf{r} - \mathbf{r}_i) \delta(\mathbf{r} - \mathbf{r}_j) |\Psi_\lambda(\mathbf{r}_1 \dots \mathbf{r}_N)|^2 = \\
 &= \frac{1}{2} \int \frac{d^3 r d^3 r'}{|\mathbf{r} - \mathbf{r}'|} N(N-1) \int d^3 r_3 \dots d^3 r_N |\Psi_\lambda(\mathbf{r}, \mathbf{r}', \mathbf{r}_3 \dots \mathbf{r}_N)|^2 = \\
 &= \frac{1}{2} \int d^3 r d^3 r' \frac{n^{2,\lambda}(\mathbf{r}, \mathbf{r}')}{|\mathbf{r} - \mathbf{r}'|}.
 \end{aligned} \tag{A.8}$$

A.5 Retarded Density-Density Response Function

We start from the Kubo formula which expresses the linear response of an operator A to a perturbation B

$$\chi_{AB}^R(t, t') = -i\theta(t - t') \langle [\hat{A}(t), \hat{B}(t')] \rangle_0. \quad (\text{A.9})$$

For the density-density response, we are interested in the change of density at time t when the density is disturbed at time t' . Accordingly (A.9) yields

$$\chi_{nn}^R(t, t') = -i\theta(t - t') \langle \Psi_0 | [\hat{n}(t), \hat{n}(t')] | \Psi_0 \rangle \quad (\text{A.10})$$

where Ψ_0 with energy E_0 corresponds to the groundstate of the unperturbed Hamiltonian H_0 and \hat{n} is the one particle density operator. We consider here the interaction picture, accordingly only the perturbation is time-dependent, whereas the unperturbed Hamiltonian is time independent. The time evolution for an operator A is given by

$$\hat{A}(t) \equiv e^{iH_0 t} A e^{-iH_0 t}. \quad (\text{A.11})$$

Thus equation (A.10) becomes

$$\begin{aligned} \chi_{nn}^R(\mathbf{r}, \mathbf{r}', t - t') &= -i\theta(t - t') \langle \Psi_0 | [e^{iH_0 t} \hat{n}(r) e^{-iH_0 t}, e^{iH_0 t'} \hat{n}(r') e^{-iH_0 t'}] | \Psi_0 \rangle = \\ &= -i\theta(t - t') \left(e^{iE_0(t-t')} \langle \Psi_0 | \hat{n}(r) e^{-iH_0 t} e^{iH_0 t'} \hat{n}(r') | \Psi_0 \rangle - \right. \\ &\quad \left. - e^{-iE_0(t-t')} \langle \Psi_0 | \hat{n}(r') e^{-iH_0 t'} e^{iH_0 t} \hat{n}(r) | \Psi_0 \rangle \right) \end{aligned} \quad (\text{A.12})$$

With the resolution of identity $\mathbf{1} = \sum_s |\Psi_s\rangle \langle \Psi_s|$, with $\tau = t - t'$ and with the short notation $|\Psi_j\rangle = |j\rangle$ for $j = 0, s$ we can write

$$\begin{aligned} \chi_{nn}^R(\mathbf{r}, \mathbf{r}', \tau) &= \\ &= -i\theta(\tau) \sum_s \left(e^{i(E_0 - E_s)\tau} \langle 0 | \hat{n}(\mathbf{r}) | s \rangle \langle s | \hat{n}(\mathbf{r}') | 0 \rangle - e^{-i(E_0 - E_s)\tau} \langle 0 | \hat{n}(\mathbf{r}') | s \rangle \langle s | \hat{n}(\mathbf{r}) | 0 \rangle \right) \end{aligned} \quad (\text{A.13})$$

¹ $H_0 |\Psi_s\rangle = E_s |\Psi_s\rangle$

The density-density response function in frequency space is obtained by Fourier Transformation

$$\chi_{nn}^{\text{R}}(\mathbf{r}, \mathbf{r}', \hat{\omega}) = \int_{-\infty}^{\infty} d\tau e^{i\omega\tau} e^{-\eta\tau} \chi_{nn}^{\text{R}}(\mathbf{r}, \mathbf{r}', \tau) \quad (\text{A.14})$$

For retarded response functions, which are not decaying at large times, we define the Fourier Transformation with a complex frequency $\hat{\omega} = \omega + i\eta$, where η is a positive infinitesimal. The Fourier Transform yields

$$\begin{aligned} \chi_{nn}^{\text{R}}(\mathbf{r}, \mathbf{r}', \hat{\omega}) &= \\ &= -i \sum_s \int_0^{\infty} d\tau e^{i\hat{\omega}\tau} \left(e^{i(E_0 - E_s)\tau} \langle 0 | \hat{n}(\mathbf{r}) | s \rangle \langle s | \hat{n}(\mathbf{r}') | 0 \rangle - e^{-i(E_0 - E_s)\tau} \langle 0 | \hat{n}(\mathbf{r}') | s \rangle \langle s | \hat{n}(\mathbf{r}) | 0 \rangle \right) = \\ &= \sum_s \left(\frac{\langle 0 | \hat{n}(\mathbf{r}) | s \rangle \langle s | \hat{n}(\mathbf{r}') | 0 \rangle}{E_0 - E_s + \hat{\omega}} - \frac{\langle 0 | \hat{n}(\mathbf{r}') | s \rangle \langle s | \hat{n}(\mathbf{r}) | 0 \rangle}{-(E_0 - E_s) + \hat{\omega}} \right) = \\ &= \sum_{s \neq 0} \left(\frac{\langle 0 | \hat{n}(\mathbf{r}) | s \rangle \langle s | \hat{n}(\mathbf{r}') | 0 \rangle}{E_0 - E_s + \hat{\omega}} + \frac{\langle 0 | \hat{n}(\mathbf{r}') | s \rangle \langle s | \hat{n}(\mathbf{r}) | 0 \rangle}{E_0 - E_s - \hat{\omega}} \right) \end{aligned} \quad (\text{A.15})$$

A.6 Proof of Equation (4.16)

We use the short hand notation $|\Psi_s\rangle = |s\rangle$, $E_{0s} = E_0 - E_s$ and omit the coupling parameter λ

$$\begin{aligned}
& \int_0^\infty d\omega (\chi(\mathbf{r}, \mathbf{r}', i\omega) + \chi(\mathbf{r}', \mathbf{r}, i\omega)) = \\
& = \int_0^\infty d\omega \sum_{s \neq 0} \left[\left(\frac{1}{E_{0s} + i\omega} + \frac{1}{E_{0s} - i\omega} \right) (\langle 0|\hat{n}(\mathbf{r})|s\rangle\langle s|\hat{n}(\mathbf{r}')|0\rangle + \langle 0|\hat{n}(\mathbf{r}')|s\rangle\langle s|\hat{n}(\mathbf{r})|0\rangle) \right] = \\
& = \int_0^\infty d\omega \frac{2E_{0s}}{E_{0s}^2 + \omega^2} \sum_{s \neq 0} (\langle 0|\hat{n}(\mathbf{r})|s\rangle\langle s|\hat{n}(\mathbf{r}')|0\rangle + \langle 0|\hat{n}(\mathbf{r}')|s\rangle\langle s|\hat{n}(\mathbf{r})|0\rangle) = \\
& = 2 \tan^{-1} \left(\frac{\omega}{E_{0s}} \right) \Big|_0^\infty \sum_{s \neq 0} (\langle 0|\hat{n}(\mathbf{r})|s\rangle\langle s|\hat{n}(\mathbf{r}')|0\rangle + \langle 0|\hat{n}(\mathbf{r}')|s\rangle\langle s|\hat{n}(\mathbf{r})|0\rangle) = \\
& = 2(\text{sign}(E_{0s}) \left(\frac{\pi}{2} - 0 \right)) \sum_{s=0} (\langle 0|\hat{n}(\mathbf{r})|s\rangle\langle s|\hat{n}(\mathbf{r}')|0\rangle + \langle 0|\hat{n}(\mathbf{r}')|s\rangle\langle s|\hat{n}(\mathbf{r})|0\rangle) \\
& \quad - \langle 0|\hat{n}(\mathbf{r})|0\rangle\langle 0|\hat{n}(\mathbf{r}')|0\rangle + \langle 0|\hat{n}(\mathbf{r}')|0\rangle\langle 0|\hat{n}(\mathbf{r})|0\rangle) = \\
& = -2\pi(\langle 0|\hat{n}(\mathbf{r})\hat{n}(\mathbf{r}')|0\rangle + n(\mathbf{r})n(\mathbf{r}'))
\end{aligned} \tag{A.16}$$

Hence the density response is directly linked to $n^{2,\lambda}(\mathbf{r}, \mathbf{r}')$.

A.7 Retarded Kohn-Sham Density-Density Response Function

For the Kohn-Sham system the groundstate is denoted by a product of one particle wavefunctions (orbitals)

$$\Psi_0(\mathbf{r}_1, \mathbf{r}_2 \dots \mathbf{r}_N) = S[\psi_1(\mathbf{r}_1)\psi_2(\mathbf{r}_2) \dots \psi_n(\mathbf{r}_n) \dots \psi_N(\mathbf{r}_N)] \tag{A.17}$$

where N denotes the number of electrons, and S is the antisymmetrization operator. An excited state is expressed by replacing the n^{th} occupied orbital by an unoccupied orbital with index $m > N$.

$$\Psi_s(\mathbf{r}_1, \mathbf{r}_2 \dots \mathbf{r}_N) = S[\psi_1(\mathbf{r}_1)\psi_2(\mathbf{r}_2) \dots \psi_m(\mathbf{r}_n) \dots \psi_N(\mathbf{r}_N)]. \tag{A.18}$$

From the derivation of the retarded density-density response function we see that $E_0 = \sum_j \epsilon_j$ and $E_s = \sum_j \epsilon_j - \epsilon_n + \epsilon_m$. ϵ_j is the eigenvalue corresponding to the orbital ψ_j . Inserting these expressions into the definition (A.15) we obtain with $\eta \rightarrow 0$

$$\chi_{nn}^{\text{R,KS}}(\mathbf{r}, \mathbf{r}', \omega) = \sum_n^{\text{occ}} \sum_m^{\text{uocc}} \left(\frac{\psi_n^*(\mathbf{r})\psi_m(\mathbf{r})\psi_m^*(\mathbf{r}')\psi_n(\mathbf{r}')}{\epsilon_n - \epsilon_m + \omega} + \frac{\psi_n^*(\mathbf{r}')\psi_m(\mathbf{r}')\psi_m^*(\mathbf{r})\psi_n(\mathbf{r})}{\epsilon_n - \epsilon_m - \omega} \right). \quad (\text{A.19})$$

Appendix B

Random Phase Approximation in VASP

B.1 Proof of Equation (6.5)

Inserting (6.3) in Bloch's theorem (6.1) yields

$$\psi_{n\mathbf{k}}(\mathbf{r}) = \psi_{n\mathbf{k}}(\mathbf{r} + N_1\mathbf{a}_1 + N_2\mathbf{a}_2 + N_3\mathbf{a}_3) = u_{n\mathbf{k}}(\mathbf{r})e^{i\mathbf{k}\mathbf{r}}e^{i\mathbf{k}(N_1\mathbf{a}_1+N_2\mathbf{a}_2+N_3\mathbf{a}_3)} \quad (\text{B.1})$$

This to be true requires

$$e^{i\mathbf{k}(N_1\mathbf{a}_1+N_2\mathbf{a}_2+N_3\mathbf{a}_3)} = e^{i(x_1\mathbf{b}_1+x_2\mathbf{b}_2+x_3\mathbf{b}_3)(N_1\mathbf{a}_1+N_2\mathbf{a}_2+N_3\mathbf{a}_3)} = e^{i2\pi(x_1N_1+x_2N_2+x_3N_3)} = 1, \quad (\text{B.2})$$

so that follows

$$x_i = \frac{m_i}{N_i}, \quad m_i \in \mathbb{Z}_{N_i} \quad (\text{B.3})$$

for $i = 1, 2, 3$.

B.2 Proof of Equation (6.25)

With the reformulation of the Dyson like equation for $\chi^{\lambda, \text{RPA}}(\mathbf{q}, i\omega)$ (in 5.11 in real space) in reciprocal space

$$\chi_{\mathbf{G}, \mathbf{G}'}^{\lambda, \text{RPA}}(\mathbf{q}, i\omega) = \chi_{\mathbf{G}, \mathbf{G}'}^{\lambda, \text{KS}}(\mathbf{q}, i\omega) + \sum_{\mathbf{G}_1} \chi_{\mathbf{G}, \mathbf{G}_1}^{\text{KS}}(\mathbf{q}, i\omega) \lambda \nu_{\mathbf{G}_1}(\mathbf{q}) \chi_{\mathbf{G}_1, \mathbf{G}'}^{\lambda, \text{RPA}}(\mathbf{q}, i\omega) \quad (\text{B.4})$$

to

$$\chi_{\mathbf{G}, \mathbf{G}'}^{\lambda, \text{RPA}}(\mathbf{q}, i\omega) = \sum_{\mathbf{G}_1} (1 - \lambda \chi_{\mathbf{G}, \mathbf{G}_1}^{\text{KS}}(\mathbf{q}, i\omega) \cdot \nu(\mathbf{q}))_{\mathbf{G}, \mathbf{G}_1}^{-1} \chi_{\mathbf{G}_1, \mathbf{G}'}^{\text{KS}}(\mathbf{q}, i\omega) \quad (\text{B.5})$$

follows immediately (we omit the arguments $\mathbf{q}, \mathbf{G}, \mathbf{G}'$ and $i\omega$ for now)

$$-\frac{\partial}{\partial \lambda} \text{Tr}\{\ln[1 - \lambda \chi^{\text{KS}} \nu]\} = \text{Tr}\{(1 - \lambda \chi^{\text{KS}} \nu)^{-1} \chi^{\text{KS}} \nu\} = \text{Tr}\{\chi^{\lambda, \text{RPA}} \nu\}. \quad (\text{B.6})$$

Inserting the above equality into

$$E_c^{\text{RPA}} = - \int_0^1 d\lambda \frac{1}{2\pi} \int_0^\infty d\omega \text{Tr}\{\nu (\chi^{\lambda, \text{RPA}}(i\omega) - \chi^{\text{KS}}(i\omega))\} \quad (\text{B.7})$$

yields

$$E_c^{\text{RPA}} = \frac{1}{2\pi} \int_0^\infty d\omega \text{Tr}\{\ln[1 - \chi^{\text{KS}}(i\omega) \nu] + \chi^{\text{KS}}(i\omega) \nu\}. \quad (\text{B.8})$$

Appendix C

Zero-Point Vibration Energies and Corrected Experimental Lattice Constants

C.1 The change in Equilibrium Energy due to Phonon Zero-Point Vibration Energies

In [39] in Appendix A, an *average phonon frequency* is introduced as

$$E_{\text{zp}} = \frac{3}{2} \hbar \omega \quad (\text{C.1})$$

where E_{zp} describes the phonon zero-point energy per atom. To describe the average phonon frequency

$$\omega = 2\pi \frac{\int f(\nu) \nu d\nu}{\int f(\nu) d\nu} \quad (\text{C.2})$$

The calculation $f(\nu)$ for any real crystal was according to [92] in the 1930's an unsolved problem. If one is only interested in the behaviour of $f(\nu)$ at very low temperatures it may be shown quite generally that for a solid of volume V

$$f(\nu) d\nu = BV v^2 d\nu \quad (\text{C.3})$$

where B is a constant. One of the first attempts to generalize this for the entire frequency range was proposed by Debye, who set

$$\begin{aligned} f(\nu) &= BV\nu^2 \quad (\nu < \nu_D) \\ &= 0 \quad (\nu > \nu_D) \end{aligned} \tag{C.4}$$

with ν being defined by

$$\int_0^{\nu_D} f(\nu) d\nu = 3N \tag{C.5}$$

so that follows

$$\frac{BV\nu_D^3}{3} = 3N \tag{C.6}$$

Plugging (C.4) into (C.2) yields

$$\omega = 2\pi \frac{3}{4} \nu_D = \frac{3}{4} \omega_D \tag{C.7}$$

so that we finally can write

$$\hbar\omega = \frac{3}{4} k_B \Theta_D \tag{C.8}$$

Using a superscript zero to indicate a quantity in the absence of phonon zero-point energy we find

$$E(V) = E^0(V) + \frac{3}{2} \hbar\omega \tag{C.9}$$

with

$$\Delta E(V_0) = E^0(V) - E(V) \tag{C.10}$$

where V_0 describes the equilibrium volume. We can immediately write

$$\frac{\Delta E(V_0)}{E(V_0)} = -\frac{9}{8} \frac{k_B \Theta_D}{E(V_0)} \tag{C.11}$$

C.2 The Change in Equilibrium Volume due to Phonon Zero-Point Vibration Energies

$E(V)$ in (C.9) has its minimum at the experimental volume V_0 . So that

$$\left. \frac{dE(V)}{dV} \right|_{V=V_0} = 0. \tag{C.12}$$

This yields with (C.9)

$$\left. \frac{dE(V)}{dV} \right|_{V=V_0} = 0 = \left. \frac{dE^0(V)}{dV} \right|_{V=V_0} + \frac{3}{2} \hbar \left. \frac{d\omega(V)}{dV} \right|_{V=V_0} \quad (\text{C.13})$$

$$P^0(V_0) = \frac{3}{2} \hbar \left. \frac{d\omega(V)}{dV} \right|_{V=V_0} \quad (\text{C.14})$$

$$P^0(V_0) = \frac{3}{2} \hbar \omega'(V_0) = \frac{3}{2} \hbar \omega'(V_0) \frac{V_0}{\omega(V_0)} \frac{\omega(V_0)}{V_0} = \quad (\text{C.15})$$

$$= -\frac{3}{2} \hbar \frac{\omega(V_0)}{V_0} \gamma(V_0) \quad (\text{C.16})$$

with

$$\gamma(V_0) = \frac{1}{2} (B_1 - 1) \quad (\text{C.17})$$

and (C.8) we find

$$P^0(V_0) = -\frac{9}{16} (B_1 - 1) \frac{k_B \Theta_D}{V_0} \quad (\text{C.18})$$

Expanding $P^0(V)$ around the volume which minimizes $E^0(V)$, \hat{V} , gives

$$P(V) \approx P^0(\hat{V}) + P'(\hat{V})(V - \hat{V}) = P'(\hat{V})(V - \hat{V}) \quad (\text{C.19})$$

so that we can write

$$P'(\hat{V})(V_0 - \hat{V}) = P'(\hat{V})(V_0 - \hat{V}) \frac{\hat{V}}{\hat{V}} = B^0(\hat{V}) \frac{\Delta V}{\hat{V}} \quad (\text{C.20})$$

$$\frac{\Delta V}{\hat{V}} = \frac{9}{16} (B_1 - 1) \frac{k_B \Theta_D}{V_0 B^0(\hat{V})}. \quad (\text{C.21})$$

Here, \hat{V} is the volume calculated without including phonon zero-point energy effects and $\Delta V = V_0 - \hat{V}$ is the change in volume due to the phonon zero-point energy.

Appendix D

Assessing the RPA for Solids and Molecules

Results for the G2-1 test set [60, 61] as summarized in table D.1. LDA results were taken from [62] and are corrected for zero-point vibrational effects and thus have to be compared to the non-corrected experimental values in parenthesis taken from [60] and [61]. PBE and HSEsol results are published in [42] and the results for RPA in the supplementary materials of [59]. Experimental values in parenthesis are non-corrected for zero-point vibrational energy effects and are taken from [62]. Corrected values are taken from [33].

Table D.1: Atomization energies in kJ/mol/formula unit for the G2-1 test set. Experimental values in parenthesis are non-corrected for zero-point vibrational energy effects and are taken from [62]. Corrected values are taken from [33].

	LDA	Dev.	PBE	Dev.	HSEsol	Dev.	RPA	Dev.	Exp
BeH	241	45	231	30	239	39	209	8	201(196)
C ₂ H ₂	1856	229	1735	45	1744	53	1592	-98	1690(1627)
C ₂ H ₄	2518	292	2390	39	2431	79	2246	-105	2351(2225)
C ₂ H ₆	3137	349	2997	22	3071	96	2671	-303	2975(2788)
CH	368	34	354	3	355	4	339	-12	351(334)
CH ₂ (¹ A ₁)	790	77	748	-13	760	-2	731	-31	761(714)
CH ₂ (³ B ₁)	848	97	814	23	833	42	751	-39	791(751)
CH ₃	1347	137	1297	16	1325	44	1232	-49	1280(1210)
CH ₃ Cl	1778	226	1672	19	1712	60	1569	-83	1653(1552)
CH ₃ OH	2325	313	2173	26	2211	65	2052	-95	2146(2012)
CH ₃ SH	2128	266	2000	21	2051	72	1899	-80	1979(1862)
CH ₄	1823	181	1756	-1	1797	40	1693	-64	1757(1642)
CN	908	169	826	77	773	24	719	-30	749(739)
CO	1238	166	1124	32	1103	11	1021	-71	1092(1072)
CO ₂	1949	351	1737	97	1703	63	1522	-118	1640(1598)
CS	838	129	750	31	731	11	668	-52	720(709)
Cl ₂	346	107	275	36	276	38	205	-33	238(239)
ClF	394	142	301	42	286	27	219	-40	259(252)
ClO	436	171	341	82	313	54	242	-17	259(265)
F ₂	321	167	218	59	179	20	126	-33	159(154)
H ₂ CO	1747	253	1612	39	1613	40	1486	-87	1573(1495)
H ₂ O	1062	144	978	3	986	11	934	-41	975(918)
H ₂ O ₂	1335	279	1176	55	1164	43	1069	-52	1121(1056)
H ₂ S	826	101	762	0	783	21	738	-24	761(725)
HCN	1468	205	1364	55	1339	30	1248	-62	1310(1263)
HCO	1360	229	1234	66	1218	50	1101	-67	1167(1131)
HCl	487	59	442	-6	455	7	418	-29	448(428)
HF	656	90	592	-2	595	1	555	-39	594(566)
HOCl	851	197	732	42	727	37	644	-46	690(654)

Table D.2: Atomization energies in kJ/mol/formula unit for the G2-1 test set.(Continued from previous page).

	LDA	Dev.	PBE	Dev.	HSEsol	Dev.	RPA	Dev.	Exp
Li ₂	97	-4	83	-25	84	-24	77	-32	109(100)
LiF	645	69	579	-2	566	-16	524	-57	582(576)
LiH	246	12	224	-19	228	-15	226	-17	243(234)
N ₂	1105	163	1019	69	967	17	932	-18	950(942)
N ₂ H ₄	2024	328	1894	66	1906	77	1784	-44	1828(1696)
NH	381	50	371	28	363	20	344	1	343(331)
NH ₂	823	111	790	28	787	25	749	-12	761(711)
NH ₃	1325	168	1263	20	1274	31	1216	-27	1243(1158)
NO	821	193	719	79	671	31	617	-23	640(628)
Na ₂	83	14	74	-6	67	-12	53	-26	79(69)
NaCl	430	22	392	-22	401	-14	373	-41	414(408)
O ₂	721	228	598	104	559	65	472	-22	494(494)
OH	495	71	459	11	457	10	432	-15	448(424)
P ₂	596	110	508	22	491	6	480	-5	485(486)
PH ₂	693	87	646	6	662	22	639	-1	640(605)
PH ₃	1067	116	1000	-8	1028	20	995	-13	1008(951)
S ₂	562	141	482	72	475	65	403	-8	410(421)
SO	695	179	591	80	566	55	490	-20	510(517)
SO ₂	1391	328	1173	115	1130	71	1000	-59	1059(1063)
Si ₂	387	77	340	30	338	28	293	-17	310(310)
Si ₂ H ₆	2299	206	2175	-55	2252	22	2162	-68	2230(2092)
SiH ₂ (¹ A ₁)	666	62	619	-25	635	-9	622	-23	644(604)
SiH ₂ (³ B ₁)	585	68	550	2	572	24	533	-15	548(516)
SiH ₃	978	83	930	-16	962	17	923	-23	946(895)
SiH ₄	1372	105	1311	-44	1355	0	1318	-38	1356(1267)
SiO	931	133	822	23	795	-4	754	-46	799(797)
ME	151		27		29		-45		
MAE	151		36		32		45		

Appendix E

Carbon Water Interaction

E.1 Analytical Behaviour of the RPA Correlation Energy

The RPA correlation energy is sufficiently smooth to analyze its analytical behaviour. As expected for the interaction between an insulating/semiconducting sheet and a molecule, the correlation energy is proportional to $\frac{1}{(d-c)^4}$, where d is the distance between the O-atom and the graphene slab in \AA and c is a constant which equals 0.47 and 0.28 for the one- and the two-leg configuration, respectively (see figure E.1 for the one leg structure and figure E.2 for the two leg structure); the center of polarizability of the water molecule is obviously shifted towards the H atoms.

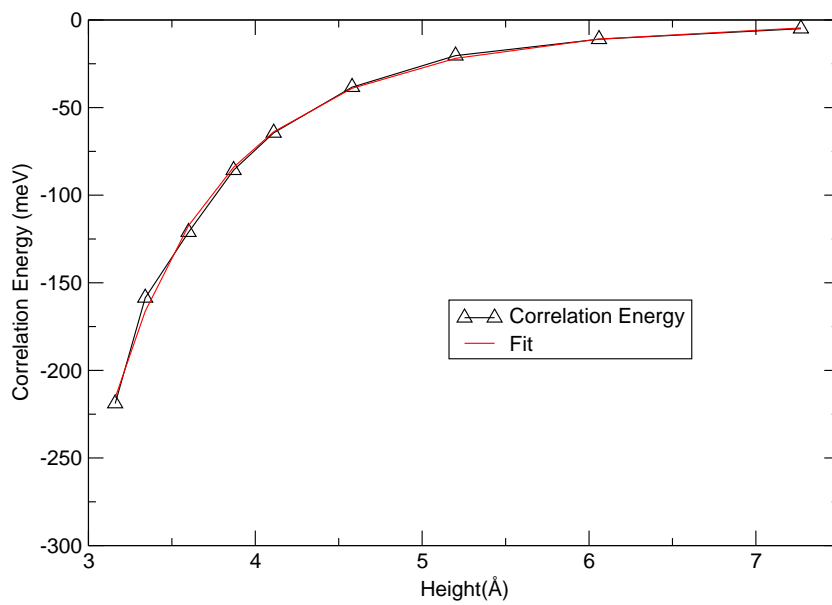


Figure E.1: One leg structure: The correlation energy is proportional to $\frac{1}{(d-c)^4}$, where d is the distance between the O-atom and the graphene slab in Å and c is a constant which equals 0.47.

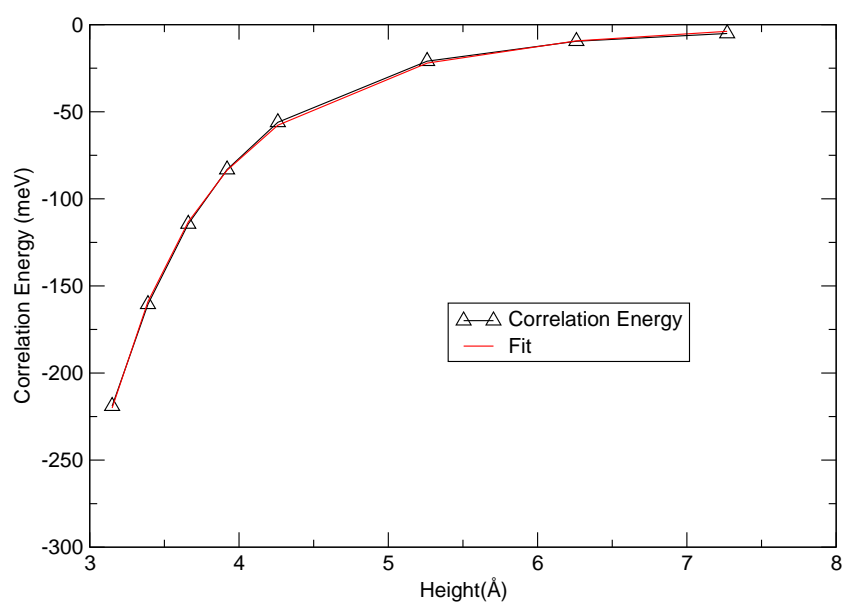


Figure E.2: Two leg structure: The correlation energy is proportional to $\frac{1}{(d-c)^4}$, where d is the distance between the O-atom and the graphene slab in Å and c is a constant which equals 0.28.

Bibliography

- [1] P. Nozières and D. Pines, *Phys.Rev.B* **111**, 442 (1958).
- [2] F. Furche, *Phys.Rev.B* **64**, 195129 (2001).
- [3] N. E. Dahlen, R. van Leeuwen and U. von Barth, *Phys.Rev.A* **73**, 012511 (2006).
- [4] M. Fuchs and X. Gonze, *Phys.Rev.B* **65**, 235109 (2002).
- [5] T. Miyake, F. Aryasetiawan, T. Kotani, M. van Schilfgaarde, M. Usuda and K. Terakura, *Phys.Rev.B* **66**, 245103 (2002).
- [6] A. Marini, P. García-González and A. Rubio, *Phys.Rev.Lett.* **96**, 136404 (2006).
- [7] M. Born and J. R. Oppenheimer, *Ann. Physik* **84**, 457 (1927).
- [8] P. Hohenberg and W. Kohn, *Phys.Rev.* **136**, B 864 (1964).
- [9] This chapter follows partly a talk by E.K.U Gross given in Benasque in 2010 <http://www.tddft.org/TDDFT2010/school/gross1.pdf>.
- [10] R. M. Martin, *Electronic Structure*, Cambridge University Press, (2004).
- [11] W. Kohn and L. J. Sham, *Phys.Rev.* **140**, A1133 (1965).
- [12] D. M. Ceperley and B. J. Alder, *Phys.Rev.Lett.* **45**, 566 (1980).

-
- [13] J. P. Perdew and K. Burke, *Int.J.Quant.Chem.* **57**, 309 (1996).
- [14] J. P. Perdew, K. Burke and M. Ernzerhof, *Phys.Rev.Lett.* **77**, 3865 (1996).
- [15] J. P. Perdew, A. Ruzsinszky, G. I. Csonka, O. A. Vydrov, G. E. Scuseria, L. A. Constantin, X. Zhou and K. Burke, *Phys.Rev.Lett.* **100**, 136406 (2008).
- [16] B. Hammer, L. B. Hansen and J. K. Nørskov, *Phys.Rev. B* **59**, 7413 (1999).
- [17] C. Lee, W. Yang and R. Parr, *Phys.Rev.B* **37**, 785 (1988).
- [18] R. Armiento and A. E. Mattsson, *Phys.Rev.B* **72**, 085108 (2005).
- [19] H. B. Callen and T. A. Welton, *Phys.Rev.* **83**, 34 (1951).
- [20] D. C. Langreth and J. C. Perdew, *Solid State Commun.* **17**, 1425 (1975).
- [21] E. K. U. Gross and W. Kohn, *Phys.Rev.Lett.* **55**, 2850 (1985).
- [22] G. Kresse and J. Hafner, *Phys. Rev. B* **48**, 13115 (1993).
- [23] G. Kresse and J. Furthmüller, *Comput. Mater. Sci.* **6**, 15 (1996).
- [24] H. J. Monkhorst and J. D. Pack, *Phys.Rev.B* **13**, 5188 (1976).
- [25] M. C. Payne, M. P. Teter, D. C. Allan, T. A. Arias and J. D. Joannopoulos, *Rev. Mod. Phys.* **64**, 1045 (1992).
- [26] P. E. Blöchl, *Phys.Rev.B* **50**, 17953 (1994).
- [27] G. Kresse and D. Joubert, *Phys.Rev.B* **59**, 1758 (1999).
- [28] J. Harl *PhD thesis*, Universität Wien, Austria (2008).
- [29] J. Harl, L. Schimka and G. Kresse, *Phys.Rev.B* **81**, 115126 (2010).

-
- [30] S. L. Adler, *Phys. Rev.* **126**, 413 (1962).
- [31] N. Wiser, *Phys. Rev.* **129**, 62 (1963).
- [32] J. Harl and G. Kresse, *Phys.Rev.B* **77**, 045136 (2008).
- [33] J. Paier, R. Hirschl, M. Marsman and G. Kresse, *J. Chem. Phys.* **122**, 234102 (2005).
- [34] J. Paier, M. Marsman, K. Hummer, G. Kresse, I. C. Gerber and J. G. Angyan, *J. Chem. Phys.* **124**, 154709 (2006).
- [35] A. E. Mattsson and R. Armiento, *Phys. Rev. B* **79**, 155101 (2009).
- [36] J. P. Perdew, A. Ruzsinszky, G. I. Csonka, L. A. Constantin and J. Sun, *Phys.Rev. Lett.* **103**, 026403 (2009).
- [37] J. Harl and G. Kresse, *Phys. Rev. Lett.* **103**, 056401 (2009).
- [38] A. Grüneis, M. Marsman, J. Harl, L. Schimka, and G. Kresse, *J. Chem. Phys.* **131**, 154115 (2009).
- [39] A. B. Alchagirov, J. P. Perdew, J. C. Boettger, R. C. Albers and C. Filohais, *Phys. Rev. B* **63**, 224115 (2001).
- [40] G. Kern, G. Kresse and J. Hafner, *Phys. Rev. B* **59**, 8551 (1999).
- [41] B. B. Karki, R. M. Wentzcovitch, S. de Gironcoli, and S. Baroni, *Phys. Rev. B* **61**, 8793 (2000).
- [42] L. Schimka, J. Harl and G. Kresse, *J. Chem. Phys.* **134**, 024116 (2011).
- [43] G. Kresse, J. Furthmüller and J. Hafner, *Europhys. Lett.* **32**, 729 (1995).
- [44] B. Grabowski, H. Tilmann and J. Neugebauer, *Phys. Rev. B* **76**, 024309 (2007).

-
- [45] P. Haas, F. Tran, and P. Blaha, *Phys. Rev. B* **79**, 085104 (2009); 79, 209902(E) (2009).
- [46] J. P. Perdew and K. Schmidt, *Density Functional Theory and its Application to Materials*, edited by V. Van Doren, C. Van Alsenoy, and P. Geerlings AIP, Melville, New York, (2001).
- [47] A. V. Krukau, O. A. Vydrov, A. F. Izmaylov and G. E. Scuseria, *J. Chem. Phys.* **125**, 224106 (2006).
- [48] M. Ernzerhof and J. P. Perdew, *J. Chem. Phys.* **109**, 3313(1998).
- [49] T. M. Henderson, B. G. Janesko and G. E. Scuseria, *J. Chem. Phys.* **128**, 194105 (2008).
- [50] E. Weintraub, T. M. Henderson and G. E. Scuseria, *J. Chem. Theory Comput.* **5**, 754 (2009).
- [51] J. Heyd, G. E. Scuseria and M. Ernzerhof, *J. Chem. Phys.* **118**, 8207 (2003), *J. Chem. Phys.* **124**, 219906(E) (2006).
- [52] J. Heyd and G. E. Scuseria, *J. Chem. Phys.* **120**, 7274 (2004).
- [53] L. A. Constantin, J. P. Perdew, and J. M. Pitarke, *Phys. Rev. B* **79**, 075126 (2009).
- [54] M. Marsman, J. Paier, A. Stroppa and G. Kresse, *J. Phys.: Condens. Matter* **20**, 064201 (2008).
- [55] M. Shishkin and G. Kresse, *Phys. Rev. B.* **74**, 035101 (2006).
- [56] J. Paier, M. Marsman, and G. Kresse, *J. Chem. Phys.* **127**, 024103 (2007).
- [57] T. Soma, *J. Phys. C: Solid State Phys.* **11**, 2669 (1978).

- [58] W. A. Harrison, *Electronic structure and the properties of solids*, (Dover, New York 1989).
- [59] J. Paier, B. G. Janesko, T. M. Henderson, G. E. Scuseria, A. Grüneis and G. Kresse, *J. Chem. Phys.* **133**, 179902 (2010).
- [60] J. A. Pople, M. Head-Gordon, D. J. Fox, K. Raghavachari, and L. A. Curtiss, *J. Chem. Phys.* **90**,5622 (1989).
- [61] L. A. Curtiss, C. Jones, G. W. Trucks, K. Raghavachari, and J. A. Pople, *J. Chem. Phys.***93**, 2537 (1989).
- [62] A. D. Becke, *J.Chem.Phys.***96**, 2155 (1992).
- [63] R. Asgari, M. Polini, B. Davoudi and M. P. Tosi, *Phys.Rev.B* **68**, 235116 (2003).
- [64] L. Schimka, J. Harl, A. Grüneis, M. Marsman, F. Mittendorfer and G. Kresse, *Nat.Mat.* **9**, 741 (2010).
- [65] G. A. Somorjai, *Chem. Rev.* **96**, 1223 (1996).
- [66] R. A. van Santen, *Molecular Heterogeneous Catalysis: A Conceptual and Computational Approach*; Wiley-VCH: Weinhei, (2005).
- [67] G. A. Somorjai, *Introduction to Surface Chemistry and Catalysis*; Wiley: New York (1994).
- [68] P. J. Feibelman, B. Hammer, J. K. Nørskov, F. Wagner, M. Scheffler, R. Stumpf, R. Watwe and J. Dumesic, *J. Phys. Chem. B* **105**, 4018 (2001).
- [69] A. Stroppa, K. Termentzidis, J. Paier, G. Kresse and J. Hafner, *Phys. Rev. B* **76**, 195440 (2007).
- [70] A. Stroppa and G. Kresse, *New Journal of Physics* **10**, 063020 (2008).

- [71] A. V. Krukau, O. A. Vydrov, A. F. Izmaylov and G. E. Scuseria, *J. Chem. Phys.* **125**, 224106 (2006).
- [72] M. Shishkin, M. Marsman and G. Kresse, *Phys. Rev. Lett.* **99**, 246403 (2007).
- [73] W. R. Tyson and W. A. Miller, *Surf. Sci.* **62**, 267-276 (2007).
- [74] F. Abild-Pedersen and M. P. Andersson, *Surf. Sci.* **601**, 1747-1753 (2007).
- [75] L. Hedin, *Phys. Rev.* **139**, A796-A823 (1965).
- [76] T. Anazawa, I. Kinoshita and Y. Matsumoto, *J. Electron Spectrosc. Relat. Phenom.* **88**, 585-590 (1998).
- [77] G. Tsilimis, J. Kutzner and H. Zacharias, *Applied Physics A* **76**, 743-749 (2003).
- [78] G. J. Blyholder, *J. Phys. Chem.* **68**, 2772 (1964).
- [79] B. Hammer, Y. Morikawa and J. K. Nørskov, *Phys. Rev. Lett.* **76**, 2141-2144 (1996).
- [80] A. Gil, A. Clotet, J. M. Ricart, G. Kresse, M. García-Hernández, N. Rösch and P. Sautet, *Surf. Sci.* **530**, 71-86 (2003).
- [81] Q-M. Hu, K. Reuter and M. Scheffler, *Phys. Rev. Lett.* **98**, 176103 (2007).
- [82] X. Ren, P. Rinke and M. Scheffler *Phys. Rev. B* **80**, 045402 (2009).
- [83] S. E. Mason, I. Grinberg and A. M. Rappe, *Phys. Rev. B* **69**, 161401 (2004).
- [84] S. Lebègue, J. Harl, T. Gould, J. G. Ángyán, G. Kresse and J. F. Dobson, *Phys. Rev. Lett.* **105**, 196401 (2010).

-
- [85] J. Ma, D. Alfè, A. Michaelides and E. Wang, *J.Chem.Phys.* **130**, 154303 (2009).
- [86] G. Hummer, J. C. Rasaiah and J. P. Noworyta, *Nature* **414**, 188 (2001).
- [87] T. Werder, J. H. Walther, R. L. Jaffe, T. Halicioglu and P. Koumoutsakos, *J.Phys.Chem.B* **107**,1345 (2003).
- [88] J. Ma, A. Michaelides, D. Alfè, L. Schimka,G. Kresse and E. Wang, *Phys.Rev.B* **84**, 033402 (2011).
- [89] D. Feller and K. D. Jordan, *J.Phys.Chem.A* **104**, 9971 (2000).
- [90] E. Voloshina, D. Usvyat, M. Schütz and B. Paulus, *Phys.Chem.Chem.Phys.* **13**, 12041 (2011).
- [91] S. Grimme, *J.Comput.Chem.***25**, 1463 (2004).
- [92] N. F. Mott and H. Jones, *The theory of the properties of metals and alloys*, Clarendon Press, Oxford, (1936).
- [93] H. Eshuis, J. E. Bates and F. Furche, *Theor. Chem. Acc.*, (2012) accepted.

Curriculum Vitae

Dipl.-Ing. Laurids Schimka
Faculty of Physics
University of Vienna
Sensengasse 8/12
A-1090 Vienna

Phone: +43 1 4277 51406
EMail: laurids.schimka@univie.ac.at

Date and place of birth: 07.07.1980, Vienna
Citizenship: Austria

Education

PhD thesis: *Application of the Random Phase Approximation to Complex Problems in Materials Science*
under the supervision of Univ.-Prof. DI Dr. Georg Kresse at the
University of Vienna, Sep. 2008 - Mar. 2012

Study at the Grande École '*École Centrale Paris*'
Graduation as 'Ingénieur Diplômé', Jun. 2008

Study of technical physics at the Vienna University of Technology
Graduation as 'Diplom Ingenieur', Jun. 2008

List of Publications

1. Adsorption and diffusion of water on graphene from first principles
J. Ma, A. Michaelides, D. Alfè, L. Schimka, G. Kresse and E. Wang,
Phys.Rev.B **84**, 033402 (2011).
2. Improved hybrid functional for solids: The HSEsol functional
L. Schimka, J. Harl, G. Kresse, *J. Chem. Phys.* **134**, 024116 (2011).
3. Accurate surface and adsorption energies from many-body perturbation theory
L. Schimka, J. Harl, A. Grüneis, M. Marsman, F. Mittendorfer and G. Kresse, *Nat.Mat.* **9**, 741 (2010).
4. Assessing the quality of the random phase approximation for lattice constants and atomization energies of solids
J. Harl, L. Schimka and G. Kresse, *Phys.Rev.B* **81**, 115126 (2010).
5. Making the random phase approximation to electronic correlation accurate
A. Grüneis, M. Marsman, J. Harl, L. Schimka, and G. Kresse, *J. Chem. Phys.* **131**, 154115 (2009).

Talks

1. **CMS&ViCoM Seminar** Vienna, Austria
19 March, 2012
The random phase approximation applied to complex problems in materials science
2. **DPG Spring Meeting 2010** Regensburg, Germany
21-26 March 2010
CO adsorption on transition metal surfaces applying the random phase approximation

Posters

1. **15th ICTP Workshop** Trieste, Italy
13-15 January, 2011
DFT and Beyond - Climbing Jacobs Ladder
2. **Psi-k Meeting** Berlin, Germany
12-16 September, 2010
Assessing the quality of the Random Phase Approximation for solids, surfaces and adsorption problems
3. **CECAM Workshop** Lausanne, Switzerland
28 June -02 July, 2010
Assessing the quality of the Random Phase Approximation for solids, surfaces and adsorption problems
4. **TDDFT Workshop** Benasque, Spain
02-15 January, 2010
CO adsorption on transition metal surfaces applying the random phase approximation
5. **Gordon Research Conference** New London, NH, USA
05-10 July, 2009
Improved description of correlation energies within the ACFDT-RPA framework